MATHEMATICAL MODELS OF MECHANISMS UNDERLYING LONG-TERM TYPE 2 DIABETES PROGRESSION

by

Erica J. Graham

A dissertation submitted to the faculty of
The University of Utah
in partial fulfillment of the requirements for the degree of

Doctor of Philosophy

Department of Mathematics

The University of Utah

August 2012

The University of Utah Graduate School

STATEMENT OF DISSERTATION APPROVAL

The dissertation of **Erica J. Graham**

has been approved by the following supervisory committee members:

Frederick R. Adler	, Chair	**07.13.12** Date Approved
James P. Keener	, Member	**07.13.12** Date Approved
Aaron L. Fogelson	, Member	**07.13.12** Date Approved
L. Charles Murtaugh	, Member	**07.13.12** Date Approved
Alla Borisyuk	, Member	Date Approved

and by **Peter E. Trapa**, Chair of the Department of **Mathematics**

and by Charles A. Wight, Dean of The Graduate School.

ABSTRACT

We develop a series of mathematical models incorporating proposed mechanisms underlying the development of two essential features of long-term type 2 diabetes progression: insulin resistance and β-cell dysfunction. Reduced insulin-stimulated plasma glucose uptake (insulin resistance) and inadequate insulin production by β cells (β-cell dysfunction) lead to a number of metabolic irregularities. We study the interaction of oxidative stress and mitochondrial dysfunction in the development of skeletal muscle insulin resistance, focusing on mitochondrial superoxide production and the functional and physical heterogeneities among mitochondria. We explore primary determinants in β-cell failure, from the perspective of endoplasmic reticulum stress and the unfolded protein response. We conclude with a basis for age-related insulin resistance, an explanation of the fundamental role of nutrient excess in the decline of metabolic health, and an identification of the interplay of cellular and molecular mechanisms important in metabolic dysregulation.

CONTENTS

LIST OF FIGURES

LIST OF TABLES

ACKNOWLEDGMENTS

To Kathy Nesmith and Perry Blickenstaff, thank you for stepping in as you have. I probably would not have made here without you. Literally.

To Dr. Fred Adler, thank you for your cautious optimism, a welcome reprieve from my habitual pessimism. I am indebted to the guidance, extreme patience, and support you have given me over the years. I have the deepest respect and greatest appreciation for your insight and perspective.

To Dr. James Keener, I knew this was the place for me after the single day I spent here during some March, some number of years ago. Thank you for building such an amazing math biology program and for your insight and interest, though I do apologize for giving you medical student syndrome with all of my diabetes talk.

To Dr. Charles Murtaugh, for lending your expertise, for contributing a new perspective, and for your time. Thank you especially for venturing down the hill in the first place.

To Drs. Aaron Fogelson and Alla Borisyuk, for being willing to sit on my committee and for providing a fresh perspective.

To the departmental staff, for paying me and telling me what to do. Special thanks to Paula Tooman and Sandy Hiskey for brightening my days, being sounding boards, and having all the answers.

To the problems at math dot utah dot edu triumvirate, Pieter Bowman, Dr. Nelson Beebe, and Victor Gabrenas, for running a well oiled machine and for solving any computer problem I have ever had and even those I didn't know I had.

To Dr. Ami Radunskaya, for being my ally. I have learned so much from you, as a teacher, mentor, and friend. Thank you for all of the opportunities and for believing in me so fervently.

To Dr. Rhonda Hughes, what can I say? You were there at the very beginning of my math career. I am truly indebted to you for all the years of advice, fierce support, and patience, the years and years of patience. Thank you for being an amazing mentor, friend, leader, and mathematician.

To Dr. Sean Laverty, for the unending advice, for the proofreading, and for lending an ear when I didn't know I needed one.

To Erin Okazaki, MD, for every card, twinkie, and ding dong. As you know, a roller coaster doesn't even begin to describe it, but thank you for being there every crazy step of the way. Dude, you rock!

To Dr. Brittany Bannish, all evidence to the contrary, I'm nonplussed. Wow. Thank you for being such a(n) _____ (adjective) friend, a(n) _____ (adverb) _____ (adjective) roommate, and the _____ (noun) to end all _____ (plural noun). I couldn't imagine grad school any other way. Congratulations, and thanks for being so awesome.

To Daisy Sudparid, for being my rock even when you couldn't, for being so understanding even when it was hard, and for being my perpetual cheerleader even when you needed one yourself. There are no words to describe how much I appreciate everything you are and do. I cannot imagine how I would have gotten here without you and am really lucky I don't have to find out. Thank you times infinity.

Finally, to the many others who have inspired, motivated, supported, pushed, enlightened, and entertained me through this process; to Dr. Victor Donnay for introducing me to mathematical biology; to the NSF for funding through grants DGE-0217424 and DMS-0354259; to EDGE for travel assistance and for the amazing community of mathematicians, I thank you.

CHAPTER 1

INTRODUCTION

Type 2 diabetes mellitus is an epidemic that affects more than 25 million individuals in the United States and an additional 330 million worldwide [19]. As the seventh leading cause of death in the United States, it significantly increases the risk of cardiovascular disease and stroke and costs hundreds of billions of dollars each year in healthcare, work loss, disability services [3]. Yet, there is no cure.

There are two major players in diabetes manifestation: glucose and insulin. The disease itself is defined by excessive plasma glucose concentrations, i.e., hyperglycemia, brought on by insulin insufficiency. Glucose is utilized by most cells to create energy and can be produced by the liver or external sources, such as food. Insulin is its major inhibitor and is secreted by pancreatic β cells in response to elevated glucose to facilitate cellular glucose uptake from the blood [25, 36]. Type 2 diabetes is one of two major classes of diabetes, the other being type 1 diabetes. The latter results from an immune-mediated destruction of pancreatic β cells and is usually diagnosed in childhood. Individuals with type 1 diabetes produce very little to no insulin and thus require exogenous insulin to regulate glucose concentrations. Furthermore, precipitating events that initiate complete β-cell loss lead to a rapid progression of overt diabetes [57]. Type 2 diabetes, on the other hand, is characterized by a relative insulin deficiency, wherein the insulin that is secreted from β cells is insufficient to meet metabolic demands. This disease is often associated with obesity, is diagnosed later in life, and has a slow progression [100].

Genetic and environmental susceptibility factors determine the presence of type 2 diabetes in the general population. Yet, the onset of disease results from any combination of a multitude of genes and environmental components, which can ultimately affect several aspects of metabolic regulation, so that the development of such a complex disease cannot be explained by a characteristic set of susceptibility factors [53, 69]. Nevertheless, there are two conditions that are central to disease development, and several mechanisms have been proposed to explain their individual progression. First, the majority of type 2 diabetics exhibit reduced re-

sponsiveness to insulin, called insulin resistance. Second, β cells of susceptible individuals do not secrete enough insulin to meet metabolic demands, defining a state of β-cell decompensation, dysfunction, or failure [66, 78]. Together, insulin resistance and β-cell dysfunction define a timeline to diabetes. Eventual type 2 diabetics exit a state of normal glucose metabolism, in which insulin sufficiently caters to metabolic requirements, and enter one of insulin resistance, which can reduce glucose uptake from the blood or increase endogenous glucose production. A compensatory response by β cells increases plasma insulin levels, causing hyperinsulinemia. This condition can last for several years, until β-cell decompensation occurs, initiating the severe hyperglycemia that defines the overt diabetic state [100].

Although insulin resistance and β-cell decompensation compose the well accepted basis of type 2 diabetes, the molecular mechanisms underlying their development are incompletely understood [53,69]. In this work, we present long-term mathematical models describing proposed mechanisms to assess their roles in metabolic regulation and disease progression (Figure 1.1) and to fill the gap in existing long-term models of type 2 diabetes [24,96], which do not provide a mechanistic basis for these fundamental pathological conditions.

In this work, we define type 2 diabetes as a disease that coordinates metabolic dysfunction on multiple biological levels, including plasma, cellular, intracellular, and molecular. Abnormalities on the plasma scale are caused by tissue and cellular defects, which are themselves acquired by intracellular and molecular impairments. At the tissue and cellular levels, we restrict ourselves to dynamics associated with skeletal muscle and β cells for the following reasons: Skeletal muscle accounts for roughly 75% of all insulin-mediated glucose uptake upon meal ingestion, and in type 2 diabetics, the rate at which glucose is utilized is decreased by 50% [25,87]; type 2 diabetes development requires β-cell dysfunction on top of insulin resistance, as insulin resistance alone cannot produce diabetes [7, 47, 66]. We therefore explore mechanisms underlying the progression of both skeletal muscle insulin resistance and functional compensation and decompensation by β cells.

Insulin resistance is characterized by impaired insulin signaling, in which elements of the associated pathway reduce insulin's ability to adequately facilitate cellular glucose uptake [48, 101]. Of the proposed mechanisms for skeletal muscle dysfunction, we center our work on the effects of dietary excess in the development of oxidative stress and the related dysfunction of energy-producing mitochondria. Oxidative stress is an accumulation of toxic reactive oxygen species, which are standard by-products of glucose metabolism and energy production by mitochondria. This suggests a role for mitochondrial function in disease pathogenesis, as

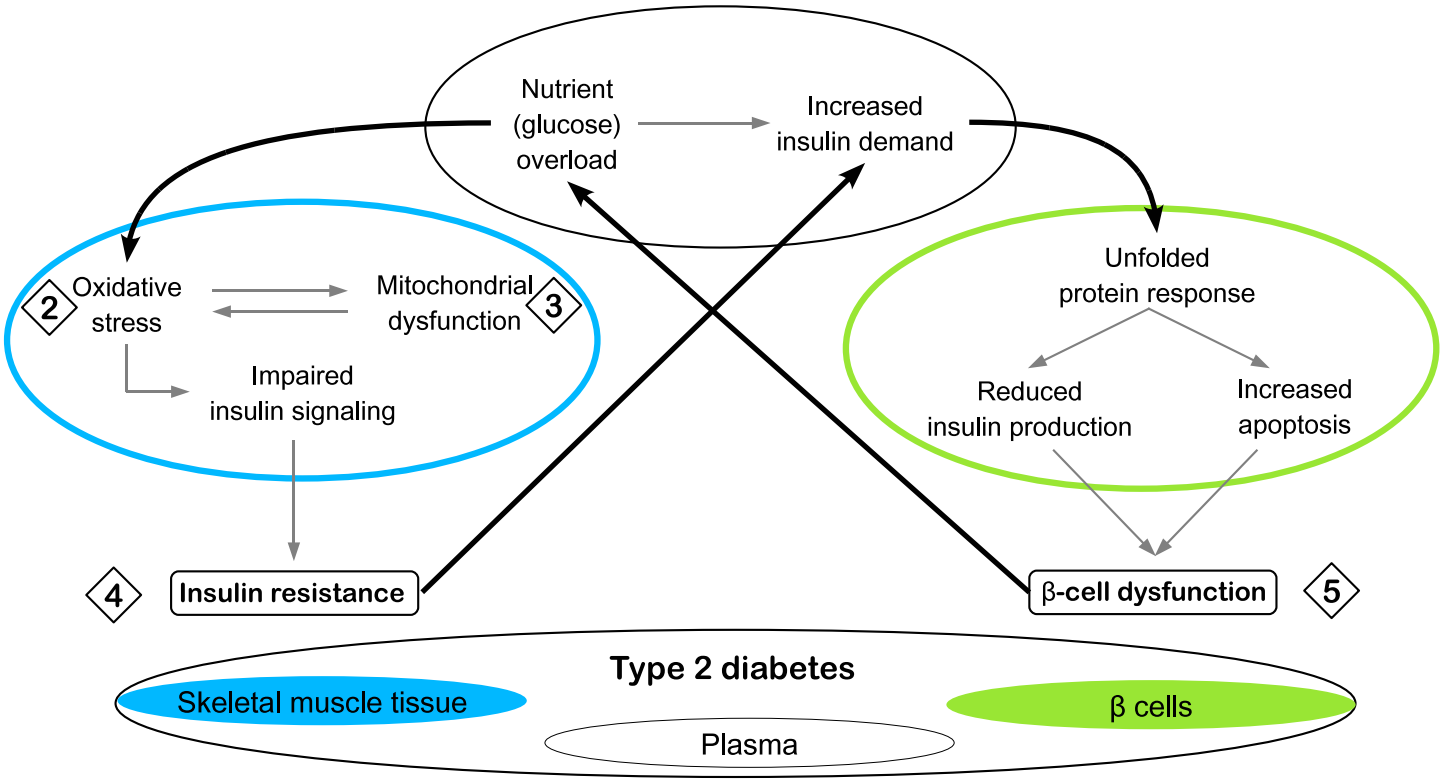

Figure 1.1. Mechanisms of type 2 diabetes progression. The disease is an amalgamation of plasma, cellular, intracellular, and molecular defects, centered on the presence of insulin resistance and β-cell failure. The current work explores disease development specifically within skeletal muscle and pancreatic β cells, highlighting proposed mechanisms of their dysfunction. In skeletal muscle cells, overnutrition leads to oxidative stress and mitochondrial abnormalities. These interact with each other to facilitate insulin signaling defects in the cell, leading to insulin resistance. Such resistance increases the metabolic demand for insulin and, consequently, the β-cell workload. Prolonged, elevated β-cell loads activate the unfolded protein response, which can promote or limit the amount of insulin secreted by β cells, as well as trigger apoptosis. Thus, constitutive activation of the unfolded protein response can lead to a failure in β cells to properly regulate glucose. Numbers 2 through 5 correspond to the chapters in which labeled mechanisms are discussed.

mitochondrial dysfunction can arise from excessive generation of reactive oxygen species and can provide positive feedback for oxidative stress [44]. We highlight these as important mechanisms in the progression of skeletal muscle insulin resistance because of their connection to the insulin signaling pathway and their potential for systemic dysfunction.

β-cell function is defined by insulin production and β-cell expansion, both of which increase in response to glucose [100]. The proposed mechanism for β-cell dysfunction lies in the unfolded protein response mounted by the endoplasmic reticulum in conditions of stress. This response, a protective mechanism to prevent β cells from being overworked, can be activated by a prolonged, increased demand for insulin [66]. However, when the response itself is activated for too long, which reflects an inability to restore cellular homeostasis, apoptotic pathways can be triggered [7]. The mechanism of β-cell failure suggested by the unfolded protein response allows for a biological description of insulin production, while providing essential feedback in the presence of elevated insulin requirement. This mechanism also addresses the notion of β-cell loss, which has been associated with type 2 diabetes, albeit with widely varying results [18, 40, 77].

It is evident that type 2 diabetes is a symphony of dysfunction, as its pathogenesis relies heavily on the interplay of destructive mechanisms that cause both insulin resistance and β-cell failure. We use subsequent chapters to present mathematical models of these long-term processes and their effects on glucose regulation. Chapter numbers and their corresponding mechanisms appear in Figure 1.1. In Chapter 2, we develop a deterministic model of the production of mitochondrial superoxide, a type of reactive oxygen species, and the effects of exogenous glucose on the presence of oxidative stress. In Chapter 3, we use deterministic and stochastic methods to model heterogeneities among mitochondria within skeletal muscle cells, along with feedback between oxidative stress and mitochondrial damage. In Chapter 4, we utilize a continuous model of the insulin signaling pathway, modulated by reactive oxygen species and mitochondrial damage, to create a mechanistic model of the progression of skeletal muscle insulin resistance. In Chapter 5, we deterministically model β-cell function at the molecular and population levels, as affected by the unfolded protein response, and we explore the effects of insulin resistance and β-cell dysfunction on glucose regulation. Finally, we use Chapter 6 to summarize and outline future extensions of the work presented herein.

CHAPTER 2

MITOCHONDRIAL PRODUCTION OF REACTIVE OXYGEN SPECIES IN GLUCOSE DYSREGULATION

Glucose is a major source of cellular energy and is utilized in many tissues including neural, skeletal muscle, hepatic and adipose tissues. Exogenous and endogenous sources, such as diet and liver production, respectively, add to plasma levels [25, 95]. Excess glucose can lead to severe health complications, including type 2 diabetes mellitus. For this reason, effective regulation by pancreatic hormones is required.

The pancreas comprises two major cell types: exocrine and endocrine. Exocrine cells, which include acinar and duct cells, are essential in the digestive process. Scattered among acini are endocrine cells, which are hormone-secreting cells located in the numerous pancreatic Islets of Langerhans. Together, these cells account for $1-2\%$ of the entire human pancreas [75, 86] and are composed of α, β, δ, ε, and PP cells [38]. The islets predominately contain α and β cells, the latter accounting for $50-80\%$ of all islet cells [68, 75, 86]. Both cell types have significant roles in regulating glucose homeostasis: Glucagon from α cells, secreted in response to low plasma glucose concentrations, leads to increased hepatic glucose output and reduced glycolysis; β-cell-derived insulin reduces blood glucose levels by stimulating glucose transport into target tissues and suppresses hepatic glucose production [23, 75].

A reduced physiological response to normal amounts of insulin is termed insulin resistance, which is characterized by an impairment in the insulin signaling pathway of hormone-responsive cells and is a major factor in type 2 diabetes pathogenesis. Although insulin resistance occurs on the whole-body level, skeletal muscle is a primary culprit in its development, as the majority of insulin-stimulated glucose uptake occurs in this tissue type [10, 25]. In the absence of other dysfunction, it is unclear how skeletal muscle fibers become and remain insulin resistant and how this state propagates throughout the majority of skeletal muscle tissues [1, 43], but the mitochondrion has been implicated as an integral piece of the puzzle [13, 43, 49]. Glycolytic end-products are utilized to facilitate energy production within this organelle, which

connects energy demand to nutrient availability. During this process of cellular respiration, toxic reactive oxygen species (ROS) are generated as a typical by-product. These are readily removed by protective antioxidant mechanisms present in mitochondria and cytosol alike, but cellular or mitochondrial dysfunction, along with nutrient excess, can alter the removal efficacy and rate of production, leading to an accumulation of ROS, termed oxidative stress [31].

In the presence of such stress, mitochondria can undergo a variety of changes, particularly in their deoxyribonucleic acid (DNA), which is notoriously susceptible to oxidative stress-mediated mutagenesis and damage [4, 52]. Because skeletal muscle tissue is post-mitotic, nuclear DNA modifications are considerably less common, and the effects of cytosolic ROS are more often manifest in the activation of cellular stress signals and their downstream targets [8, 10]. The insulin signaling cascade is one such target, highlighting the basis of the oxidative stress-centered hypothesis in the development of insulin resistance [94].

Generated primarily by muscle mitochondria, superoxide is a highly toxic ROS. Intracellular and mitochondrial protective mechanisms, such as superoxide dismutase, prevent most superoxide from causing damage. The manganese form of superoxide dismutase (MnSOD) resides in the mitochondrial matrix, and its reaction with superoxide results in the formation of hydrogen peroxide, a less toxic ROS [35] that can impede insulin signaling [104]. Thus, in order to determine how insulin resistance develops, it is essential to understand mitochondrial superoxide production and its effects, which is the focus of this chapter (Figure 2.1, blue text). This component of insulin resistance progression can then give way to additional mechanisms that are associated more directly with dysfunctional glucose uptake (Figure 2.1, black text).

Mitochondrial superoxide production is primarily the result of intracellular glucose metabolism (Figure 2.2). Upon entering the skeletal muscle cell, glucose is broken down into pyruvate, which then enters the mitochondrial matrix and produces pairs of electrons that pass through the electron transport chain (ETC). Each electron pair travels through ETC Complexes I and III, initiating a series of redox reactions that allow complex proteins to switch between oxidized and reduced states [88]. These reactions release energy that is used to pump protons from the matrix into the intermembrane space, generating a potential gradient. At complex IV, the electrons are passed to free oxygen and matrix protons to create water molecules. The electrochemical potential energy created by the proton gradient in the intermembrane space is used to power adenosine triphosphate (ATP) production, after which protons can flow back into the matrix. Electrons can also be dropped from the ETC, which allows them to react with the abundant oxygen molecules to form superoxide.

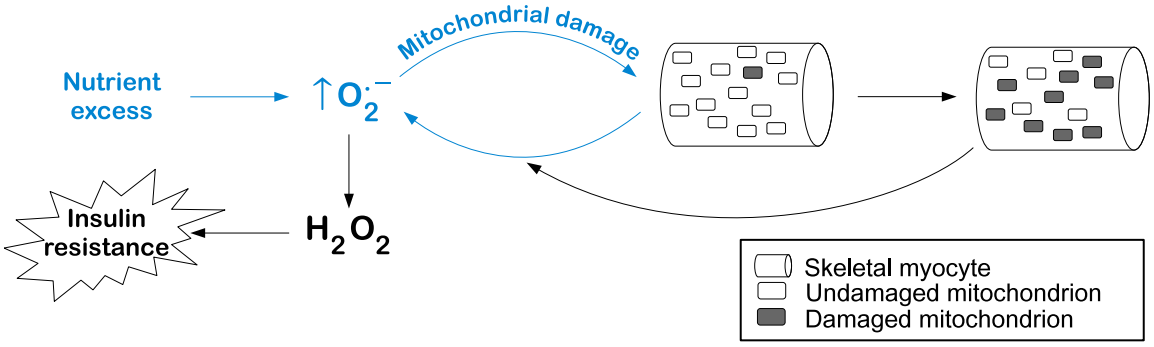

Figure 2.1. Illustration (blue text and symbols) of the primary focus of Chapter 2. Glucose or nutrient excess generates increased concentrations of mitochondrial superoxide, which are elevated further by intramitochondrial feedback. This leads to a state of oxidative stress within mitochondria and a role for superoxide in the progression of insulin resistance. $O_2^{\cdot -}$: superoxide; H_2O_2: hydrogen peroxide.

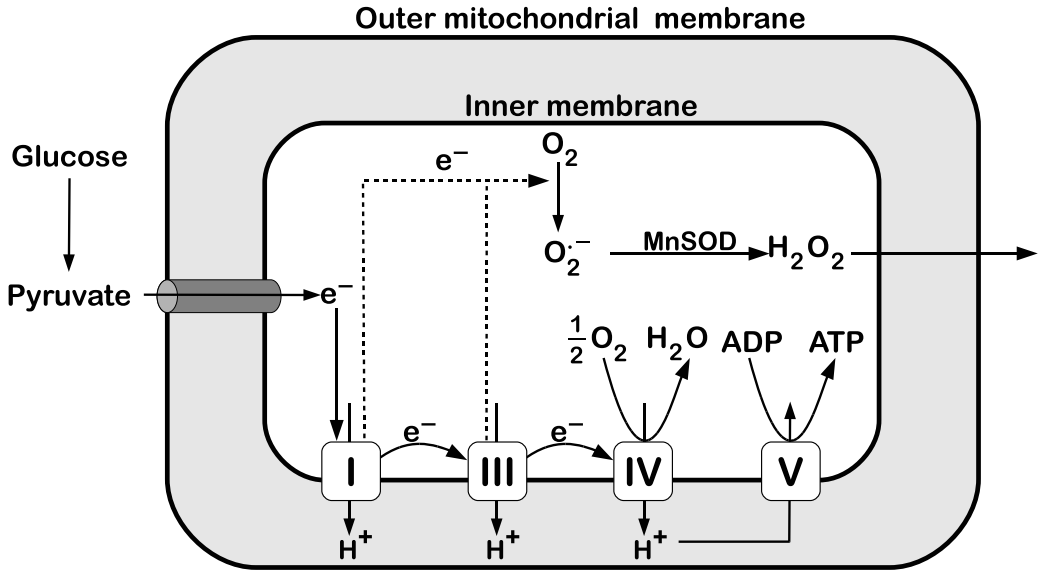

Figure 2.2. Oxidative phosphorylation and superoxide production. Glucose metabolism gives rise to pyruvate, which is transported into the mitochondrion. A series of redox reactions result in the generation of electron pairs that are to flow through the electron transport chain (ETC). Complexes I and III contain a myriad of proteins that are alternately reduced and oxidized. These reactions create energy used to pump protons from the mitochondrial matrix into the intermembrane space, thus generating a potential gradient. At the end of the chain, electrons are used to form water, and the electrochemical energy is used to power ATP production, allowing protons to return to the matrix. Electrons in Complexes I and III can leak from the ETC into the mitochondrial matrix, allowing for their reduction of oxygen to form superoxide. The anion is detoxified by antioxidant enzyme MnSOD, yielding hydrogen peroxide. ADP: adenosine diphosphate; ATP: adenosine triphosphate; e^-: electron; H^+: proton; H_2O: water molecule; H_2O_2: hydrogen peroxide; MnSOD: manganese superoxide dismutase; O_2: oxygen molecule; $O_2^{\cdot -}$: superoxide.

Energy use provides positive feedback on its production, but in a state of lower ATP utilization, the rate of glycolysis slows, resulting in decreased energy production. A combination of reduced energy use and heightened glucose uptake, which can represent a sedentary lifestyle and overeating, results in an excess of ATP, a depletion of adenosine diphosphate (ADP), and an elevated proton gradient. If the potential energy created by protons cannot be released, electron flow is retarded, but the constant influx of nutrient-derived electrons causes them to aggregate in complexes I and III. Electron leakage into the mitochondrial matrix then becomes more likely, resulting in increased rates of superoxide production [99].

In this chapter, we develop a mathematical model of mitochondrial superoxide production to determine the effects of nutrient overload on the oxidative state of skeletal muscle cells.

2.1 Model of mitochondrial superoxide production

Figure 2.3 is a schematic of the full model, which contains two major components: the glucose-insulin regulatory system and the intramitochondrial system.

2.1.1 Glucose-insulin subsystem

The glucose-insulin regulatory system is the point of contact for many metabolic abnormalities (Equations (2.1)). The state variables for this subsystem are plasma glucose, $G(t)$; plasma insulin, $I(t)$; and intracellular glucose, $G_i(t)$.

$$\text{Plasma glucose:} \quad \frac{\mathrm{d}G}{\mathrm{d}t} = \sigma + h_g - k_g G - SGI \tag{2.1a}$$

$$\text{Plasma insulin:} \quad \frac{\mathrm{d}I}{\mathrm{d}t} = h_i B \frac{G^4}{G^4 + G_h^4} - k_i I \tag{2.1b}$$

$$\text{Intracellular glucose:} \quad \frac{\mathrm{d}G_i}{\mathrm{d}t} = v_1 \cdot SGI - k_{gi} G_i. \tag{2.1c}$$

- *Plasma glucose.* Sources of glucose include both endogenous and exogenous factors. Most of the internally created glucose is derived from the liver, while diet provides external glucose. Removal of glucose from the blood can occur via insulin-dependent and -independent means. While the brain takes in glucose at a constant rate and independently of any other signals, skeletal muscle cells require insulin to facilitate glucose internalization [25]. The Bergman Minimal Model for the assessment of insulin sensitivity, which models the changes in plasma glucose and an insulin action variable, is often used to describe glucose dynamics [11]. The insulin action compartment serves as a transitional reservoir for plasma insulin input and is assumed to facilitate glucose uptake directly, thus representing the delay between insulin appearance in the blood and its

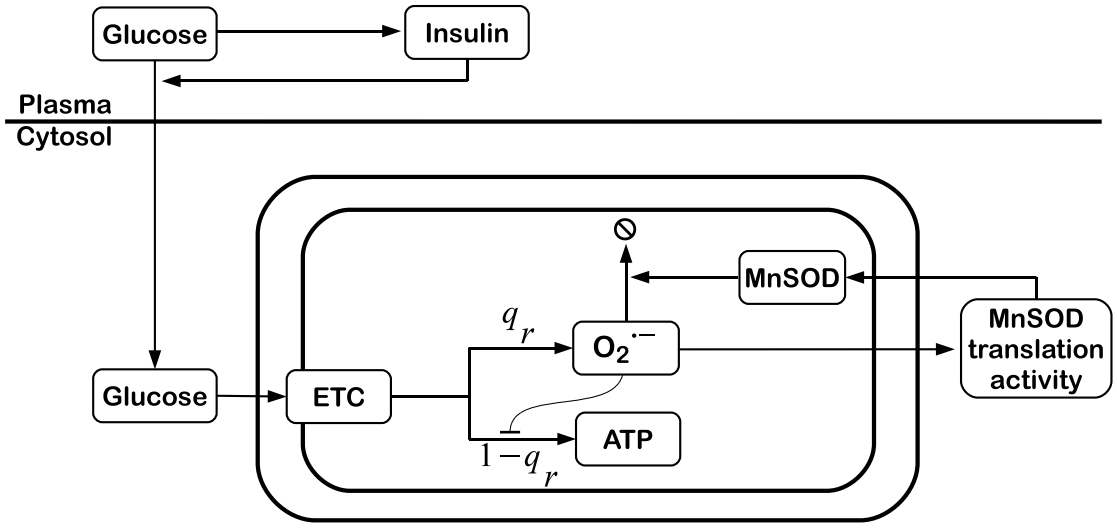

Figure 2.3. Details of the mitochondrial superoxide production model. Glucose uptake leads to ETC activation and ATP production. A fraction q_r of cellular respiration results in superoxide formation, with the remainder dedicated to energy production. Superoxide reduces mitochondrial efficiency in generating ATP, thereby decreasing the fraction of proper respiratory activity and increasing its own production. Superoxide also enhances MnSOD production, which works to remove the anion from the mitochondrion. ATP: adenosine triphosphate; ETC: electron transport chain; MnSOD: manganese superoxide dismutase; $O_2^{\cdot-}$: superoxide.

regulatory action on glucose. Because glucose and insulin responses occur on the order of minutes, subsequent adaptations of the Minimal Model that account for long-term dynamics [24, 96] make a quasi-steady state approximation of insulin action, resulting in a single equation to describe the change in plasma glucose. This is the form used in Equation (2.1a).

The source term h_g describes endogenous glucose production from the liver, while insulin-independent plasma glucose uptake occurs at a constant rate k_g. To reflect the dependence of peripheral tissues on insulin, the rate of uptake is assumed to be proportional to the concentrations of glucose and insulin with constant rate parameter S, often referred to as the insulin sensitivity parameter [12, 24, 96].

We modify the form of previous models with the time-dependent rate parameter $\sigma(t)$, which accounts for dietary intake and consequent glucose absorption into the blood. σ varies according to the average daily change from baseline (G_0) in the glucose area under the curve, which we denote by ΔAUC (Figure 2.4). Let T be the appropriate number of time units in a given day. Then

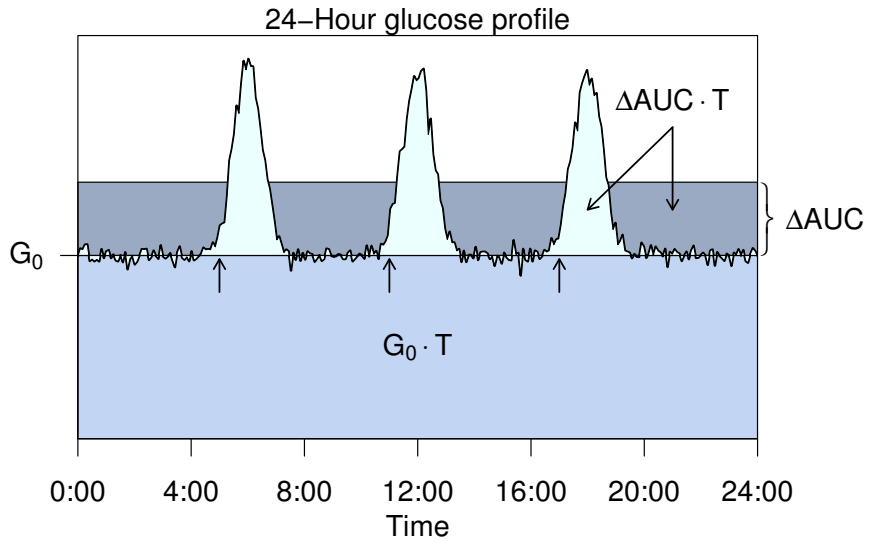

Figure 2.4. Sample 24-hour glucose profile and illustration of ΔAUC. The fasting glucose area under the curve is given by G_0T. Each peak corresponds to the ingestion of a meal (↑) and subsequent appearance in the blood. The net area beneath these three curves is the cumulative change above fasting and the average change is this quantity divided by T. ΔAUC is defined to be the average change, so that the area given by $\Delta\text{AUC}\cdot T$ is equivalent to the total area beneath the curve.

$$\Delta\text{AUC} = \frac{1}{T}\int_0^T (G(t) - G_0)\,\mathrm{d}t = \frac{1}{T}\int_0^T G(t)\,\mathrm{d}t - G_0.$$

We assume that a glucose concentration of G_0 corresponds to hepatic input h_g, so that σ is proportional to h_g, scaled by the ratio of ΔAUC to baseline glucose:

$$\sigma = h_g \frac{\Delta\text{AUC}}{G_0}. \tag{2.2}$$

In our model exploration, we simulate daily meals by defining $\sigma(t)$ as a square wave. The wave amplitude is then scaled according to the meal duration to ensure that the integrated wave over 24 hours equals the right-hand side of (2.2).

- *Plasma insulin.* The rate of insulin secretion is a sigmoidal function of glucose [36]. From the work of De Gaetano et al. [24], hormone production and release is modeled by a Hill function with coefficient 4 and maximal production rate $h_i B$, where B represents the number of β cells present (Equation (2.1b)). Insulin is cleared from the blood with rate constant k_i.

  Following an increase in blood glucose, β cells secrete insulin to allow for the return of glucose to its basal concentration, which is the typical metabolic response to dietary

intake. Although glucose always stimulates β-cell release of insulin into the blood, this secretion saturates for ever-increasing concentrations of glucose. β cells may adapt to changes in metabolic demand by either increasing their mass or function [86], and to eliminate the effects of compensatory β-cell behavior in the present framework, we assume B is constant.

- *Intracellular glucose.* The full amount of glucose removed from plasma is distributed evenly among skeletal muscle cells with conversion factor v_1 (Equation (2.1c)). Further, glycolysis, the process by which intracellular glucose is broken down for use in cellular respiration and subsequent ATP production, occurs at a constant rate k_{gi}. We apply this assumption presently to reduce the biological complexity of ATP production and utilization dynamics.

2.1.2 Mitochondrial subsystem

Glycolysis results in the creation of pyruvate, which is subsequently transported into the cell's mitochondria, setting the electron transport chain in motion. Because mitochondria are responsible for most superoxide produced in skeletal muscle fibers, we construct a model of the processes operating within an individual organelle (Figure 2.3). The model comprises two main pieces, one describing the ETC (Equations (2.3)), the other describing the causes and effects of superoxide (Equations (2.4)). The six state variables represented are oxidized and reduced ETC complex, $C_{ox}(t)$ and $C(t)$; superoxide, $R_s(t)$; antioxidant enzyme MnSOD, $A_s(t)$; MnSOD translation signal, $E(t)$; and mitochondrial inefficiency, $L(t)$.

Part I: ETC

Oxidized ETC complex:
$$\frac{\mathrm{d}C_{ox}}{\mathrm{d}t} = -v_2 N_e \cdot k_{gi} G_i C_{ox} + k_c[(1-q_r)(1-L)+q_r]C \tag{2.3a}$$

Reduced ETC complex:
$$\frac{\mathrm{d}C}{\mathrm{d}t} = v_2 N_e \cdot k_{gi} G_i C_{ox} - k_c[(1-q_r)(1-L)+q_r]C \tag{2.3b}$$

Part II: Superoxide

Superoxide:
$$\frac{\mathrm{d}R_s}{\mathrm{d}t} = k_c q_r C - k_{rs} R_s A_s \tag{2.4a}$$

MnSOD:
$$\frac{\mathrm{d}A_s}{\mathrm{d}t} = a_a E - q_a k_{rs} R_s A_s \tag{2.4b}$$

MnSOD translation signal:
$$\frac{\mathrm{d}E}{\mathrm{d}t} = a_e R_s (1-E) - k_e E \tag{2.4c}$$

Mitochondrial inefficiency:
$$\frac{\mathrm{d}L}{\mathrm{d}t} = \xi\left(1 - \frac{R_{s0}}{R_s}\right)(1-L) \tag{2.4d}$$

- *Electron transport dynamics.* We condense the ETC complexes into a single representative entity; the proteins housed in this complex can assume either an oxidized or a reduced state (Equations (2.3a) and (2.3b)). Glucose processing results in the immediate donation of electrons to the ETC, where N_e is the number of electrons created per glucose concentration and v_2 accounts for pyruvate entry into a single mitochondrion. The transfer of electrons leads to a reduction reaction, transferring proteins from the oxidized state (C_{ox}) to the reduced state (C). Because the release of electrons immediately precedes ATP production, we assume these events occur in tandem; therefore, the electron-free complex returns to an oxidized state with rate $k_c(1-q_r)$. A fraction q_r of respiration leads to the formation of superoxide, which also decreases the contribution of reduced complex toward ATP production.

  Based on studies of isolated mitochondria, between 0.12% and 4% of all cellular respiration is thought to result in superoxide formation [8, 31, 49, 98]. However, the *in vivo* percentage is most likely much smaller due to experimental conditions [67]. Specifically, the supraphysiological concentrations of ETC substrates and oxygen used in isolation favor the reduction of ETC complexes; with higher oxygen concentrations, the likelihood of electron transfer from reduced substrates to oxygen increases further [32]. Therefore, we assume q_r is small.

  Mitochondrial dysfunction increases with age, and the source of such dysfunction is believed to be an accumulation of mutations in mitochondrial DNA (mtDNA) [9, 14, 44]. The proximity of the site of superoxide production to that of mtDNA enhances mitochondrial susceptibility to mutagenesis, which results in a progressive increase in mutation number. When 35% of mtDNA encodes for genes involved in electron transport, it stands to reason that an increased mutation number will affect proper electron transport [92]. We assume oxidation is slowed by mitochondrial inefficiency, L, which increases with age. Such dysfunction is presumed to affect the proper transport of electrons through the entire complex. Therefore, the rate at which ATP production proceeds is limited by the efficiency factor $(1-L)$. It is also assumed that L progresses uniformly in all mitochondria.

  Because the right-hand sides of Equations (2.3a) and (2.3b) sum to zero, $C_{tot} = C_{ox} + C$ is constant, and $C_{ox} = C_{tot} - C$. Substituting into Equation (2.3b) gives

$$\frac{\mathrm{d}C}{\mathrm{d}t} = v_2 N_e \cdot k_{gi} G_i (C_{tot} - C) - k_c[(1-q_r)(1-L) + q_r]C \tag{2.4e}$$

to describe the dynamics of the electron transport chain complex in terms of its reduced form.

- *Superoxide.* Equation (2.4a) describes the change in the concentration of mitochondrial superoxide over time. The sole source of superoxide is electron leakage from the reduced ETC complex, and the rate of antioxidant-mediated dismutation is first-order with respect to superoxide and MnSOD.

- *Manganese superoxide dismutase.* Nuclear translation of MnSOD requires an upregulation signal with the ability to communicate between superoxide and transcription machinery. Such a signal may come from NF-κB, FoxO, and CREB proteins, which respond to elevated superoxide levels [65, 73]. Although superoxide is eliminated by antioxidants, its highly toxic nature subjects mitochondria and their proteins, antioxidant enzymes included, to oxidative damage.

  We therefore model MnSOD along with its translation signal (Equations (2.4b) and (2.4c)). MnSOD is produced at maximal rate a_a, scaled by the strength of its translation signal, which ranges from zero and one. To reflect the potential damage to MnSOD caused by superoxide, we assume that a small fraction q_a of the MnSOD-superoxide reactions lead to antioxidant degradation; the enzyme MnSOD is otherwise undamaged. Inactive translation signaling, $(1-E)$, may be activated with an increase in superoxide at rate a_e. In the absence of superoxide stimulation, this signal decays by reverting to its inactive form.

- *Mitochondrial inefficiency.* Superoxide is often generated near the ETC, which is in close proximity to mtDNA molecules in the inner mitochondrial membrane. Mutagenic lesions are formed when superoxide oxidizes guanine bases in the mtDNA, which leads to higher mutation frequencies. The mutations themselves may slowly accumulate in mitochondria when repair mechanisms fail, which is why mitochondria of aging organisms are characterized by a number of mtDNA mutations that have developed over several decades [9, 76].

  We let L denote the fractional inefficiency of mitochondria due to the build up of mutated mtDNA (Equation (2.4d)) and assume that concentrations of R_s greater than the basal level, R_{s0}, lead to the progressive deterioration of mitochondrial ETC function. Because mitochondrial dysfunction changes very slowly, the rate parameter ξ is small compared to the others in this subsystem.

2.2 The effect of glucose input

To assess the role of exogenous glucose in superoxide production, we numerically solve Equations (2.1) and (2.4) for a period of 120 years with hourly increments, according to the parameters in Table 2.1. For these solutions, we vary the nutrient intake parameter σ periodically according to the formula (2.2), with ΔAUC ranging between 0 and 4.0 [17]. Henceforth, model results will be discussed in terms of ΔAUC. A description of all parameters appears in Table 2.1.

We present trajectories for intracellular glucose (G_i), the ETC complex (C), superoxide (R_s), MnSOD translation activity (E), MnSOD (A_s), and mitochondrial inefficiency (L) over a 120-year period (Figure 2.5). The system is assumed to be in equilibrium at $t = 0$ for ΔAUC = 0, and the corresponding initial conditions are made identical for all ΔAUC. With the exception of mitochondrial inefficiency, each variable experiences rapid oscillations due to the daily glucose input, the wide bands reflecting the short-term response of the system. Intracellular glucose, as expected, exhibits higher amplitudes with increased ΔAUC, promoting the reduction of the ETC complex. More dramatic oscillations and elevated levels of reduced complex are associated

Table 2.1. Parameter descriptions for Equations (2.1) and (2.4). A summary of all values used appears in Table A.1.

Parameter	Description	Units
a_a	MnSOD production	min^{-1}
a_e	MnSOD signal activation	min^{-1}
B	β-cell mass	10^6 cells
G_h	half-maximal glucose stimulation	mM
h_g	hepatic glucose production	mM min^{-1}
h_i	insulin production	$(10^6 \text{ cells})^{-1} \text{ min}^{-1}$
k_c	cellular respiration	min^{-1}
k_e	MnSOD signal deactivation	min^{-1}
k_g	insulin-independent glucose uptake	min^{-1}
k_{gi}	glycolysis	min^{-1}
k_i	insulin clearance	min^{-1}
k_{rs}	superoxide dismutation	$\mu\text{M}^{-1} \text{ min}^{-1}$
N_e	produced electrons	mM^{-1}
q_a	MnSOD damage probability	#
q_r	fractional superoxide production	#
S	insulin sensitivity parameter	$\text{pM}^{-1} \text{ min}^{-1}$
σ	food intake parameter	mM min^{-1}
υ_1	glucose distribution factor	#
υ_2	ETC conversion factor	#
ξ	mitochondrial dysfunction growth	d^{-1}

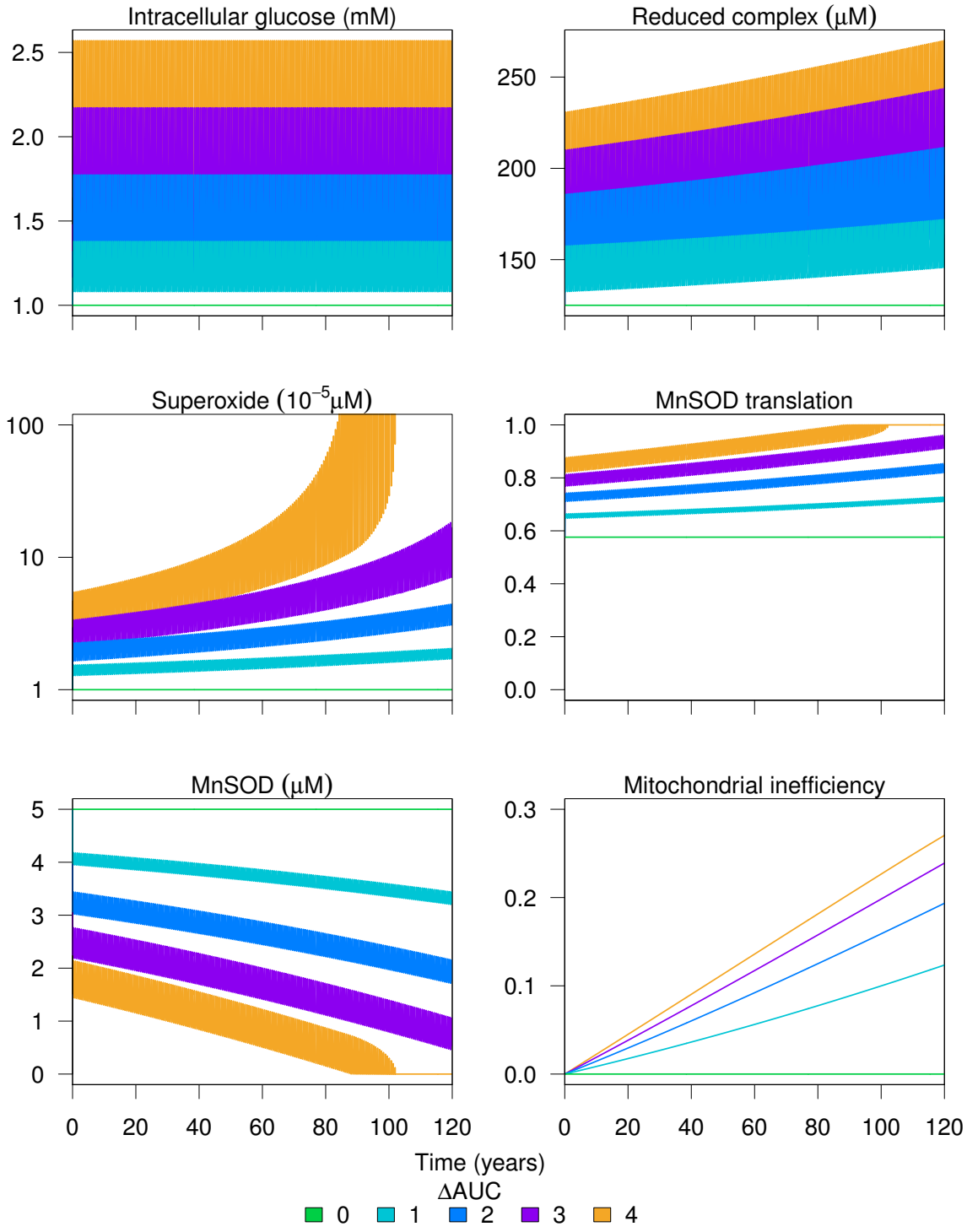

Figure 2.5. Long-term trajectories for the mitochondrial variables of the superoxide production model for various ΔAUC. Wide bands reflect rapid daily oscillations.

with larger ΔAUC, leading to increased superoxide production. The strength of the MnSOD translation response is heightened in the presence of superoxide, leading to fluctuating MnSOD concentrations. However, the antioxidant itself oscillates at lower levels as ΔAUC increases. Finally, mitochondrial inefficiency dictates long-term dynamics, as it rises slowly over time.

Progressive mitochondrial dysfunction leads to a slow increase in the reduction of the ETC complex, which in turn increases superoxide production. With a further decline in antioxidant capacity, superoxide levels continue to rise, well beyond the low steady-state level of 10^{-5} μM. Higher dietary intake, as measured by ΔAUC, hastens the process of destruction. There exists an unrealistically large equilibrium concentration of superoxide as time progresses indefinitely (not shown). Below a critical MnSOD threshold, which depends on existing mitochondrial dysfunction, the superoxide concentration will experience a more drastic elevation. Eventually, the ever-declining antioxidant capacity results in extreme superoxide levels, for any positive ΔAUC.

The full model of mitochondrial superoxide production highlights two important feedback loops from the perspective of superoxide concentration. On the one hand, there exists a positive feedback of superoxide on its own production, by way of mitochondrial inefficiency. In the short term, superoxide is created as a simple by-product of cellular respiration. However, the slower decline in mitochondrial function eventually decreases the amount of reduced complex used for ATP production. The result is a larger pool of reduced complex available for electron leakage and subsequent superoxide generation. The persistence of such interactions generates further organelle dysfunction and still higher superoxide concentrations.

Because superoxide stimulates the production of MnSOD, it facilitates a process that predominately leads to its own decline. In the short term, the efficacy with which MnSOD dismutates superoxide successively controls anion concentrations in a negative feedback loop. Further increases in superoxide produce more MnSOD within the limits of the translation signal. The longer term process of slight antioxidant damage, combined with the positive feedback, shifts the balance in favor of superoxide.

2.2.1 Time-scale analysis

To determine the relative effect of mitochondrial inefficiency and nutrient excess on the production of superoxide, we carry out a time-scale analysis on the present model. The slow dynamics of $L(t)$ allow for the rescaling of time based on the order of ξ. Let $\tau = \varepsilon t$ for ε satisfying $\xi = \varepsilon\bar{\xi}$. We may then rewrite the full system, with each variable redefined in terms

of τ, in the form of Equations (2.5):

$$\varepsilon\frac{\mathrm{d}G}{\mathrm{d}\tau} = \sigma + h_g - k_g G - SGI \tag{2.5a}$$

$$\varepsilon\frac{\mathrm{d}I}{\mathrm{d}\tau} = h_i B\frac{G^4}{G^4+9^4} - k_i I \tag{2.5b}$$

$$\varepsilon\frac{\mathrm{d}G_i}{\mathrm{d}\tau} = v_1 \cdot SGI - k_{gi} G_i. \tag{2.5c}$$

$$\varepsilon\frac{\mathrm{d}C}{\mathrm{d}\tau} = v_2 N_e \cdot k_{gi} G_i (C_{tot} - C) - k_c[(1-q_r)(1-L)+q_r]C \tag{2.5d}$$

$$\varepsilon\frac{\mathrm{d}R_s}{\mathrm{d}\tau} = k_c q_r C - k_{rs} R_s A_s \tag{2.5e}$$

$$\varepsilon\frac{\mathrm{d}A_s}{\mathrm{d}\tau} = a_a E - q_a k_{rs} R_s A_s \tag{2.5f}$$

$$\varepsilon\frac{\mathrm{d}E}{\mathrm{d}\tau} = a_e R_s (1-E) - k_e E \tag{2.5g}$$

$$\frac{\mathrm{d}L}{\mathrm{d}\tau} = \bar{\xi}\left(1 - \frac{R_{s0}}{R_s}\right)(1-L). \tag{2.5h}$$

Equations (2.5a) – (2.5g) define the fast subsystem of the model, while the slow subsystem is characterized by a single equation, (2.5h). The steady states of Equation (2.5h) are given by $R_s = R_{s0}$ and $L = 1$. Because the system is assumed to originate at equilibrium, we treat L as a parameter to determine its effect on the dynamics of the fast variables prior to reaching the terminal state of $L = 1$. In particular, we assume that ε is sufficiently small such that for each change in L, the fast subsystem has arrived at an equilibrium. Thus, as $\varepsilon \to 0$, we can calculate the quasi-steady-state expressions for the fast variables and make a series of substitutions to obtain a single formula for superoxide, R_s, as a function of both mitochondrial inefficiency L and meal intake parameter σ. Assuming a negligible effect of insulin-independent uptake ($k_g = 0$),

$$R_s(\sigma, L) = \frac{v_1 v_2 q_a q_r k_c k_e N_e C_{tot}(\sigma + h_g)}{a_e\left\{v_1 v_2 N_e(\sigma+h_g)(a_a - q_a q_r k_c C_{tot}) + a_a k_c[(1-q_r)(1-L)+q_r]\right\}}. \tag{2.6}$$

The right-hand side of Equation (2.6) is positive provided the denominator

$$\Theta = a_e\left\{v_1 v_2 N_e(\sigma+h_g)(a_a - q_a q_r k_c C_{tot}) + a_a k_c[(1-q_r)(1-L)+q_r]\right\} \tag{2.7}$$

is positive. Under certain combinations of L and σ, this expression may also equal zero exactly, thus defining the line $\Theta = 0$ as the catastrophic barrier. Figure 2.6 depicts the areas in which superoxide concentration exceeds physiological limits, as well as the impact of interactions between mitochondrial dysfunction and dietary excess. $\Theta = 0$ is the line separating the shaded and blank regions.

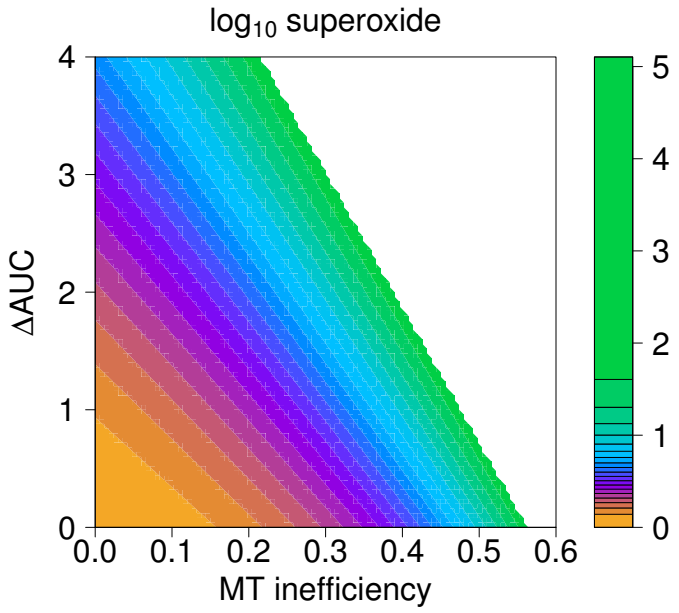

Figure 2.6. Map of steady-state superoxide in the fast subsystem based on ΔAUC and mitochondrial inefficiency. MT: mitochondrial.

As ΔAUC, and hence σ, increases, superoxide follows suit, even in the absence of mitochondrial dysfunction. The progression of inefficiency amplifies the effect of higher glucose input, to the extent that lower levels of mitochondrial inefficiency are sufficient to catapult superoxide well beyond reasonable limits.

2.3 Discussion

The model of superoxide production and damage highlights several important factors regarding the role of mitochondria in oxidative stress, along with the feedback mechanism underlying its development. Slow changes in mitochondrial inefficiency enhance the detrimental production of toxic superoxide. Many short-term feedback processes maintain a functioning metabolic system, such as the compensatory response in antioxidant production. However, the benefits of this response are reduced by superoxide's own destructive effects, particularly in the presence of nutrient excess.

The current model gives a semimechanistic view of superoxide production and identifies important features underlying it, but does so with a level of reduced complexity. A major simplification in the model is the omission of ATP dynamics and its impact on cellular glucose processing. The glycolytic pathway has several built-in feedback mechanisms that protect the cell and its machinery. In a state of low energy use and high glucose intake, there is an increase

in the cytosolic concentration of ATP. Glycolysis slows in the event of energy excess, resulting in a reduction of pyruvate entry into the mitochondrion and therefore diminished electron transport activity, which reduces superoxide production.

ATP availability depends on the ATP/ADP antiporter, which exchanges one molecule of mitochondrial ATP for cytosolic ADP. The total cellular concentration of adenine nucleotides remains fairly constant, which highlights the importance of energy utilization in electron transport. Once mitochondrial ADP is converted to ATP, a molecule of cytosolic ADP is required to transport newly formed ATP from the mitochondrion for cellular benefit. However, in the event of low energy utilization, fewer cytosolic ATP molecules are converted back into ADP, which reduces this molecule's presence in the cytosol. A deficiency in cytosolic ADP results in a buildup of mitochondrial ATP. Continued ATP production, within the limitations of the transmembrane potential, results in depletion of mitochondrial ADP [29]. If this occurs, electron transport activity stalls because of the large number of protons that have been pumped into the intermembrane space to power ATP production. A maximal electrochemical gradient potential prohibits further pumping of protons, which is required for the flow of electrons. Electrons already present in the ETC are then trapped, thus increasing the likelihood of leakage into the mitochondrial matrix and the consequent reduction of existing oxygen molecules [99]. ATP can both prevent and promote excessive mitochondrial superoxide production, and we eliminate these opposing actions by restricting ourselves to the general effects of nutrient overload and implicit ATP production.

In this chapter, we have described superoxide production and the positive feedback introduced by ROS-mediated mitochondrial dysfunction within an individual mitochondrion. The present model highlights defects of individual organelles from the perspective of ROS overproduction, but the progression of insulin resistance requires cellular dysfunction as well. We can exploit the former to describe the underlying causes of the latter. Heterogeneities among cellular components, such as mitochondria, and their relationship to superoxide can provide insights that extend beyond the current framework.

CHAPTER 3

THE DYNAMICS OF MITOCHONDRIAL DYSFUNCTION

Mitochondria are often referred to as the powerhouse of the cell. They are responsible for creating sufficient energy for normal cellular function, and they are capable of adapting their output to changing energy demands. In insulin resistance, they produce damaging superoxide anions that, in turn, do them harm. Like many machines, these organelles are susceptible to functional modifications that reduce their benefit to the cells in which they live. Mitochondrial alterations are often manifest in mutations to their DNA, but may extend to more general components, such as their size and ability to replicate [93, 107]. Through an integrated signal of health, the characteristics of the individual powerhouses can impact cellular-level functions, such as insulin signaling, thus highlighting a role for mitochondrial heterogeneity in the progression of insulin resistance (Figure 3.1).

Individual cells contain several hundred mitochondria, each of which in turn carry several copies of its mtDNA. A single cell thus contains thousands of mtDNA copies [92]. Given that mtDNA experiences rapid turnover, the composite effect of heterogeneous mtDNA and high

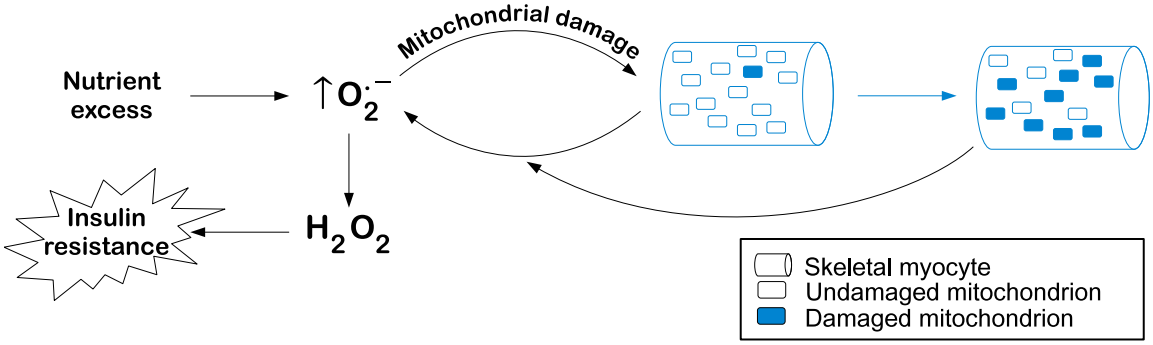

Figure 3.1. Illustration (blue text and symbols) of the primary focus of Chapter 3. Damage in an individual mitochondrion is selectively favored, as the cellular population of organelles continues to be infiltrated with damage. These mitochondria provide feedback to both cellular and mitochondrial function, supporting a role for mitochondrial heterogeneities and abnormalities in the progression of insulin resistance. $O_2^{\cdot -}$: superoxide; H_2O_2: hydrogen peroxide.

susceptibility to further mutations make repair mechanisms relatively inefficient [52]. The existence of multiple mtDNA copies with varying alterations is called heteroplasmy. This state, for any given mitochondrion, confers higher susceptibility to additional mutations upon the entire mitochondrial population. Mitochondrial fission can reduce the threat of heteroplasmy by diminishing the level of mtDNA mixing between different mitochondria, but this process is imperfect. As a last resort, mitophagy (mitochondrial autophagy) facilitates organelle turnover [27, 93, 99].

Oxidative stress increases the mutation rate of mtDNA, and hence, the likelihood of heteroplasmy. It also compromises the integrity of the mitochondrial permeability transition pore, leading to an influx of water and consequent swelling [107]. An increase in the volume of these damaged organelles decreases susceptibility to the protective scavenging mechanisms that carry out mitophagy, thus reducing their turnover rates in comparison to their healthier counterparts [64]. Further, damaged mitochondria are believed to have a replicative disadvantage [51], which may result from diminished responses to fission-inducing signals [93]. These ideas highlight two main differences between oxidatively damaged organelles and those experiencing normal levels of mutation: Mitophagy regulates the presence of excessive mtDNA heterogeneity within a single entity, but becomes less effective with oxidation-induced alterations; less defective mitochondria are better able to reproduce. Additionally, the physical and functional abnormalities accrued lead to increased ROS production [44], suggesting a role for the propagation of a damaged phenotype within the whole-cell population of mitochondria. In this chapter, we develop a mathematical model to describe selection in the mitochondrial population and explore its role in intracellular metabolic processes.

3.1 Models of mitochondrial selection

Given the changes in growth and turnover acquired by damaged mitochondria, we develop a mathematical model to describe damage selection in the cellular mitochondrial population. Although several levels of damage can exist, we consider two primary classes of mitochondria: undamaged and damaged (Figure 3.2). Let $\mathscr{C}_0$ and $\mathscr{C}_1$ denote these classes, respectively. Let μ be the probability that a $\mathscr{C}_0$ mitochondrion acquires enough damage to transition into $\mathscr{C}_1$, and assume that transitions occur when mitochondria replicate. We define the population sizes of these classes as $M_0(t)$ and $M_1(t)$. To determine the impact of long-term mitochondrial dynamics, we ignore transient plasticity and assume a constant population size K. Therefore, $K = M_0(t) + M_1(t)$ for all time t.

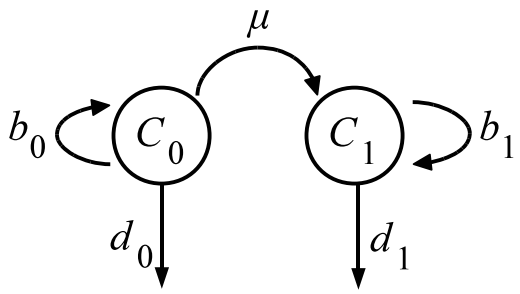

Figure 3.2. Schematic diagram for the mitochondrial selection model, which describes the population dynamics of two mitochondrial classes (undamaged, $\mathscr{C}_0$; damaged, $\mathscr{C}_1$). Healthy mitochondria can transfer to the damaged class with probability μ. Each class can replicate or experience turnover with varying rates, which are defined to demonstrate the selective differences between mitochondrial subpopulations. Each death is balanced by a birth, thus maintaining a constant population size.

Let b_0 and b_1 be the respective growth rates for $\mathscr{C}_0$ and $\mathscr{C}_1$. Similarly, let the turnover rates of these subpopulations be represented by d_0 and d_1. To incorporate the selective differences between $\mathscr{C}_0$ and $\mathscr{C}_1$, let s denote the fractional growth reduction of damaged mitochondria and c their fractional scavenging resistance. We then have

$$b_1 = (1-s)\,b_0, \tag{3.1}$$

$$d_1 = (1-c)\,d_0. \tag{3.2}$$

In this section, we utilize deterministic and stochastic methods to identify essential aspects of mitochondrial dynamics within the cellular landscape.

3.1.1 The deterministic approach

We construct a system of continuous-time ordinary differential equations to illustrate the dynamics of mitochondrial damage influenced by selection (Table 3.1, Equation (3.3)). The combined turnover of the population is the sum of the individual processes, which occur at rates proportional to the subpopulation sizes: $d_0 M_0 + d_1 M_1$. To ensure constant population size, assume each turnover event is balanced by a growth event, as determined by the relative growth rates of each population. Growth of the $\mathscr{C}_0$ population is contingent upon the failure to transition to a damaged state, which occurs with probability $(1-\mu)$.

Table 3.1. Parameter descriptions for Equations (3.3). A summary of all values used appears in Table A.1.

Parameter	Value/Range	Units
K	total population size	mitochondria
μ	damage transition probability	#
s	fractional growth deficit	#
c	fractional scavenging resistance	#
b_0	undamaged mitochondrial growth rate	d^{-1}
d_0	undamaged mitochondrial turnover rate	d^{-1}
b_1	damaged mitochondrial growth rate	d^{-1}
d_1	damaged mitochondrial turnover rate	d^{-1}

$$\frac{\mathrm{d}M_0}{\mathrm{d}t} = \underbrace{(d_0M_0 + d_1M_1)}_{\text{turnover}} \underbrace{(1-\mu)\frac{b_0M_0}{b_0M_0 + b_1M_1}}_{\mathscr{C}_0 \text{ growth}} - d_0M_0, \tag{3.3a}$$

$$\frac{\mathrm{d}M_1}{\mathrm{d}t} = (d_0M_0 + d_1M_1)\Big[\underbrace{\mu\frac{b_0M_0}{b_0M_0 + b_1M_1}}_{\text{transition}} + \underbrace{\frac{b_1M_1}{b_0M_0 + b_1M_1}}_{\mathscr{C}_1 \text{ growth}}\Big] - d_1M_1. \tag{3.3b}$$

We begin analysis of system (3.3) by defining $\pi(t) = \dfrac{M_0(t)}{K}$ as the fraction of undamaged mitochondria within a single cell. If this fraction is zero, we consider the cell to be in a state of total damage. Equations (3.3a) and (3.3b) then reduce to

$$\frac{\mathrm{d}\pi}{\mathrm{d}t} = [d_0\pi + d_1(1-\pi)](1-\mu)\frac{b_0\pi}{b_0\pi + b_1(1-\pi)} - d_0\pi, \tag{3.4}$$

which has the equilibrium values

$$\pi_1^* = 0 \qquad \text{and} \tag{3.5a}$$

$$\pi_2^* = \frac{(1-\mu)b_0d_1 - b_1d_0}{(1-\mu)b_0d_1 - b_1d_0 + \mu b_0d_1}. \tag{3.5b}$$

Stability analysis indicates that total damage of the skeletal muscle cell, that is, a population with no healthy mitochondria, occurs when

$$\frac{(1-\mu)b_0}{d_0} < \frac{b_1}{d_1}, \tag{3.6}$$

which is the stability condition for π_1^*. In terms of the selection parameter s and turnover factor c, the condition for destruction of all healthy mitochondria is $c > \dfrac{s-\mu}{1-\mu}$. If $\mu \ll 1$, then the extinction requirement reduces to $c > s$. Thus, if the scavenging resistance of $\mathscr{C}_1$ mitochondria is greater than the fitness penalty of damage, the system will favor total damage as $t \to \infty$.

3.1.2 The stochastic approach

Individual mutation events, like the transitions from $\mathscr{C}_0$ to $\mathscr{C}_1$, are rare and should be treated stochastically. We develop a stochastic model to track the number of damaged mitochondria in a cell. As in the deterministic system, we pair each turnover event with a growth event. The probability that a death will be replaced by a birth in one of the classes depends on the relative growth probability of either class, as in Equations (3.3). We can write a 2×3 transition matrix to describe all possible changes to both populations,

$$\begin{bmatrix} \Delta M_0 \\ \Delta M_1 \end{bmatrix} = \begin{bmatrix} \mathbf{a}_1 & \mathbf{a}_2 & \mathbf{a}_3 \end{bmatrix} = \begin{bmatrix} +1 & -1 & 0 \\ -1 & +1 & 0 \end{bmatrix}, \tag{3.7}$$

where ΔM_i is the change in the number of class i mitochondria ($i = 0, 1$), and we can simplify the accounting by explicitly including the possibility of no change.

We now define the probabilities associated with the transition events described in matrix (3.7). Let $p_i = \Pr(\mathbf{a}_1 | M_0 = i)$ and $q_i = \Pr(\mathbf{a}_2 | M_0 = i)$. Then $1 - p_i - q_i = \Pr(\mathbf{a}_3 | M_0 = i)$. Because $M_0 + M_1 = K$, we may replace M_1 with $K - M_0$. As p_i describes a gain of one in the healthy mitochondrial population of size i and q_i the equivalent loss, we can write

$$p_i = \underbrace{\frac{d_1(K-i)}{d_0 i + d_1(K-i)}}_{\text{death from } \mathscr{C}_1} \cdot \underbrace{\frac{(1-\mu) b_0 i}{b_0 i + b_1(K-i)}}_{\text{birth to } \mathscr{C}_0} \qquad \text{and} \tag{3.8}$$

$$q_i = \underbrace{\frac{d_0 i}{d_0 i + d_1(K-i)}}_{\text{death from } \mathscr{C}_0} \cdot \underbrace{\frac{\mu b_0 i + b_1(K-i)}{b_0 i + b_1(K-i)}}_{\text{transition/birth to } \mathscr{C}_1}, \qquad \text{so that} \tag{3.9}$$

$$\begin{aligned} 1 - p_i - q_i = {} & \underbrace{\frac{d_1(K-i)}{d_0 i + d_1(K-i)}}_{\text{death from } \mathscr{C}_1} \cdot \underbrace{\frac{\mu b_0 i + b_1(K-i)}{b_0 i + b_1(K-i)}}_{\text{transition/birth to } \mathscr{C}_1} \\ & + \underbrace{\frac{d_0 i}{d_0 i + d_1(K-i)}}_{\text{death from } \mathscr{C}_0} \cdot \underbrace{\frac{(1-\mu) b_0 i}{b_0 i + b_1(K-i)}}_{\text{birth to } \mathscr{C}_0}. \end{aligned} \tag{3.10}$$

Let $\pi_i(t)$ represent the probability that there are i mitochondria in $\mathscr{C}_0$ at time t. Equivalently, $\pi_i(t) = \Pr\big(M_0(t) = i\big)$, which implies that $1 - \pi_i(t) = \Pr\big(M_1(t) = K - i\big)$. We derive the master equation describing the change in the probability distribution for the number of undamaged mitochondria at time t to be

$$\begin{aligned} \frac{\mathrm{d}\pi_0}{\mathrm{d}t} &= \hat{q}_1 \pi_1 - \hat{p}_0 \pi_0, \\ \frac{\mathrm{d}\pi_i}{\mathrm{d}t} &= \hat{p}_{i-1} \pi_{i-1} - (\hat{q}_i + \hat{p}_i) \pi_i + \hat{q}_{i+1} \pi_{i+1}, \qquad 1 \leqslant i \leqslant K-1, \\ \frac{\mathrm{d}\pi_K}{\mathrm{d}t} &= \hat{p}_{K-1} \pi_{K-1} - \hat{q}_K \pi_K, \end{aligned} \tag{3.11}$$

where $\hat{p}_i = p_i \cdot [d_0 i + (K-i)]^{-1}$ and $\hat{q}_i = q_i \cdot [d_0 i + (K-i)]^{-1}$ for events occurring, on average, at the rate $d_0 i + (K-i)$. This has the stationary distribution $\pi_0^\infty = 1$ and $\pi_i^\infty = 0$ for $i \neq 0$, provided $q_K \neq 0$. Hence, the only existing absorbing state in the stochastic framework is $M_0 = 0$. This result is in contrast to stability condition (3.6) of the deterministic model (3.3), which includes a transcritical bifurcation.

3.1.2.1 Simulation

We implement a modified Gillespie algorithm (Appendix B) to simulate the mitochondrial populations in the present model. Because the first damage transition occurs with such low probability, there is an extended period of time over which very few changes occur, but beyond which the selective advantage of damaged mitochondria leads to rapid fixation (Figure 3.3(a)). Although it takes more than 500 years to initiate a substantial decline toward extinction, the process is complete within three years (Figure 3.3(b)). We now wish to quantify the timing of this process by determining the expected time to extinction of the undamaged population. We consider this quantity to be the "time to total mitochondrial damage".

3.1.2.2 Expected time to total mitochondrial damage

We reformulate the model as a modified version of the classical Gambler's Ruin problem to determine the expected extinction times. As before, let p_i and q_i denote the probabilities of net gain and loss of one undamaged mitochondrion, respectively. Let W_i be the probability that, beginning with $M_0 = i$, M_0 will equal K before it reaches zero. Necessarily, $W_K = \mu W_{K-1}$,

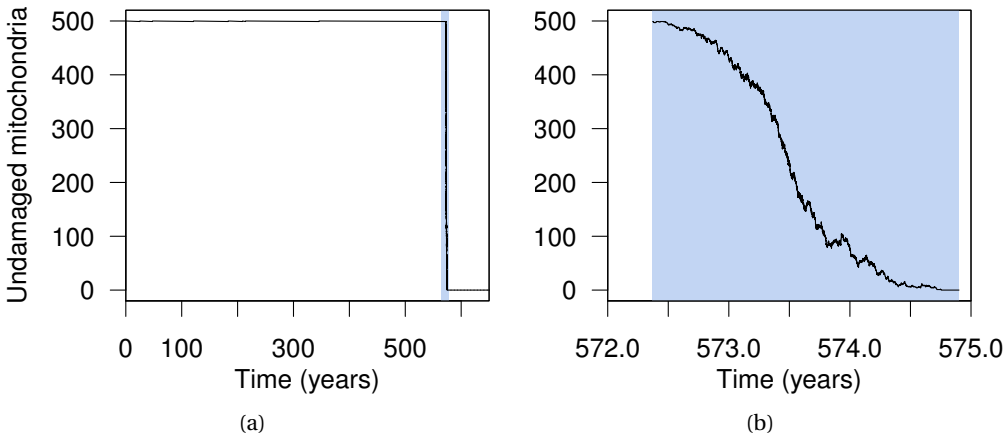

Figure 3.3. Representative trajectory for the number of undamaged mitochondria in the selection model (a) over several hundred years and (b) during the interval of rapid damage.

because a $\mathscr{C}_0$-to-$\mathscr{C}_1$ transition, occurring with probability μ, is the only way damage can be acquired in a completely healthy population of mitochondria. In the general case,

$$W_i = p_i W_{i+1} + q_i W_{i-1}. \tag{3.12}$$

Let L_i be the probability that all $\mathscr{C}_0$ mitochondria will be lost before reaching a size of K from $M_0 = i$. Using Equation (3.12), we obtain

$$L_i = (1 - p_i - q_i) + p_i L_{i+1} + q_i L_{i-1}. \tag{3.13}$$

Now, let T_i be the expected time until the undamaged population meets its ruin from a population of i mitochondria, and let E_i be the average duration of time between events. Because turnover events dictate the net changes in the mitochondrial population,

$$E_i = [d_0 i + d_1 (K - i)]^{-1}. \tag{3.14}$$

If M_0 remains unchanged, the new time to ruin is $T_i + E_i$. Similarly, the corresponding times for a gain or loss in $\mathscr{C}_0$ are $T_{i+1} + E_i$ and $T_{i-1} + E_i$, respectively. These lead to the second-order difference equation

$$q_i T_{i-1} - (p_i + q_i) T_i + p_i T_{i+1} = -E_i, \tag{3.15}$$

with $T_0 = 0$. Equation (3.15) can be solved explicitly (Appendix C) to give

$$\begin{cases} T_i = T_0 + \displaystyle\sum_{j=0}^{i-1} \left[\eta_{j+1} + \sum_{m=0}^{K-j-2} \prod_{n=m+1}^{K-j-1} \eta_{K-m} \rho_{K-n} \right], \quad i = 1, \ldots, K-1, \\ T_K = \eta_K + T_{K-1}, \end{cases} \tag{3.16}$$

where $\eta_i = E_i / q_i$, and $\rho_i = p_i / q_i$.

Figure 3.4 illustrates the mean extinction times for a variety of initial conditions. With K initially undamaged mitochondria, 602 years would pass, on average, before total damage occurs. which applies to the time course shown in Figure 3.3. In a normally functioning individual, this result suggests that although cellular health may decline over time, it does persist beyond the duration of a lifetime. In an individual with metabolic abnormalities, a change in one or more model parameters, such as μ, can reduce this time. A slight accumulation of damaged mitochondria greatly reduces the time to total damage, emphasizing that the mean extinction time is initially determined by slow transitions from $\mathscr{C}_0$ to $\mathscr{C}_1$.

To test the sensitivity of the total damage times to fractional growth reduction, s, and fractional scavenging reduction, c, we evaluate the closed form solution (3.16) over the ranges

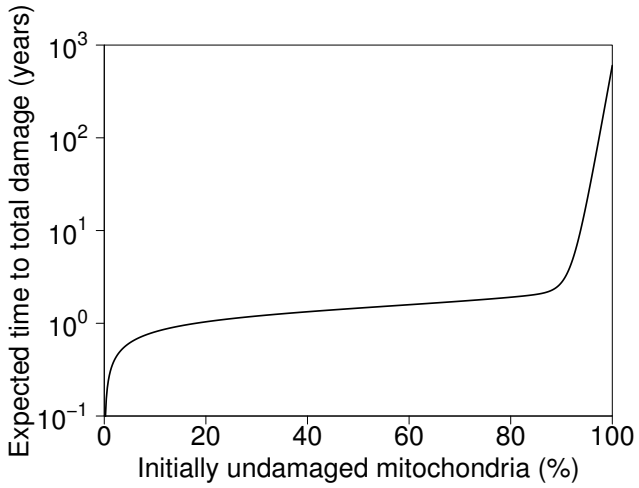

Figure 3.4. Analytical solution to the modified Gambler's Ruin problem for total damage times.

$0 \leqslant s \leqslant 0.2$ and $0 \leqslant c \leqslant 1$ (Figure 3.5). If damaged mitochondria lack sufficient evasion from scavenging mechanisms, reflected by $c \ll 1$, the short-term selective advantage lies with undamaged mitochondria and extinction times range from $T_i \sim \mathcal{O}(10^4)$ to $T_i > \mathcal{O}(10^{50})$. In general, if the deterministic stability criterion ($c > s$ for $\mu \ll 1$) is not satisfied for $\pi_1^* = 0$, the corresponding result in the stochastic model is an extremely large time to absorption.

3.1.2.3 Simulation and analysis comparison

We also use the extinction times from 2000 simulations to calculate the mean time to total damage, comparing the result to that determined by the modified Gambler's Ruin solution (Fig-

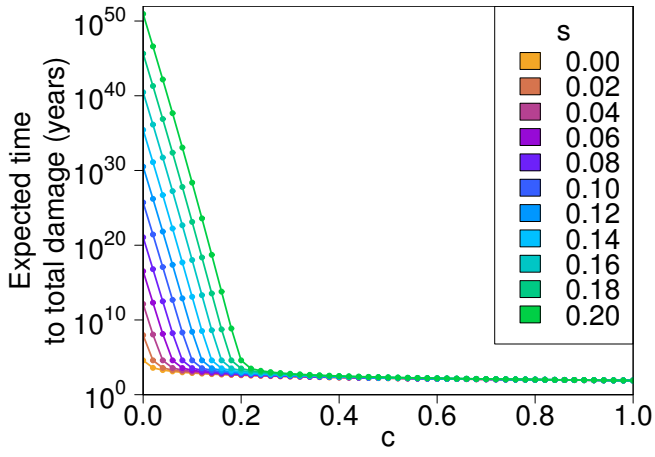

Figure 3.5. Various T_K from the stochastic mitochondrial selection model. Mean times to extinction are plotted against scavenging reduction parameter c. Each curve corresponds a particular growth reduction value s between 0 and 0.2.

ure 3.6). Theoretical calculations produce a good approximation to the computational results. There is a substantial difference between the mean and median extinction times for the upper 20% of undamaged mitochondria. This reflects significant variation in the damage acquisition process, which can be explained by an exponential distribution of extinction times when the initial population size is near maximal (Figure 3.7).

A small number of damaged mitochondria is equally as likely to undergo negative selection, which would fully restore the healthy population of organelles, as to put selective pressure on the undamaged subpopulation. Consequently, the survival advantage of $\mathscr{C}_1$ mitochondria matches the replicative advantage of those in $\mathscr{C}_0$ when $M_0 \gg M_1$. Although healthy mitochondria are more likely to grow, they are also more likely to die when their numbers are large. Thus, initially, when healthy organelles dominate, very few changes occur in the population. This adds considerable time to the extinction clock, but with a sudden shift in the balance, selection favors the damaged class, and extinction proceeds rapidly.

3.2 The role of feedback

The effects of mitochondrial selection are slow compared to the dynamics of metabolism. This, however, is only the case when feedback between these two entities is ignored. In this section, we explore bidirectional feedback between intracellular mitochondrial population dynamics and intramitochondrial superoxide production.

3.2.1 Superoxide-to-mitochondrial damage feedback

Mitochondrial dysfunction by way of ROS perpetuates its own decline, yet the impact on cellular function is not well defined. To address this, we create a feedback from our model of superoxide production to that of mitochondrial selection. Specifically, we redefine the transition rate of a mitochondrion from $\mathscr{C}_0$ into $\mathscr{C}_1$ to be

$$\mu(t) = \mu_0[1 + \rho(R_s(t)/R_{s0} - 1)]. \tag{3.17}$$

The transition probability μ is assumed to increase linearly with superoxide so that at the basal level ($R_s = R_{s0}$), a standard probability of μ_0 applies. The slope ρ is therefore the effective strength of elevated superoxide in accelerating damage transitions. We assess the time-dependent changes in extinction times (Equation (3.16)) by incorporating the dynamics of the superoxide production model. As in Section 2.2, we seek to determine the impact of nutrient intake marker ΔAUC on the present model. Figure 3.8 demonstrates reduced extinction times with both time and ΔAUC. A value of $\rho = 1$ is used for all curves. The true effect of nutrient

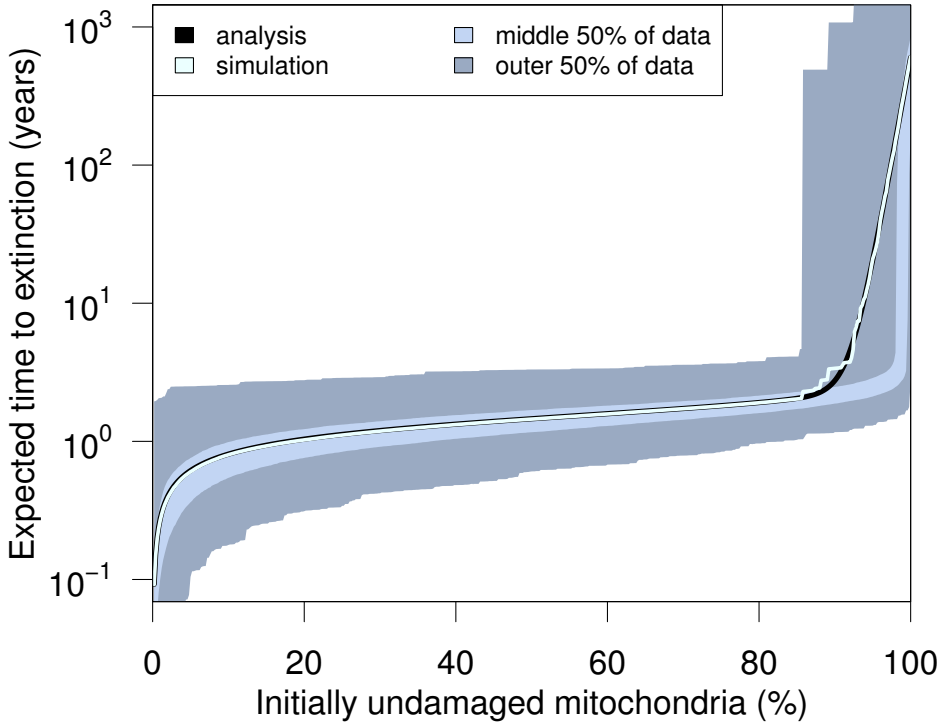

Figure 3.6. Simulation (white line) and analytical (black line) results for expected extinction times of undamaged mitochondria (2000 simulations). Darker gray regions correspond to the outer 50% of data, the lighter gray region to the middle 50% of data. 100% = 500 mitochondria.

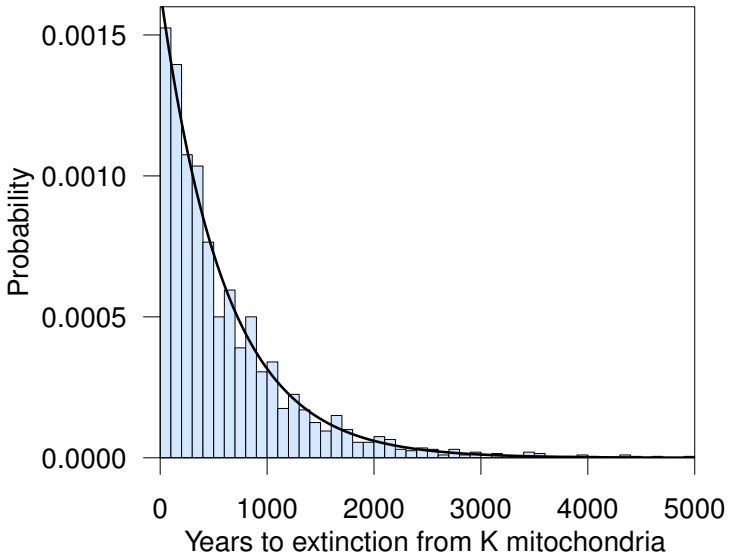

Figure 3.7. Simulated distribution of extinction times from an entirely undamaged initial population of K mitochondria. Results reveal an exponential distribution of times with rate $\lambda = 1/T_K$. $K = 500$.

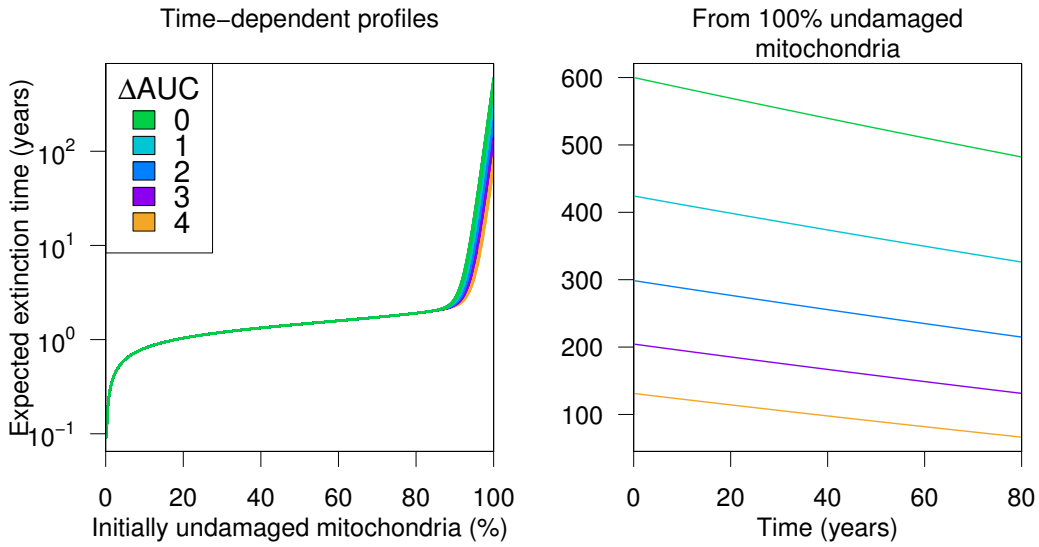

Figure 3.8. (a) Time-varying profiles of total damage times, given different levels of nutrient intake and a superoxide-dependent transition probability. (b) Extinction time trajectories for a fully undamaged mitochondrial population. Both graphs cover an 80-year period with $\rho = 1$.

overload is to accelerate the extinction of $\mathscr{C}_0$ mitochondria (Figure 3.8(a)). In an entirely undamaged population of mitochondria, the times to total damage decrease as elevated superoxide concentrations increase the transition probability from healthy to damaged (Figure 3.8(b)). Although the expected extinction times are longer for smaller values of ΔAUC, their reduction over time is faster because of their dependence on $1/\mu(t)$. This analysis requires the computation of extinction times from a given number of healthy mitochondria. In continuous time, however, damage and recovery occur non-discretely; this formulation does not independently allow for continuous changes in superoxide-influenced mitochondrial population dynamics.

3.2.2 Bidirectional feedback

We extend our consideration of unidirectional feedback to account for the increased production of superoxide by damaged mitochondria [50]. While selective differences are apparent, it should also be true that inherent abnormalities in a damaged mitochondrion progressively alter its function, further diminishing its capacity and efficiency for energy production and other respiratory processes. In turn, this would lead to increased superoxide production.

Let $D(t)$ be the probability that any given mitochondrion is classified as damaged, according to the stochastic model. Assume the effect of damage is to exacerbate mitochondrial inefficiency. We define

$$f(L,D) = (1-L)(1-D) \tag{3.18}$$

to be the new efficiency factor for mitochondria, thus replacing the term $(1-L)$ in Equation (2.4e):

$$\frac{\mathrm{d}C}{\mathrm{d}t} = v_2 N_e \cdot k_{gi} G_i (C_{tot} - C) - k_c[(1-q_r) f(L,D) + q_r]C, \tag{3.19}$$

Given that all mitochondria are assumed to develop inefficiency uniformly, we probabilistically account for heterogeneity at the population level. $f(L,D)$ therefore provides the link between intramitochondrial processes and intracellular population dynamics, describing the condition under which abnormalities within individual mitochondria are exacerbated by a damage status.

We are equipped with information about the likelihood of damage, which allows for the convenient treatment of intramitochondrial dynamics across multiple organelles, as well as the stochastic population dynamics, which integrate an all-or-nothing response to the damage of a single mitochondrion. The latter framework would require that we generate a total of K superoxide subsystems to determine total cellular ROS production, whereas the former is amenable to further changes in the model network. We therefore utilize the damage likelihood approach to implement mitochondrial feedback on superoxide.

To derive the form of $D(t)$, we return to a master equation formulation of mitochondrial damage and selection, in which we describe the evolution of the probability distribution for the number of mitochondria in damaged class $\mathscr{C}_1$. Let $\bar{\pi}_j(t) = \Pr(M_1(t) = j)$. Also, let $\bar{p}_j$ be the rate describing a net loss of one damaged mitochondrion and $\bar{q}_j$ that of net gain. Formulations of these expressions are similar to those previously used in (3.8) and (3.9), with the exception that each probability evolves relative to the mean time $[d_0(K-j) + d_1 j]^{-1}$ between events:

$$\bar{p}_j = d_1 j \cdot \frac{(1-\mu) b_0 (K-j)}{b_0(K-j) + b_1 j} \tag{3.20}$$

$$\bar{q}_j = d_0 (K-j) \cdot \frac{\mu b_0 (K-j) + b_1 j}{b_0(K-j) + b_1 j}. \tag{3.21}$$

We incorporate superoxide-mediated feedback by assuming that μ is given by the time-dependent expression $\mu_0[1 + \rho(R_{s0}/R_s - 1)]$. The corresponding master equation is

$$\begin{aligned}
\frac{\mathrm{d}\bar{\pi}_0}{\mathrm{d}t} &= \bar{p}_1 \bar{\pi}_1 - \bar{q}_0 \pi_0, \\
\frac{\mathrm{d}\bar{\pi}_i}{\mathrm{d}t} &= \bar{q}_{i-1}\bar{\pi}_{i-1} - (\bar{q}_i + \bar{p}_i)\bar{\pi}_i + \bar{p}_{i+1}\bar{\pi}_{i+1}, \qquad 1 \leqslant i \leqslant K-1, \\
\frac{\mathrm{d}\bar{\pi}_K}{\mathrm{d}t} &= \bar{q}_{K-1}\bar{\pi}_{K-1} - \bar{p}_K \bar{\pi}_K.
\end{aligned} \tag{3.22}$$

Let $D = \sum_{j=1}^{K} \bar{\pi}_j$. By definition, $D = 1 - \bar{\pi}_0$ and describes the probability of having at least one damaged mitochondrion in the population. Given the simplicity of master equation (3.22), we can solve this system with initial conditions $\bar{\pi}_0(0) = 1$ and $\bar{\pi}_j(0) = 0$ for $j \neq 0$. For ease of use, we numerically solve these $K+1$ differential equations in conjunction with the superoxide production model equations. Further, for constant μ, the dynamics of D do not change substantially when solving a reduced version of the master equation comprising $z+2$ equations for $z \geqslant 30$ (Equations (3.23), Figure 3.9).

$$\begin{aligned}
\frac{\mathrm{d}\bar{\pi}_0}{\mathrm{d}t} &= \bar{p}_1\bar{\pi}_1 - \bar{q}_0\pi_0, \\
\frac{\mathrm{d}\bar{\pi}_i}{\mathrm{d}t} &= \bar{q}_{i-1}\bar{\pi}_{i-1} - (\bar{q}_i + \bar{p}_i)\bar{\pi}_i + \bar{p}_{i+1}\bar{\pi}_{i+1}, \qquad 1 \leqslant i \leqslant z-1, \\
\frac{\mathrm{d}\bar{\pi}_z}{\mathrm{d}t} &= q_{z-1}\bar{\pi}_{z-1} - (\bar{q}_z + \bar{p}_z)\bar{\pi}_z \\
\frac{\mathrm{d}\bar{\pi}_K}{\mathrm{d}t} &= \bar{q}_z\bar{\pi}_z,
\end{aligned} \tag{3.23}$$

The results presented henceforth are generated from the coupled superoxide system and the truncated master equation (3.23). Because mitochondrial dynamics are progressive, we use the original slow system (2.5h) in our coupling, and evolve all variables on the slow timescale. Daily meals are then absorbed in a constant rate of nutrient intake σ. The solution curves in Figure 3.10 are trajectories for superoxide concentration and total mitochondrial dysfunction over 100 years. We define total dysfunction to be $1 - f(L, D)$, which specifies the contribution of both individual and population-wide effects to mitochondrial function.

As in the model without feedback, the present system reveals accelerated elevations in superoxide concentrations with increased ΔAUC. However, the level of nutrient excess required for marked superoxide overproduction are reduced significantly. In the original model (Figure 2.5), superoxide concentrations remain below 10^{-4} μM for the 120-year period with ΔAUC = 2.0. In Figure 3.11, on the other hand, this same value of ΔAUC forces superoxide to rise well above 10^{-4} μM within 60 years. In addition, the inclusion of $f(L, D)$ promotes an age-related increase in oxidative stress independently of nutrient overload. This is illustrated by the superoxide curve associated with ΔAUC = 0, which experiences a slow rise. Total mitochondrial dysfunction, as expected, progressively increases over time. Compared to the timing predicted by the mean times to total damage, the feedback between superoxide and mitochondrial damage accelerates the onset of catastrophe. Within the first two decades, there is a relatively equivalent increase in dysfunction, due to the slow dynamics of L and D. As the effect of growing superoxide takes hold, a separation develops, in which damage-mediated

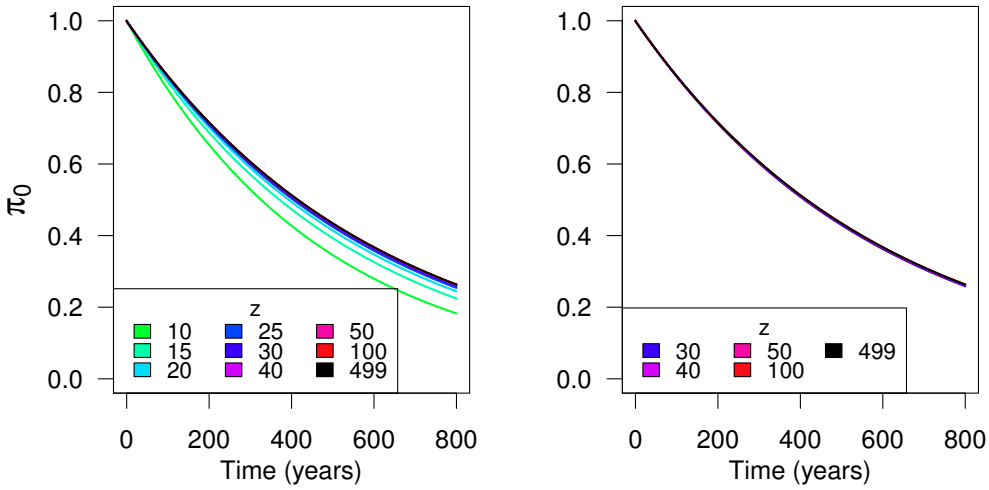

Figure 3.9. Comparison of truncated master equation π_0 trajectories. A total of $z+2$ equations are used for each numerical solution shown. Because the mitochondrial population is assumed to comprise $K = 500$ mitochondria, $z \leqslant 499$ must be true. Curves in the right panel are restricted to $z \geqslant 30$.

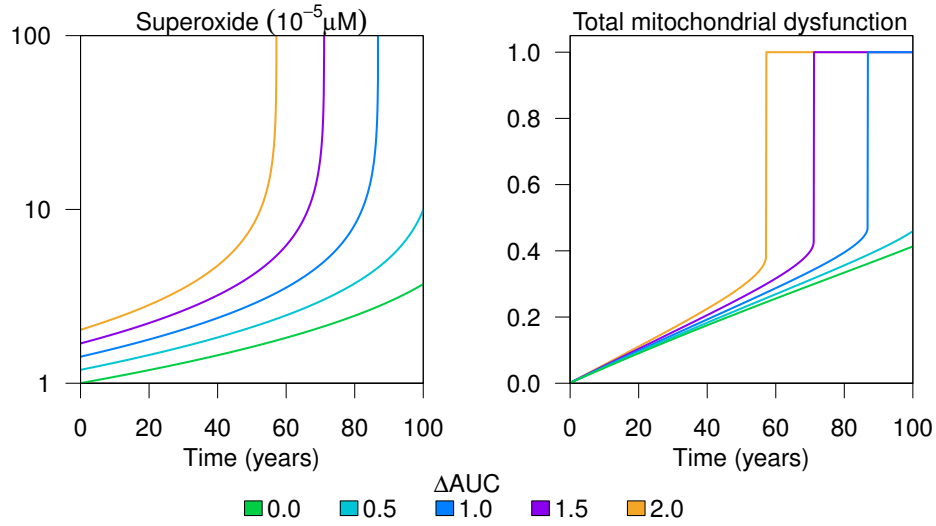

Figure 3.10. Dynamics of superoxide and mitochondrial dysfunction in the superoxide production model with damage-mediated feedback.

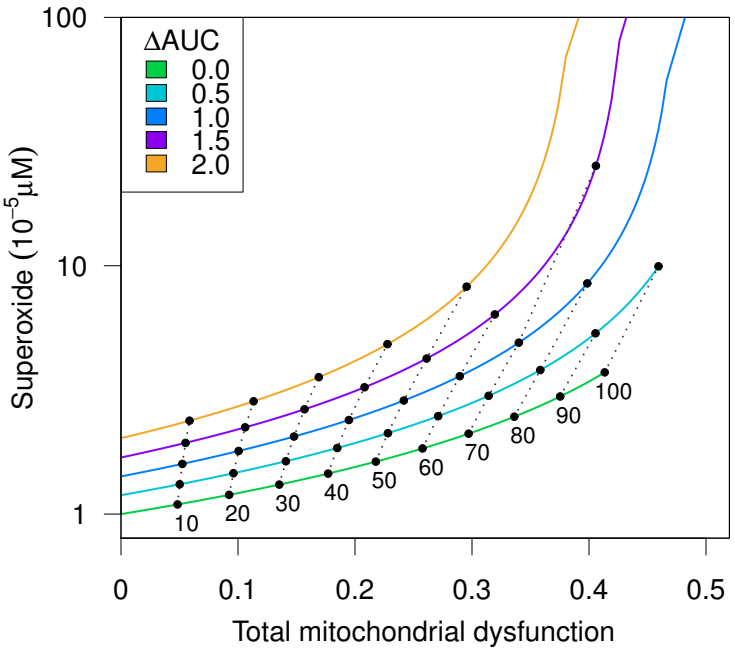

Figure 3.11. Mitochondrial dysfunction-superoxide phase plane summary of the model with feedback. Total mitochondrial dysfunction is determined by the function $1 - f(L,D)$. Filled, black circles indicate 10-year increments, and dotted lines track these time points across various ΔAUC.

feedback has a greater influence on ROS formation. In the end, it is unmitigated superoxide levels that result in total organelle dysfunction.

We explore how the timing of such dysfunction is affected by two important parameters: ξ, the rate at which mitochondrial inefficiency develops, and ρ, the effective strength of superoxide in damage acceleration. We choose these parameters because they are largely responsible for the slow feedback that ultimately leads to complete mitochondrial damage. Physiological levels of superoxide are between 10 and 200 pM [67]; as such, we construct age maps for superoxide concentrations exceeding an arbitrary threshold of 10^{-4} μM: ξ values span two orders of magnitude from $0.1 - 10 \times 10^{-6}$, ρ is varied within the closed interval $[0,1]$, and ΔAUC = 0, 0.5, 1.0, 1.5 and 2.0. The full system is solved numerically for a period of 100 years, and we record the year in which the threshold superoxide concentration is reached or exceeded (Figure 3.12).

For ΔAUC = 0, the threshold is surpassed within 100 years only when both ρ and ξ are near their maximum values. As ΔAUC increases, the age to reach threshold decreases, falling within a range of 30 – 40 years for more extreme values of ρ and ξ when ΔAUC = 2.0. These results suggest that while mitochondrial inefficiency can have a substantial impact on mi-

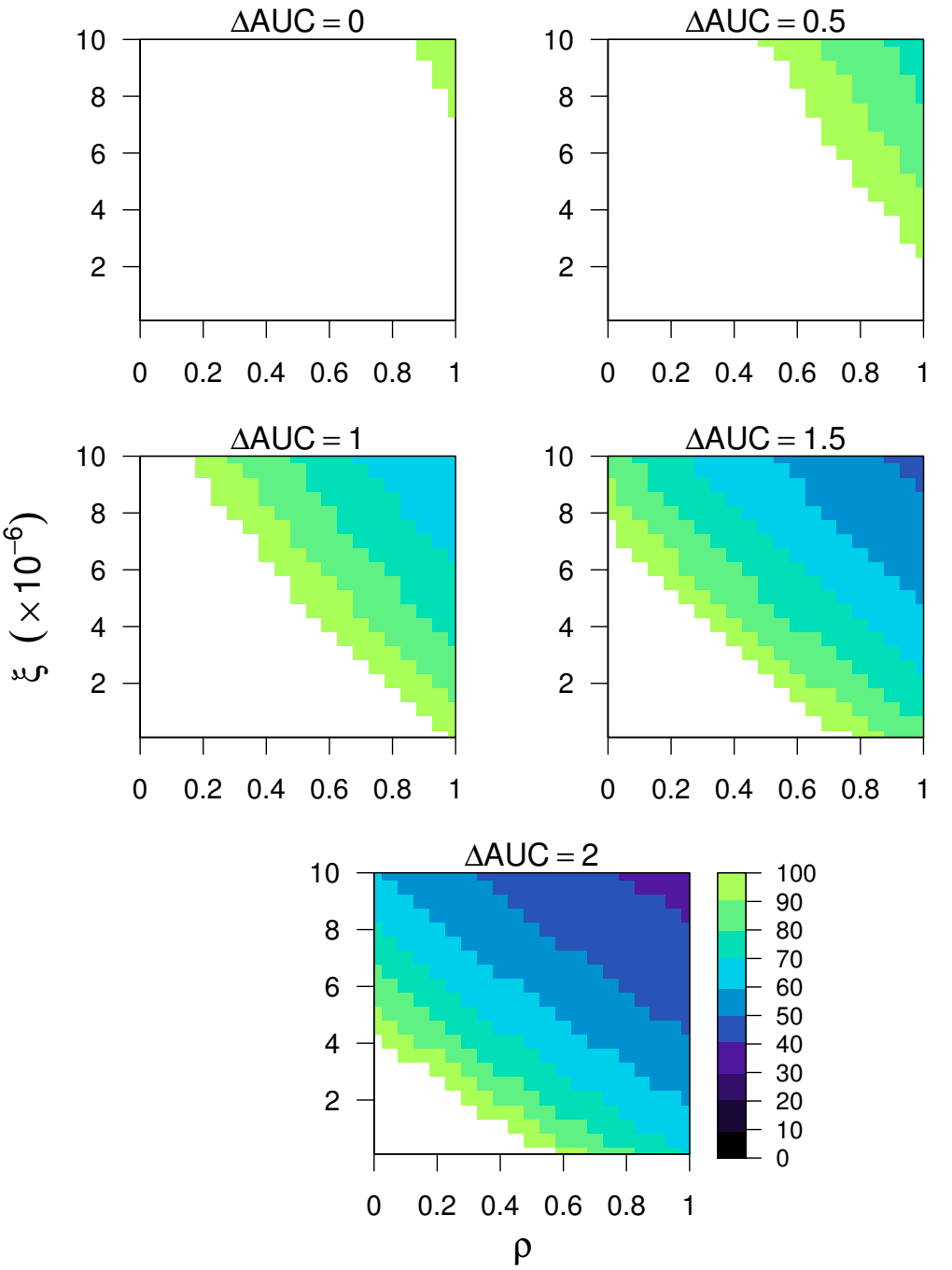

Figure 3.12. Age maps indicating the interaction of the rate of mitochondrial inefficiency development, ξ, and the strength of superoxide in increasing the mitochondrial transition probability, ρ.

tochondrial superoxide production, the worsening of such inefficiency due to mitochondrial damage drastically reduces the time until mitochondrial capacity is overtaken by excessive levels of superoxide.

3.3 Discussion

Our model of mitochondrial selection reveals important insights into mechanisms underlying the progression of cellular dysfunction. Under the assumption that mitochondria experience baseline dysfunction, along with our consideration of characteristic population-level differences arising from the damaged state, we determine that total mitochondrial damage is favored within the cellular environment and that such damage develops over several years. In the absence of distinct intracellular processes, these "years" refer to centuries; however, the accumulation of reactive oxygen species in cellular organelles and the bidirectional positive feedback between superoxide production and mitochondrial damage reduces this timeline to the order of decades. We find that increased glucose load leads to considerable reductions in the age to severe oxidative stress, as determined by threshold levels of mitochondrial superoxide.

In the full feedback model, we assume that superoxide affects the transition probability from healthy to damaged mitochondria in a linearly decreasing fashion. Although the mechanism underlying this assumption is biologically more detailed, our model would require additional variables that contribute unnecessary complexities. First, the progressive damage of mitochondria can be dictated largely by oxidative stress levels, but the dynamic process underlying such a transition requires considerations of superoxide effects on mitochondrial membrane potentials, along with the influx of water and other chemicals that can further alter mitochondrial function. Second, complications arising from a compromised mitochondrial membrane and other damage characteristics are necessarily linked to uniform mitochondrial dysfunction (L), as the propensity toward further mutations continues to worsen mitochondrial quality. Finally, mitochondrial fusion and fission events, more defined aspects of heteroplasmy, and the resultant effect on mitophagy require a dynamical network describing the interactions of individual entities and their characteristics. The mitochondrion is an entire biosystem on its own, but given the multiple biological scales that contribute to the development of insulin resistance, we eschew a systems biological approach in favor of identifying a few characteristic factors that provide qualitative similarities.

In this chapter, we have described the impact of glucose on insulin resistance, based on

the presence of oxidative stress and progressive mitochondrial dysfunction. Insulin resistance, however, is defined by impaired insulin signaling, which is absent from this model. The presence of oxidative stress, accompanied by mitochondrial dysfunction should lead to defects in the insulin signaling pathway, but we require a mechanistic basis for validation.

CHAPTER 4

THE PROGRESSION OF INSULIN RESISTANCE

Mitochondrial oxidative stress from nutrient overload is exacerbated by mitochondrial damage. Insulin resistance is a localized protective mechanism in the short term, but its long-term effects reach well beyond the individual cell, especially during the progression of type 2 diabetes. Insulin stimulates a series of phosphorylation events resulting in the activation or inhibition of kinases downstream of its receptor, ultimately facilitating the entry of glucose into target tissues. Insulin receptor substrates can be inhibited by stress-activated kinases, which are themselves activated by oxidative stress or pro-inflammatory signals [94]. This inhibition impairs the efficient propagation of the insulin signal and insulin-mediated glucose uptake. In this chapter, we determine how the underlying changes in mitochondrial health affect the progression of cellular insulin resistance through mathematical modeling (Figure 4.1).

The mechanisms explored in previous chapters for oxidative stress development and cellular dysfunction converge on the progression of insulin resistance through the insulin signaling pathway. Upon insulin binding to its receptor, the receptor tyrosine kinase becomes activated, leading to the immediate phosphorylation of insulin receptor substrate 1 (IRS-1) on tyrosine residues [20, 101]. This protein then associates with and subsequently activates the p85 regulatory subunit of phosphatidylinositol 3-kinase (PI3K). PI3K activation allows for the generation of phosphatidylinositol (3,4,5) trisphosphate, which leads to Akt/protein kinase B (PKB) activation. PKB is arguably a hub in insulin signaling, as it regulates a plethora of insulin-stimulated activities, including protein synthesis, glycogen synthesis for glucose storage, and cell survival [91]. The kinase also facilitates the translocation of glucose transporter 4 (GLUT4) to the cellular membrane via phosphorylation of Akt substrate 160, thus allowing for cellular glucose entry (Figure 4.2). The ability of skeletal muscle cells to remove glucose from the plasma therefore depends directly on the presence of GLUT4 at their surface, and insulin can increase the number of these when necessary [25, 55, 87, 91].

Hydrogen peroxide is a detoxified form of superoxide, but unlike superoxide, can leave the mitochondrion where it is produced and diffuse into the cytosol [67]. There, it activates stress

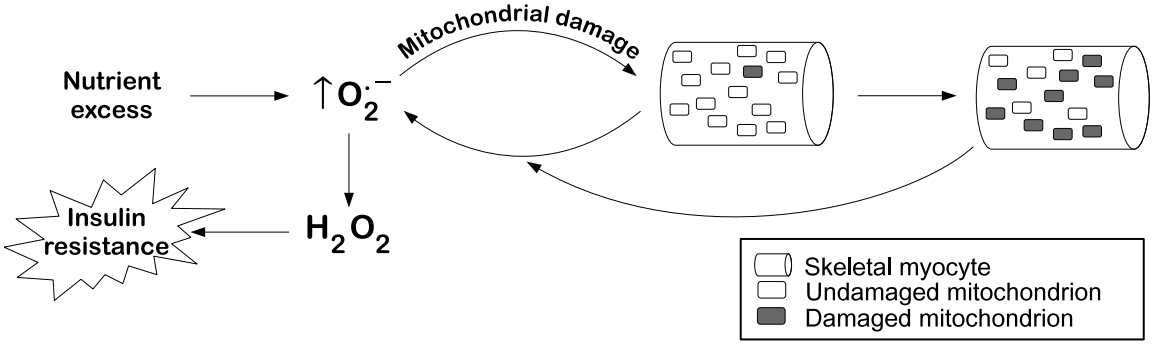

Figure 4.1. Illustration of the primary focus of Chapter 4. Feedback between superoxide production and mitochondrial damage, in the presence of nutrient excess, promotes elevated cytosolic hydrogen peroxide insulin resistance. $O_2^{\cdot -}$: superoxide; H_2O_2: hydrogen peroxide.

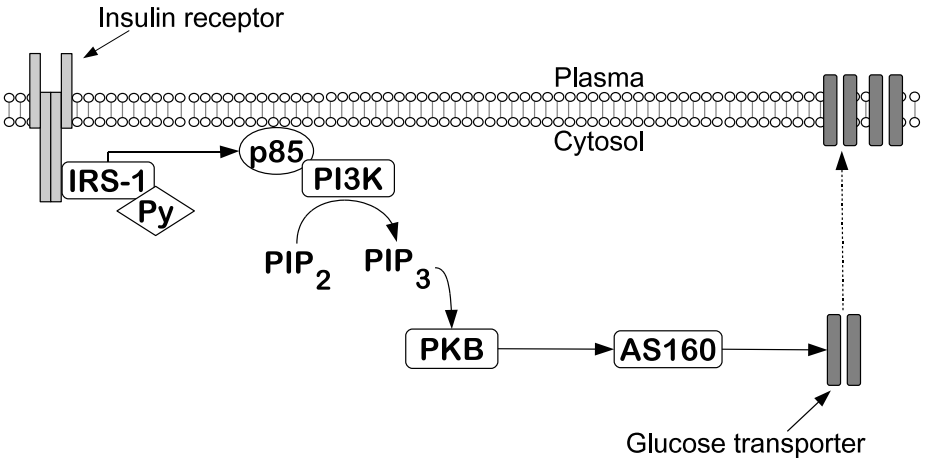

Figure 4.2. Insulin signaling overview. IRS-1 is tyrosine phosphorylated upon insulin binding to its receptor, leading to PI3K and PIP_3 activation. Downstream activation of PKB leads to GLUT4 exocytosis via protein AS160. IRS-1: insulin receptor substrate-1; Py: tyrosine phosphorylation; PI3K: phosphatidylinositol 3-kinase; PIP_2: phosphatidylinositol (4,5) bisphosphate; PIP_3: phosphatidylinositol (3,4,5) trisphosphate; PKB: Akt/protein kinase B.

protein c-Jun N-terminal kinase (JNK) in a dose-dependent manner [104]. One target of JNK is IRS-1, where it phosphorylates serine residues. Serine phosphorylation inhibits the tyrosine phosphorylation of IRS-1 that is required for proper post-receptor signaling [2,20]. Excess food intake and elevated insulin lead to increased glucose uptake and in turn to cellular oxidative stress. The resulting JNK activation impairs insulin signaling, with the effect of reducing both the amount of glucose entering the cell and oxidative stress. Accumulated reactive oxygen species in skeletal muscle cells therefore create a protective negative feedback loop [43].

4.1 Model of insulin signaling

We define a minimal model of insulin signaling that quantifies the effects of oxidative stress. Sedaghat et al. provide a detailed mechanistic model for insulin signaling that tracks the insulin signaling cascade, from surface receptors to several downstream kinases [85]. An input of insulin eventually results in the movement of intracellular GLUT4 to the cell membrane for glucose uptake. This model does not include the inhibitory function of serine-phosphorylated IRS-1.

Nyman et al. use *in vitro* data and current knowledge of metabolic regulation to develop a comprehensive systems biological model of glucose homeostasis with three major subsystems: whole-body, adipose tissue signaling, and insulin binding [71]. The purpose of the full model is to test hypotheses that provide a link between *in vitro* and *in vivo* experimentation, in order to ultimately explain observed differences in adipose tissue glucose uptake data. This model does include the inhibitory function of IRS-1 serine phosphorylation. However, the mechanism of this activity is different for adipocytes, wherein mammalian target of rapamycin (mTOR) is the major cause of serine phosphorylation. mTOR is a downstream target of PKB, and its effect in adipose tissue does not alter mitochondrial function [42].

We aim to elucidate the mechanisms contributing to the long-term progression of insulin resistance in skeletal muscle cells by developing a minimal version of the Sedaghat et al. model, in the same vein as the adipose tissue module of the Nyman et al. M^2 model. In our model, oxidative stress-activated proteins, influenced by intra-mitochondrial dynamics, are responsible for the negative feedback of IRS-1 serine phosphorylation on insulin signaling (Figure 4.3).

The full system (4.1) consists of 11 ordinary differential equations. The model's state variables are fractions of unbound and bound insulin receptors, $I_u(t)$ and $I_r(t)$; activity level of phosphorylated tyrosine residues within IRS-1, P_y; activity level of phosphorylated inhibitory serine residues within IRS-1, $P_s(t)$; unphosphorylated and phosphorylated JNK, $J_u(t)$ and $J(t)$;

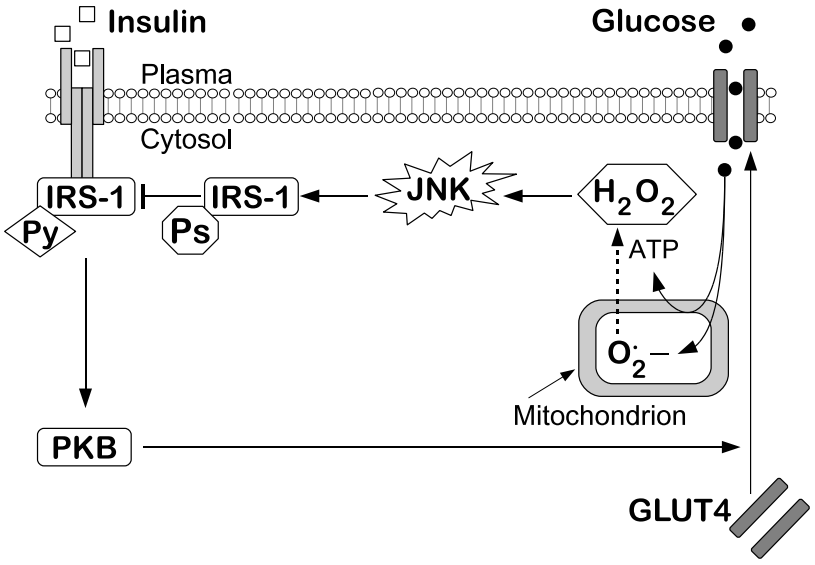

Figure 4.3. Insulin signaling pathway with reactive oxygen species effects. Insulin stimulates tyrosine phosphorylation of IRS-1, which leads to PKB activation and subsequent GLUT4 translocation to the cell membrane. Glucose enters the cell through these transporters, and its metabolism generates superoxide, which leads to the presence of hydrogen peroxide in the cytosolic space. Hydrogen peroxide activates JNK, which leads to IRS-1 serine phosphorylation. The phosphorylated serine residues prevent tyrosine phosphorylation, thus impeding the insulin signal. IRS-1: insulin receptor substrate-1; Py: tyrosine phosphorylation; Ps: serine phosphorylation; PKB: Akt/protein kinase B; JNK: c-Jun N-terminal kinase; H_2O_2: hydrogen peroxide; $O_2^{\cdot -}$: superoxide; GLUT4: glucose transporter 4.

unphosphorylated and phosphorylated PKB, $P_i(t)$ and $P(t)$; fractions of intracellular and membrane GLUT4, $U_i(t)$ and $U(t)$; and cytosolic hydrogen peroxide, $R_h(t)$.

$$\left.\begin{aligned} &\text{Unbound insulin receptors:} && \frac{\mathrm{d}I_u}{\mathrm{d}t} = -\alpha_i I_u I + \delta_i I_r \\ &\text{Bound insulin receptors:} && \frac{\mathrm{d}I_r}{\mathrm{d}t} = \alpha_i I_u I - \delta_i I_r \end{aligned}\right\} \tag{4.1a}$$

$$\text{Phosphorylated tyrosine residues:} \quad \frac{\mathrm{d}P_y}{\mathrm{d}t} = \alpha_y I_r (1-P_y)(1-P_s) - \delta_y P_y \tag{4.1b}$$

$$\text{Phosphorylated serine residues:} \quad \frac{\mathrm{d}P_s}{\mathrm{d}t} = \alpha_s (1-P_s) J - \delta_s P_s \tag{4.1c}$$

$$\left.\begin{aligned} &\text{Unphosphorylated JNK:} && \frac{\mathrm{d}J_u}{\mathrm{d}t} = -\alpha_j J_u R_h + \delta_j J \\ &\text{Phosphorylated JNK} && \frac{\mathrm{d}J}{\mathrm{d}t} = \alpha_j J_u R_h - \delta_j J \end{aligned}\right\} \tag{4.1d}$$

$$\left.\begin{aligned} &\text{Unphosphorylated PKB/Akt:} && \frac{\mathrm{d}P_i}{\mathrm{d}t} = -\alpha_p P_y P_i + \delta_p P \\ &\text{Phosphorylated PKB/Akt:} && \frac{\mathrm{d}P}{\mathrm{d}t} = \alpha_p P_y P_i - \delta_p P \end{aligned}\right\} \tag{4.1e}$$

$$\left.\begin{aligned} &\text{Intracellular GLUT4:} && \frac{\mathrm{d}U_i}{\mathrm{d}t} = -(\alpha_u + \eta_p P) U_i + \delta_u U \\ &\text{Membrane GLUT4:} && \frac{\mathrm{d}U}{\mathrm{d}t} = (\alpha_u + \eta_p P) U_i - \delta_u U \end{aligned}\right\} \tag{4.1f}$$

$$\text{Cytosolic hydrogen peroxide:} \quad \frac{\mathrm{d}R_h}{\mathrm{d}t} = q_h K \cdot \alpha_h(A_s, R_s) - \delta_{rh} A_h R_h \tag{4.1g}$$

With a detailed description of the model, we apply a number of simplifications to reduce the number of equations in (4.1) from 11 to 4.

- *Insulin receptors.* By applying conservation laws of time-scale arguments, we assume that insulin receptor activation is an immediate first step in the insulin signaling cascade (Equations (4.1a)). The rate at which insulin binds its receptor is governed by mass-action kinetics, with a linear unbinding term. No insulin is removed from the plasma during this process, and we assume that the level of insulin, I, remains constant. We assume that synthesis and degradation of insulin receptors are balanced, so that the total number of insulin receptors is constant. Thus, we can model the fraction of bound insulin receptors only as
$$\frac{\mathrm{d}I_r}{\mathrm{d}t} = \alpha_i (1-I_r) I - \delta_i I_r. \tag{4.2}$$

- *IRS-1 phosphorylation dynamics.* We assume that tyrosine phosphorylation in IRS-1 describes the activation level of IRS-1, while serine phosphorylation defines the level of inhibition of IRS-1. In both cases, a maximal activity level of 1.0 is assumed. Thus,

downstream insulin signaling occurs at a rate proportional to the level of tyrosine activity, modulated by serine inhibition (Equation (4.1b)). Because post-receptor activation of tyrosine IRS-1 is immediate, we take the proportion of bound insulin receptors to be in quasi-steady state, yielding the expression

$$I_r = \frac{\alpha_i I}{\alpha_i I + \delta_i} = \frac{I}{I + I_h}, \tag{4.3}$$

where $I_h = \delta_i / \alpha_i$. We consider I_r to be "insulin activity" and describe IRS-1 tyrosine activity with

$$\frac{\mathrm{d}P_y}{\mathrm{d}t} = \alpha_y \frac{I}{I + I_h}(1 - P_y)P_s^u - \delta_y P_y. \tag{4.4}$$

Inhibitory serine sites are phosphorylated at a rate linearly proportional to JNK activity, and serine deactivation occurs at constant rate δ_s (Equation (4.1c)).

- *JNK dynamics.* In Equations (4.1d), JNK activation via hydrogen peroxide is assumed to decay in the absence of its stimulus, while $J_{\max} = J_u + J$ is the constant maximal level of JNK activity. With $J_u = J_{\max} - J$, JNK signaling dynamics are given by

$$\frac{\mathrm{d}J}{\mathrm{d}t} = \alpha_j (J_{\max} - J)R_h - \delta_j J. \tag{4.5}$$

By assuming that the effect of hydrogen peroxide is seen immediately in the elevation of serine phosphorylation, JNK dynamics are in quasi-steady state. We therefore use the function

$$J = J_{\max} \frac{\alpha_j R_h}{\alpha_j R_h + \delta_j} = \frac{J_{\max} R_h}{R_h + \hat{j}}, \tag{4.6}$$

where $\hat{j} = \delta_j / \alpha_j$, as the response curve of JNK to hydrogen peroxide.

- *PKB/Akt dynamics.* The effect of upstream cascade components on PKB phosphorylation is assumed to be proportional to IRS-1 tyrosine phosphorylation (Equations (4.1e)). Under the assumption that $P_i + P = 1$, $P_i = 1 - P$, and we obtain

$$\frac{\mathrm{d}P}{\mathrm{d}t} = \alpha_p P_y (1 - P) - \delta_p P. \tag{4.7}$$

By further assuming an instantaneous effect of tyrosine phosphorylation on GLUT4 translocation, we describe changes in total PKB activity with

$$P = \frac{\alpha_p P_y}{\alpha_p P_y + \delta_p} = \frac{P_y}{P_y + \hat{p}}, \tag{4.8}$$

with $\hat{p} = \delta_p / \alpha_p$.

- *GLUT4 dynamics.* GLUT4 synthesis and degradation are assumed to balance, so that the total GLUT4 concentration, comprising both membrane and intracellular transporters, is constant. Hence, we denote the fraction of transporters in either location by U_i and U, so that $U_i + U = 1$. Transporters regularly cycle between intracellular and membrane states, while the function of PKB is to further stimulate the movement of GLUT4 toward the cellular membrane. We replace the equations in (4.1f) with

$$\frac{\mathrm{d}U}{\mathrm{d}t} = (\alpha_u + \eta_u P)(1-U) - \delta_u U. \tag{4.9}$$

- *Hydrogen peroxide dynamics.* A fraction q_h of superoxide-derived hydrogen peroxide diffuses from mitochondria into the cytosol (Equation (4.1g)). Because the superoxide concentration is assumed to be the same in all mitochondria, the total contribution to cytosolic hydrogen peroxide must be multiplied by the total mitochondrial population size, K. $\alpha_h(A_s, R_s)$ represents the MnSOD-dependent dismutation rate of superoxide, and catalase-mediated hydrogen peroxide removal is assumed to be the constant $\delta_{rh} A_h$.

4.1.1 Model reduction

Based on the above simplifications, we model the dynamics of insulin signaling and oxidative stress feedback with a reduced system (Equations (4.10), Table 4.1).

Phosphorylated tyrosine residues: $$\frac{\mathrm{d}P_y}{\mathrm{d}t} = \alpha_y \frac{I}{I + I_h}(1-P_y)(1-P_s) - \delta_y P_y \tag{4.10a}$$

Phosphorylated serine residues: $$\frac{\mathrm{d}P_s}{\mathrm{d}t} = \alpha_s (1-P_s)\frac{J_{\max} R_h}{R_h + \hat{j}} - \delta_s P_s \tag{4.10b}$$

Fraction membrane GLUT4: $$\frac{\mathrm{d}U}{\mathrm{d}t} = \left(\alpha_u + \eta_p \frac{P_y}{P_y + \hat{p}}\right)(1-U) - \delta_u U \tag{4.10c}$$

Cytosolic hydrogen peroxide: $$\frac{\mathrm{d}R_h}{\mathrm{d}t} = q_h K \cdot \alpha_h(A_s, R_s) - \delta_{rh} A_h R_h \tag{4.10d}$$

This system has two inputs: insulin and hydrogen peroxide. We assess the composite effects of these by first computing the steady-state percentage of membrane GLUT4. The equilibrium expressions of the four variables in the reduced system are

$$R_h = \frac{q_h K}{\delta_{rh} A_h}\alpha_h \tag{4.11}$$

$$P_s = \frac{\alpha_s J_{\max} R_h}{\alpha_s J_{\max} R_h + \delta_s (R_h + \hat{j})} \tag{4.12}$$

$$P_y = \frac{\alpha_y (1-P_s) I}{[\alpha_y (1-P_s) I_r + \delta_y](I + I_h)} \tag{4.13}$$

$$U = \frac{\alpha_u (P_y + \hat{p}) + \eta_p P_y}{(\alpha_u + \delta_u)(P_y + \hat{p}) + \eta_p P_y} \tag{4.14}$$

Table 4.1. Parameter descriptions for Equations (4.10). A summary of all values used appears in Table A.1.

Parameter	Description	Units
A_h	catalase	μM
α_s	serine phosphorylation	min^{-1}
α_u	basal GLUT4 translocation	min^{-1}
α_y	tyrosine phosphorylation	min^{-1}
δ_{rh}	hydrogen peroxide removal	$\mu\text{M}^{-1}\ \text{min}^{-1}$
δ_s	serine dephosphorylation	min^{-1}
δ_u	GLUT4 internalization	min^{-1}
δ_y	tyrosine dephosphorylation	min^{-1}
η_p	PKB-mediated GLUT4 translocation	min^{-1}
I_h	half-maximal insulin activity	pM
$\hat{j}$	half-maximal JNK activation	μM
$J_{\max}$	maximal JNK activity	#
K	total number of mitochondria	mitochondria
$\hat{p}$	half-maximal PKB activity	#
q_h	fractional cytosolic appearance of hydrogen peroxide	#

Combining Equations (4.11) – (4.14) yields a function $U(I,\alpha_h)$, for which we can create a contour plot (Figure 4.4). Insulin enhances the percentage of GLUT4 at the cell membrane, while hydrogen peroxide has the opposite effect. Elevated insulin partially reverses the inhibition that oxidative stress imposes on glucose uptake, but the effectiveness of such action varies. For lower hydrogen peroxide production rates, insulin compensates well, as determined by the net gain in GLUT4 over all insulin concentrations. For intermediate levels of production, this compensation reaches a maximum, which then declines toward near-basal effect sizes for higher production. These results suggest that sufficient β-cell compensation for insulin resistance can maintain normal glucose regulation, but that an inability of β cells to do this leads to an oxidative stress-mediated loss in glucose uptake capacity.

4.1.2 Summary

Our model of insulin signaling incorporates essential aspects of the insulin signaling pathway, along with inhibitory mechanisms that play a role in the progression of insulin resistance. Through equilibrium analysis, we have demonstrated a mechanism through which hydrogen peroxide originating from mitochondria reduces the ability of skeletal muscle cells to respond to insulin cues. We conclude that an elevation in superoxide production ultimately impedes post-receptor insulin signaling through the activation of intracellular stress signaling.

Of note are some biological factors that have been omitted from our model, such as obe-

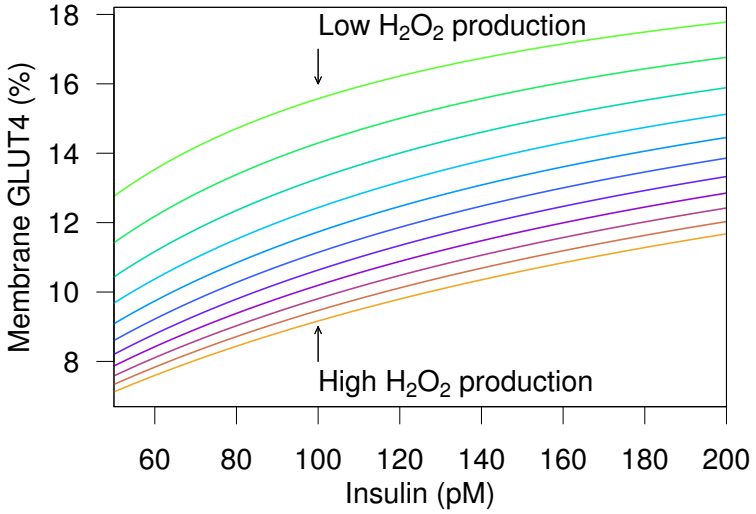

Figure 4.4. Steady-state percentages of membrane GLUT4 presence in response to insulin and hydrogen peroxide from the reduced insulin signaling model. The lowest H_2O_2 production rate shown is 0 per mitochondrion min^{-1}; the highest rate is 100.0 per mitochondrion min^{-1}.

sity. Insulin resistance and obesity occur together frequently in a clinical setting and reveal a role for inflammation in metabolic abnormalities [66]. In skeletal muscle tissue, along with adipose tissue, inflammatory signals, especially tumor necrosis factor α (TNFα), have been implicated in JNK activation [45]. The convergence of reactive oxygen species and inflammation on stress activation in skeletal muscle cells eliminates the need for an explicit description of diet-induced inflammation. A long-term state of obesity can be modeled by an external environmental parameter that increases JNK-mediated serine phosphorylation independently of hydrogen peroxide. Inclusion of an inflammatory factor would therefore work to further inhibit tyrosine phosphorylation and decrease membrane GLUT4.

Several components of the insulin signaling cascade have also been left out of the model, in contrast to the the work of Sedaghat et al. [85]; however, this omission reflects the goal of the present work. The activity of cellular reactive oxygen species interrupts normal insulin signaling, while insulin stimulates it. This framework allows us to incorporate additional time-dependent components that contribute to a mechanistic timeline of metabolic dysregulation, while limiting superfluous levels of complexity.

4.2 Model of insulin resistance

The story of insulin resistance begins in the plasma, migrates to the mitochondrion and continues into the cytosol, where the insulin signaling pathway lies. In this section, we com-

bine the models of superoxide production and insulin signaling from Chapter 2, the damage feedback model described in Chapter 3, and the reduced model of insulin signaling outlined in Section 4.1. The combined model studies the role of mitochondria and nutrient excess in the progression of insulin resistance.

To explicitly model insulin signaling as the primary mechanism of insulin-stimulated glucose uptake, we must also modify the original glucose-insulin subsystem (2.1). Under the assumption that insulin-mediated glucose uptake is proportional to the fraction of GLUT4 (U) at the plasma membrane in skeletal muscle cells, we obtain the revised subsystem in Equations (4.15a) – (4.15c). The primary difference is that in Equation (4.15a), total glucose uptake is given by $\hat{s}GU$, which contrasts the earlier representation in Equation (2.1b) of SGI. With mitochondrial and reactive oxygen species dynamics, Equations (4.15d) – (4.15n) complete the system.

We augment superoxide dynamics with spontaneous dismutation, given by the term $\delta_{rs}R_s^2$ (Equation (4.15e)). MnSOD function is extremely effective, and the rate of dismutation via this antioxidant is several orders of magnitude faster than that brought on by the collision of two superoxide anions [34]. Thus, spontaneous dismutation becomes significant in governing hydrogen peroxide dynamics only upon MnSOD depletion. Once $A_s = 0$, superoxide and hydrogen peroxide approach their respective equilibrium concentrations, which are identical for all ΔAUC, and the difference between health and dysfunction is determined by the times at which these equilibria are approached, as is the case in the previous formulation.

We initialize the system by assuming that glucose is in equilibrium according to the given value of food intake parameter σ, which is held constant for the duration of the simulated time courses. We then solve for $\hat{s}$ in

$$\frac{\mathrm{d}G}{\mathrm{d}t} = \sigma + h_g - k_g G - \hat{s}GU$$

according to the initial steady-state assumption, so that $\hat{s} = (\sigma + h_g - k_g G_0)/(G_0 U_0)$. $\hat{s}$ is an adapted rate of uptake into skeletal muscle cells determined by exogenous glucose input. In each case, $G(0) = 5$ mM. Trajectories for plasma glucose and insulin, hydrogen peroxide, both IRS-1 phosphorylation states, and membrane GLUT4 are presented for several values of ΔAUC between 0 and 4.0 with $\rho = 0.5$ (Figure 4.5).

ΔAUC > 0 leads to elevated glucose uptake rates from plasma into the cell. As a result, glucose, insulin, and serine phosphorylation activity experience larger rates of increase, overcoming the fact that each of these variables has the same initial condition for every ΔAUC value. As time progresses, elevated glucose input is associated with more rapid declines in mi-

Plasma glucose: $$\frac{\mathrm{d}G}{\mathrm{d}t} = \sigma + h_g - k_g G - \hat{s}GU \tag{4.15a}$$

Plasma insulin: $$\frac{\mathrm{d}I}{\mathrm{d}t} = h_i B \frac{G^4}{G^4 + G_h^4} - k_i I \tag{4.15b}$$

Intracellular glucose: $$\frac{\mathrm{d}G_i}{\mathrm{d}t} = v_1 \cdot \hat{s}GU - k_{gi} G_i. \tag{4.15c}$$

Reduced ETC complex: $$\frac{\mathrm{d}C}{\mathrm{d}t} = v_2 N_e \cdot k_{gi} G_i (C_{tot} - C) - k_c[(1 - q_r) f(L, D) + q_r]C, \tag{4.15d}$$

$$\text{with } f(L, D) = (1 - L)(1 - D)$$

Superoxide: $$\frac{\mathrm{d}R_s}{\mathrm{d}t} = k_c q_r C - k_{rs} R_s A_s - \delta_{rs} R_s^2 \tag{4.15e}$$

MnSOD: $$\frac{\mathrm{d}A_s}{\mathrm{d}t} = a_a E - q_a k_{rs} R_s A_s \tag{4.15f}$$

MnSOD translation signal: $$\frac{\mathrm{d}E}{\mathrm{d}t} = a_e R_s (1 - E) - k_e E \tag{4.15g}$$

Mitochondrial inefficiency: $$\frac{\mathrm{d}L}{\mathrm{d}t} = \xi \left(1 - \frac{R_{s0}}{R_s}\right)(1 - L) \tag{4.15h}$$

Mitochondrial damage probability: $$\frac{\mathrm{d}D}{\mathrm{d}t} = \sum_{j=1}^{K} \frac{\mathrm{d}\bar{\pi}_j}{\mathrm{d}t} \tag{4.15i}$$

Probability of i damaged mitochondria: $$\frac{\mathrm{d}\bar{\pi}_i}{\mathrm{d}t} = \bar{q}_{i-1}\bar{\pi}_{i-1} - (\bar{q}_i + \bar{p}_i)\bar{\pi}_i + \bar{p}_{i+1}\bar{\pi}_{i+1}, \tag{4.15j}$$

$$\text{with } \bar{p}_j = d_1 j \cdot \frac{(1 - \mu(t)) b_0 (K - j)}{b_0(K - j) + b_1 j},$$

$$\bar{q}_j = d_0 (K - j) \cdot \frac{\mu(t) b_0 (K - j) + b_1 j}{b_0(K - j) + b_1 j}, \text{ and}$$

$$\mu_0 \left[1 + \rho \left(\frac{R_{s0}}{R_s} - 1\right)\right]$$

Phosphorylated tyrosine residues: $$\frac{\mathrm{d}P_y}{\mathrm{d}t} = \alpha_y \frac{I}{I + I_h}(1 - p_y)(1 - P_s) - \delta_y P_y \tag{4.15k}$$

Phosphorylated serine residues: $$\frac{\mathrm{d}P_s}{\mathrm{d}t} = \alpha_s (1 - P_s) \frac{J_{\max} R_h}{R_h + \hat{j}} - \delta_s P_s \tag{4.15l}$$

Fraction membrane GLUT4: $$\frac{\mathrm{d}U}{\mathrm{d}t} = \left(\alpha_u + \eta_p \frac{P_y}{P_y + \hat{p}}\right)(1 - U) - \delta_u U \tag{4.15m}$$

Cytosolic hydrogen peroxide: $$\frac{\mathrm{d}R_h}{\mathrm{d}t} = q_h K \cdot \alpha_h (A_s, R_s) - \delta_{rh} A_h R_h \tag{4.15n}$$

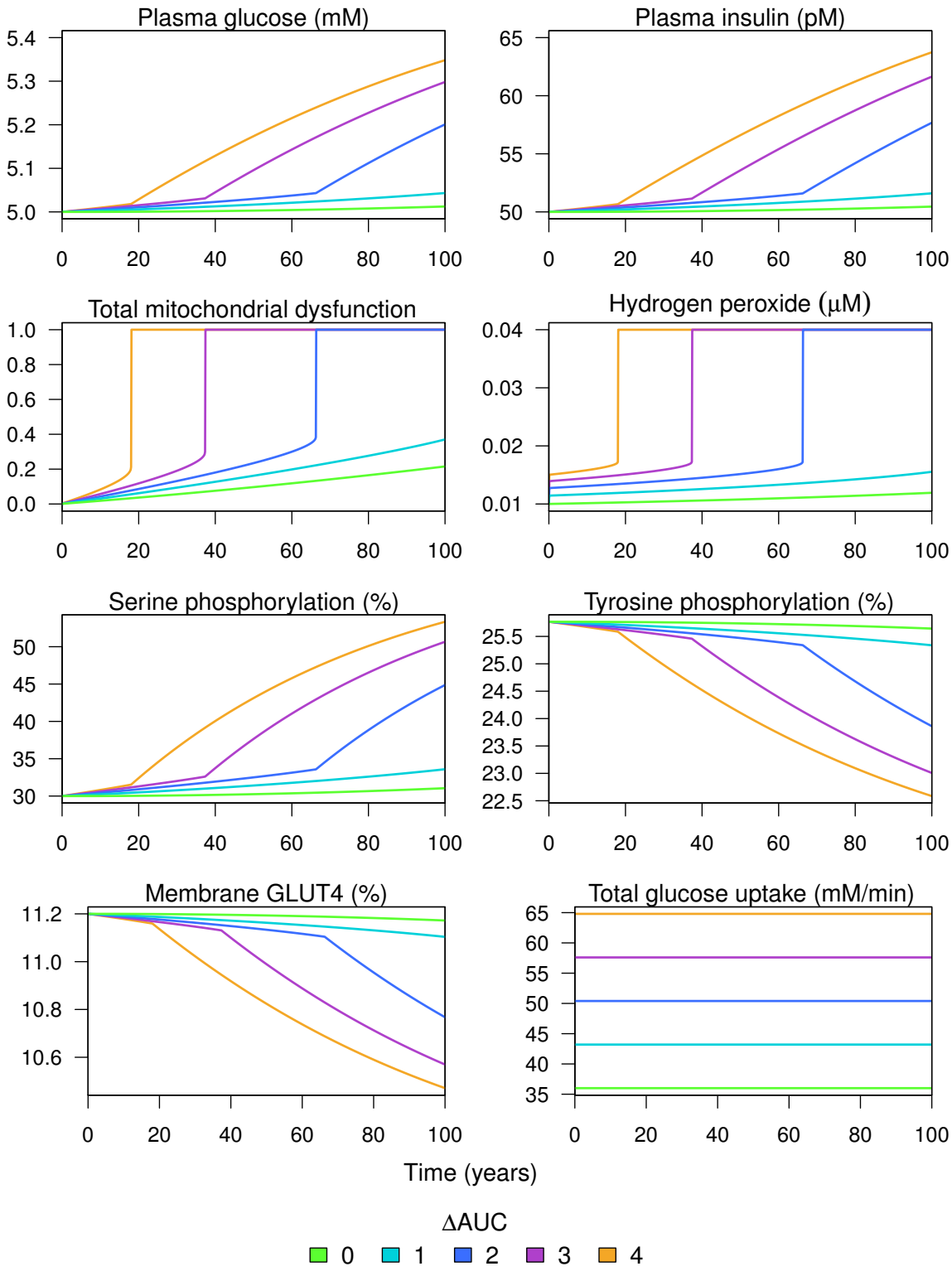

Figure 4.5. Trajectories from the superoxide production model with insulin signaling and mitochondrial damage feedback. $\rho = 0.5$.

tochondrial function, and increases in hydrogen peroxide and serine phosphorylation of IRS-1 are met with decreases in tyrosine phosphorylation and membrane GLUT4. Upon maximal mitochondrial dysfunction (a value of 1.0), a shift in the cytosolic variables is seen. Glucose, insulin, and IRS-1 serine phosphorylation increase at even greater rates; hydrogen peroxide reaches its maximal steady-state concentration; and, the percentage of GLUT4 at the cellular membrane experiences a sharper decline. Nutrient excess facilitates a more dramatic change in these variables and greatly reduces the timing of major dysfunction.

For ΔAUC = 0, worsening mitochondrial function, due to either age-related or damage-mediated inefficiency, is the major cause of the slight decline in metabolic function. For ΔAUC > 0, elevated concentrations of glucose result in higher insulin levels, which allow for a proportional rise in uptake via increased tyrosine phosphorylation, more hydrogen peroxide and subsequent metabolic abnormalities. In all cases, the total rate at which glucose is taken into skeletal muscle cells remains constant.

Complete mitochondrial dysfunction initiates a break point in the system, beyond which model dynamics experience more rapid changes. This behavior is in line with the longitudinal data analysis by Tabák et al., in which type 2 diabetics exhibit an elevated rate of decline in insulin sensitivity shortly before disease diagnosis [90]. By extending the time interval of our numerical solutions, we can determine the timing of the break point in model dynamics for a range of ΔAUC (Figure 4.6). The timing of these sharp changes in metabolic activity are inversely proportional to ΔAUC. Oxidative stress, combined with nutrient excess, therefore plays a significant role in the decline of skeletal muscle function over time. Yet, even in the absence of glucose overload, total mitochondrial damage occurs within fewer than 200 years, which is a substantial reduction from the 602-year estimate from the original mitochondrial

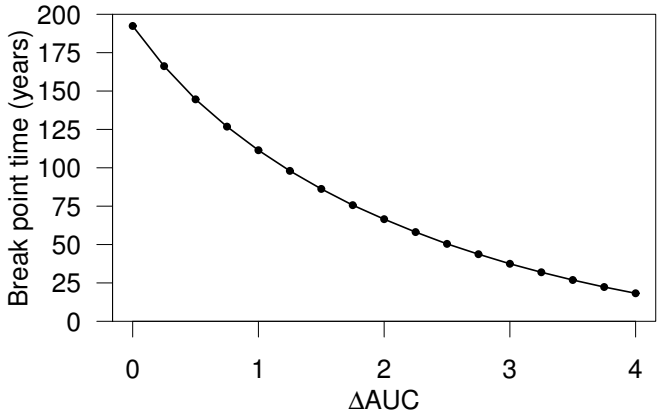

Figure 4.6. Timing of the transition to total mitochondrial damage over a range of ΔAUC.

selection model (Chapter 3). This suggests that an unavoidable accumulation of ROS and progressive alterations to mitochondrial health, however slight, are important in metabolic regulation.

4.3 Discussion

We have developed a minimal model of insulin signaling subject to ROS-induced modification. Environmental changes that increase mitochondrial superoxide production also increase cytosolic hydrogen peroxide. The result is oxidative stress-mediated activation of JNK, which impairs proper insulin signaling through inhibitory phosphorylation of the insulin receptor substrate.

Insulin signaling experiences some level of impairment through the course of the average lifetime. The free radical theory of aging asserts that this change is due to the development oxidative stress with age [98]. The results of the present model are consistent with this notion, as the GLUT4 trajectory for ΔAUC = 0 demonstrates an age-related decline that occurs independently of environmental factors. Inherent changes in mitochondrial health promote superoxide production, and as the likelihood of cellular mitochondrial dysfunction increases, so too does the likelihood of oxidative stress. Hydrogen peroxide derived from the decline in mitochondrial health leads to small stress responses that enhance serine phosphorylation of IRS-1, thus reducing GLUT4 at the plasma membrane. Hence, external factors, such as excess diet-derived glucose, exacerbate age-related insulin resistance through oxidative stress-mediated mitochondrial damage and impaired insulin signaling.

Initially, plasma glucose levels rise because of the slow decline in membrane GLUT4. Glucose-stimulated insulin secretion is sufficient to maintain constant levels of glucose uptake given a reduction of transporters at the cell surface (Figure 4.5). However, the initial rise in glucose due to ΔAUC input is not properly regulated by the current system. This is because the current system does not mount a compensatory response to glucose concentrations above "normal" steady-state levels. The existing compensation is the result of the standard insulin secretory response based on β-cell glucose sensing, which has a half-maximal stimulatory concentration (G_h) of 9.0 mM. The largest concentrations reached in the current model barely exceed 5.3 mM, so that insulin increases approximately linearly with glucose for the 100-year period of interest. Were sufficient compensatory β-cell function a factor in this model, the elevations in insulin would be more substantial. Therefore, the progression of a noticeably defective response to insulin requires not only the existence of inherent or environmentally-

influenced metabolic abnormalities, but also mechanisms that can improve the situation in the short term, but cause more harm than good in the long term. This is the role of β cells in the progression of insulin resistance and in the development of type 2 diabetes, which also explains why insulin resistance alone does not cause diabetes [7, 66].

CHAPTER 5

β-CELL FUNCTION AND DECOMPENSATION

β cells are solely responsible for the prevention of hyperglycemia. Dysfunction in peripheral tissues cannot lead to type 2 diabetes in the absence of β-cell abnormalities. Mechanisms of β-cell failure, as in the progression of insulin resistance, are incompletely understood. Well-defined, however, are the factors affected by such failure. β-cell activity encompasses three major components: β-cell mass, insulin secretion and insulin biosynthesis. Each of these has the capacity to adapt to changing metabolic demands, and a β-cell population that is unable to meet the requirements is considered dysfunctional. Sufficient loss of function results in the relative insulin deficiency that precipitates type 2 diabetes [66, 81].

To elucidate the mechanisms underlying β-cell failure, it is important to identify which components contribute the most dysfunction. Substantial reductions in β-cell mass have been associated with type 2 diabetes; specifically, the rates of apoptosis in these cells are increased [40,66,100]. However, only pancreatectomies resulting in the removal of more than 80% of normal β-cell mass result in insulin deficiency [26]. Further, it is unclear whether type 2 diabetics exhibit significant β-cell loss at the time of diagnosis [22, 63]. Together, these findings suggest that defective insulin synthesis and secretion contribute primarily to the onset of β-cell failure, while β-cell loss is a secondary defect.

Glucose-sensing in β cells is the primary signal for insulin secretion and occurs in two phases. The first phase is completed within 10 minutes of intravenous glucose stimulation [25], whereas the second may last for hours [48, 66]. Upon glucose entry into the β-cell, glucose phosphorylation, the first step in the glycolytic pathway, determines the rate at which glycolysis proceeds [46, 70, 72]. Glycolytic pyruvate increases the cytosolic ATP/ADP ratio through oxidative phosphorylation, precipitating the closure of ATP-dependent potassium channels (K_{ATP}). Cell depolarization and activation of voltage-gated calcium channels follow, thereby increasing the concentration of intracellular calcium. This rise in calcium promotes insulin exocytosis from secretory granules at the β-cell surface and thus a rise in circulating insulin [39, 86]. Glucose-stimulated K_{ATP}-dependent exocytosis characterizes the first phase of insulin secretion

[101]. A K_{ATP}-independent pathway amplifies the initial secretory and biosynthetic response, thus characterizing the second phase of insulin release, in which the exocytosis of existing hormone stores and the production of new insulin occurs. About half of all pyruvate generated by glycolysis enters this alternate pathway of cycling, from which amplifying signals, such as NADPH and α-ketoglutarate, are generated [46, 66]. These additional metabolites allow for constitutive glucose regulation.

Whereas the mitochondrion is largely responsible for immediate insulin release, the endoplasmic reticulum (ER) of β cells is a hub for proper insulin processing that leads to storage and exocytosis. Preproinsulin, the downstream product of insulin gene transcription, migrates to the ER membrane from the cytoplasm, and cleavage of its translocation signaling peptide accompanies its entry into the ER lumen. Upon entry, the immediate insulin precursor, proinsulin, is generated in its unfolded form. The ER folding machinery is responsible for processing nascent proinsulin in preparation for transit to the Golgi apparatus and subsequent packaging via granule synthesis [57]. Insulin release from the endocrine pancreas therefore relies on the interplay of several processes, whose proper function is necessary to prevent insulin insufficiency and glucose dysregulation.

ER stress results from an increased need for insulin and can impair β-cell function. It is characterized by an imbalance between the ER folding load and folding capacity [7]. High insulin demand increases the ER proinsulin processing workload and the likelihood of improper folding. Under these circumstances, the influx of unfolded proteins can overwhelm the ER folding mechanism, while an accumulation of unfolded or misfolded proteins triggers the unfolded protein response (UPR) of the cell. This response serves several important functions: It increases the folding capacity through ER-assisted folding (ERAF); it increases the degradation of misfolded and unfolded proteins through ER-associated degradation (ERAD); it reduces general protein translation in the cell; and, it upregulates transcription of its own genes [62, 103].

There are three primary effectors of the UPR: protein kinase RNA-like endoplasmic reticulum kinase (PERK), inositol-requiring protein 1α (IRE1α), and activating transcription factor 6 (ATF6) (Figure 5.1). Each of these is inhibited when bound to the ER chaperone immunoglobulin binding protein (BiP) [7, 33]. In the presence of ER stress, unfolded proteins sequester BiP, which allows for UPR effector activation. PERK attenuates protein translation by phosphorylating the α subunit of eukaryotic initiation factor 2; IRE1α and ATF6 phosphorylate and activate X-box binding protein 1 (XBP1) mRNA, which leads to increased transcription of UPR genes,

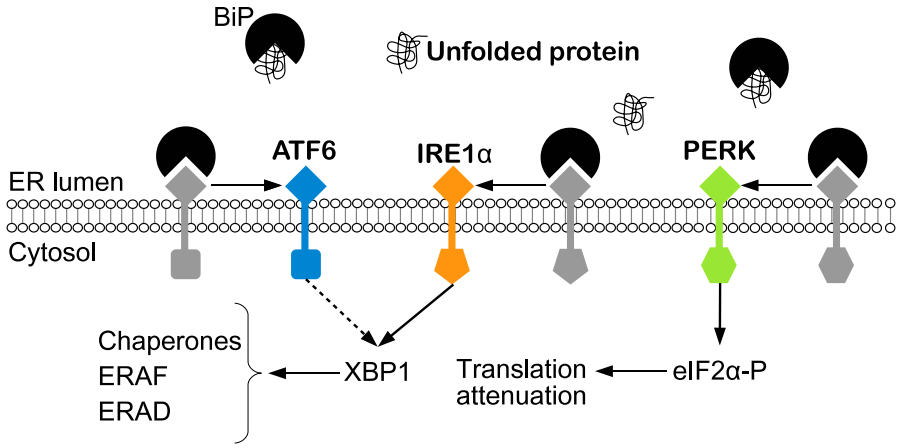

Figure 5.1. Unfolded protein response in an ER stress setting. In the absence of ER stress, BiP inhibits UPR effectors ATF6, IRE1α, and PERK through binding. An accumulation of unfolded proteins in the ER lumen sequesters BiP, allowing for UPR activation. In this case, PERK initiates eIF2α phosphorylation, which promotes attenuation of protein translation within the cell, thus reducing the workload sent to the ER. ATF6 and IRE1α both promote the production of ER chaperones and genes for ERAF and ERAD. The dotted line indicates that XBP1 is one target of ATF6, which can also undergo cleavage that results in similar ER stress-related responses as XBP1. ATF6, activating transcription factor 6; BiP, immunoglobulin binding protein; eIF2α-P, phosphorylated α subunit of eukaryotic initiation factor 2; ERAD, ER-associated degradation; ERAF, ER-assisted folding; IRE1α, inositol-requiring protein 1α; PERK, PKR-like endoplasmic reticulum kinase; XBP1, X-box binding protein 1.

BiP, and other essential ER chaperones [41, 97, 103].

Various chaperones mediate ERAF and ERAD activity, while also inhibiting the UPR. To enhance ERAF and ERAD responses, the UPR effectively upregulates production of the chaperones, creating a negative feedback loop that allows the system to reset once the stress has been eliminated [54, 97]. In a constitutively stressed ER, UPR activity can cause a progressive decline in insulin output through attenuated protein, and hence proinsulin, translation, which may contribute to the relative insulin deficiency accompanying type 2 diabetes onset. Further, when the severity of ER stress creates a permanent imbalance between workload and processing, prolonged UPR activation can initiate proapoptotic pathways, resulting in β-cell death [5, 56, 66].

In this chapter, we present a mathematical model for β-cell function and explore mechanisms of dysfunction through the UPR and β-cell compensatory mechanisms. Section 5.1 contains a model of the UPR and insulin production with constant β-cell mass, which we use to assess the effects of glucose on short-term UPR induction. In Section 5.2, we incorporate β-cell mass dynamics in a larger framework of glucose regulation to determine the long-term

implications of nutrient excess and insulin resistance.

5.1 Model of β-cell function

Following the framework of Trusina et al. [97], we construct a mathematical model of intracellular β-cell function based on unfolded proteins. The purpose of the original model is to determine the impact of UPR-mediated protein translation attenuation in relieving ER stress, as determined by increased production of unfolded proteins. Also explored is the relative benefit of reduced translation to the cell as a function of the duration of externally applied pulsatile stress. We adapt this model to incorporate the effects of glucose on β-cell insulin production and release, under the assumption that attenuated protein translation is a feature of the UPR (Equations (5.1), Figure 5.2, Table 5.1). State variables include unfolded proinsulin protein, $B_{uu}(t)$; XBP1 mRNA, $B_{ux}(t)$; ER chaperone proteins, $B_{uc}(t)$; and folded insulin protein, $B_{uf}(t)$. The primary modifications of the Trusina et al. model are the inclusion of the glucose-dependent term in Equation (5.1a) and the addition of (5.1d) to describe the fate of folded insulin. We also include plasma glucose and insulin dynamics, but not detailed skeletal muscle dynamics (Equations (5.1e) and (5.1f)).

$$\text{Proinsulin protein:}\quad \frac{\mathrm{d}B_{uu}}{\mathrm{d}t} = h_{uu}\underbrace{\frac{G^2}{G^2+G_{hu}^2}}_{\text{production}}\cdot\underbrace{\frac{1}{1+K_{\mathrm{PERK}}\cdot\hat{u}(t)}}_{\substack{\text{translation}\\ \text{attenuation}}} - \underbrace{d_{uu}B_{uc}\frac{B_{uu}}{B_{uu}+K_{uu}}}_{\text{folding/degradation}} \tag{5.1a}$$

$$\text{Active XBP1 mRNA:}\quad \frac{\mathrm{d}B_{ux}}{\mathrm{d}t} = \underbrace{h_{ux}\hat{u}(t)}_{\text{IRE1}\alpha\text{ activity}} - d_{ux}B_{ux} \tag{5.1b}$$

$$\text{ER chaperones:}\quad \frac{\mathrm{d}B_{uc}}{\mathrm{d}t} = \sigma_{uc} + h_{uc}B_{ux} - d_{uc}B_{uc} \tag{5.1c}$$

$$\text{Insulin protein:}\quad \frac{\mathrm{d}B_{uf}}{\mathrm{d}t} = \underbrace{q_{uf}d_{uu}B_{uc}\frac{B_{uu}}{B_{uu}+K_{uu}}}_{\text{folding}} - \underbrace{k_{uf}GB_{uf}}_{\text{secretion}} \tag{5.1d}$$

$$\text{Plasma glucose:}\quad \frac{\mathrm{d}G}{\mathrm{d}t} = \sigma + h_g - k_gG - SGI \tag{5.1e}$$

$$\text{Plasma insulin:}\quad \frac{\mathrm{d}I}{\mathrm{d}t} = \hat{h}_iB\cdot k_{uf}GB_{uf} - k_iI, \tag{5.1f}$$

$$\text{with } \hat{u}(t) = \frac{B_{uu}/K_1}{1+\frac{B_{uu}}{K_1}+\frac{B_{uc}}{K_2\left(1+\frac{B_{uu}}{K_3}\right)}}.$$

- *Unfolded proinsulin.* Proinsulin production is stimulated by glucose in a sigmoidal manner [84], and the activity of UPR component PERK reduces this production (Equation (5.1a)). PERK is activated by newly synthesized proinsulin and is inhibited by a general

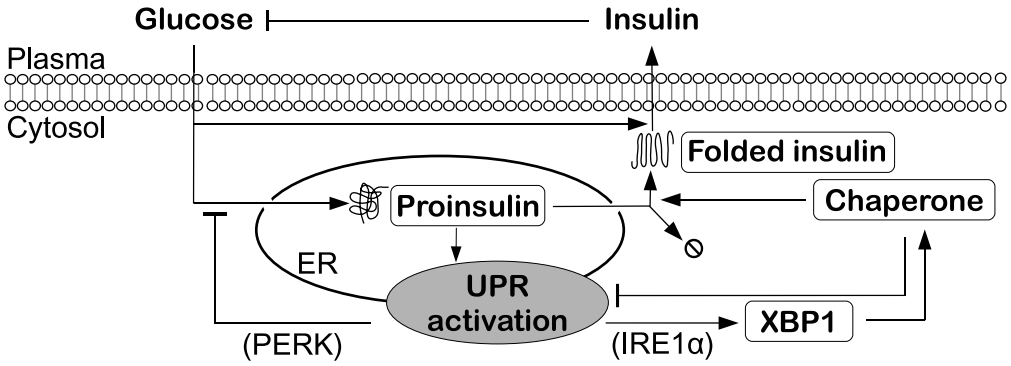

Figure 5.2. Model of β-cell function. Glucose stimulates proinsulin production and the secretion of stored, properly folded insulin into the plasma for glucose regulation. Unfolded proinsulin activates the UPR, which can carry out functions associated with either PERK or IRE1α. PERK-mediated action results in the attenuation of proinsulin translation, while IRE1α-dependent responses activate XBP1 mRNA to promote chaperone production. These chaperones are essential in the folding and degradation of proinsulin and also serve to negatively regulate UPR induction.

Table 5.1. Parameter descriptions for Equations (5.1). A summary of all values used appears in Table A.1.

Parameter	Value/Range	Units
d_{uc}	chaperone decay	min^{-1}
d_{uu}	proinsulin folding/degradation	min^{-1}
d_{ux}	XBP1 mRNA decay	min^{-1}
$\hat{h}_i$	plasma conversion factor	pM molecule^{-1} $(10^6 \text{ cells})^{-1}$
h_{uc}	XBP1-dependent chaperone production	molecules (mRNA level)$^{-1}$ min^{-1}
h_{uu}	proinsulin production	molecules min^{-1}
h_{ux}	IRE1α-induced XBP1 mRNA activation	mRNA level min^{-1}
K_{PERK}	maximal PERK activity	#
k_{uf}	insulin protein secretion	mM^{-1} min^{-1}
K_{uu}	proinsulin-chaperone Michaelis-Menten constant (folding/degradation)	molecules
K_1	PERK/IRE1α-proinsulin dissociation constant	molecules
K_2	PERK/IRE1α-chaperone dissociation constant	molecules
K_3	proinsulin-chaperone dissociation constant (chaperone sequestration)	molecules
q_{uf}	proinsulin folding fraction	mM^{-1} min^{-1}
σ_{uc}	basal chaperone production	molecules min^{-1}

class of ER chaperones, B_{uc}, according to Michaelis-Menten kinetics. B_{uc} removes proinsulin via folding and degradation, which are combined into a single term. We assume that misfolded proinsulin results in immediate degradation and that β-cell turnover, occurring on the order of months [78], does not have a significant impact on the presence of ER proinsulin.

- *XBP1 activity.* IRE1α is assumed to follow the same Michaelis-Menten kinetics as PERK, and its maximal activity level is absorbed in the production rate of active XBP1 mRNA (Equation (5.1b)). First-order degradation of active XBP1 mRNA occurs at rate d_{ux}. We use arbitrary units to describe mRNA levels.

- *ER chaperones.* ER chaperones are generated at a constant rate and undergo first-order degradation (Equation (5.1c)). XBP1 provides an additional source of chaperones through mRNA-mediated translation upregulation.

- *Folded insulin.* A fraction q_{uf} of removed proinsulin is assumed to be folded, thus entering the intracellular insulin compartment, which comprises both immediately accessible and stored insulin (Equation (5.1d)). We assume that the process of folded hormone transport to the Golgi apparatus and subsequent granule biosynthesis is immediate and that glucose leads directly to the release of insulin from this pool into the plasma.

- *Plasma.* Plasma glucose appears from exogenous (σ) and hepatic (h_g) sources and is removed by insulin-dependent and -independent means (Equation (5.1e)). We assume a constant number of β cells, B, and each of these is assumed to secrete an average amount $k_{uf}GB_{uf}$ of insulin protein, which is converted to plasma concentrations with factor $\hat{h}_i$ (Equation (5.1f)). First-order kinetics govern insulin clearance from the blood.

5.1.1 Response to daily meals

To assess the feedback dynamics within the UPR submodel, we solve the differential equations with a square wave food intake parameter, σ, defined in terms of the average daily change in the glucose area under the curve, ΔAUC. Results shown in Figure 5.3 correspond to ΔAUC = 1. Because PERK and IRE1α responses are induced identically, we describe overall UPR effector activity with $\hat{u}$ and discuss its differential effects with respect to the present simulation. At the onset of the first meal (M1), all variables, save the chaperones and folded insulin, rise rapidly. ER chaperones experience a delayed increase, while the insulin protein level within the β cell falls at a similar rate. At hour six, the rapid increase in glucose causes similar behavior

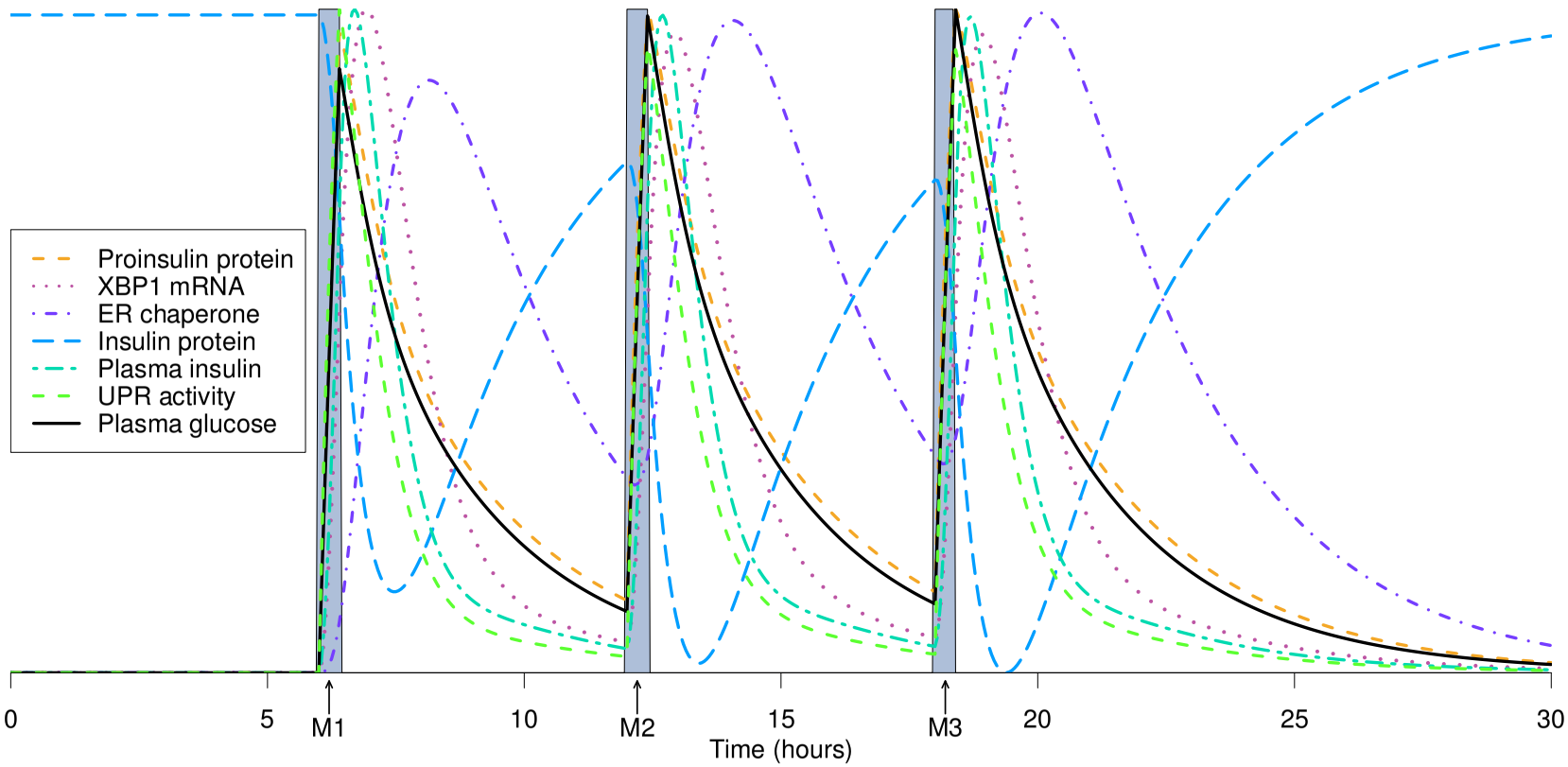

Figure 5.3. Dynamics of system (5.1) over a 30-hour period. Trajectories for all state variables are scaled to demonstrate the relative behavior of the model. 24-minute meals are simulated as square waves and applied at hours 6, 12, and 18, or equivalently, 6 a.m., 12 p.m., and 6 p.m. Meal intervals (gray regions) are denoted by M1, M2, and M3. UPR activity is determined by the expression $\hat{u}$. Results are shown for $\Delta\text{AUC} = 1$.

in proinsulin and consequently in UPR activity. For the duration of M1, intracellular insulin content declines substantially due to the required increase in insulin secretion. This leads to elevated plasma insulin, which peaks shortly after the conclusion of M1. XBP1 production tracks the dynamics of IRE1α-mediated UPR activity, achieving a local maximum after peak UPR induction. ER chaperone proteins follow suit, as they respond to activated XBP1 mRNA. Recovery of insulin protein in the β-cell occurs after the peak in proinsulin production and the folding activity of chaperones. Prior to the start of M2, no variable returns to its basal level. More dramatic differences from baseline are apparent in proinsulin, insulin protein, glucose, and chaperone proteins. Slow decay of chaperones influences the continued decrease in proinsulin and concurrent rise in folded insulin, but the delayed peak prevents restoration of basal activity before the beginning of M2.

Because ER chaperones remain elevated, when the glucose concentration begins its second rise, a greater maximal chaperone amount is achieved, but with a smaller net change. This is precipitated by an XBP1 response that is also smaller in amplitude than the response mounted with M1, likely due to the reduced change in proinsulin. As with glucose, proinsulin does not decay to baseline in the inter-meal period from M1 to M2. However, the ability of β cells to generate a sufficient insulin response is due to the continued presence of elevated chaperones, which reduce UPR activity and consequent protein attenuation, yet promote insulin folding. Maximal XBP1 mRNA levels are lower than with M1, which reduces the net gain in ER chaperones. Nevertheless, the higher peak in chaperone number allows plasma insulin production to remain intact.

Responses to M3 closely resemble those of M2, with the exception that the 12-hour period without meals after M3 gives the system more opportunity to return to a basal state. However, the perturbations in glucose appearance are too large to achieve full restoration of the original state; this indicates a slight desensitization of regulatory responses, which is reflected in the deviation of each quantity from its basal level just before the onset of the next meal at hour 30.

We also detail model behavior over a period of three days, for integer values of ΔAUC between 0 and 4.0. (Figure 5.4). Higher levels of nutrient intake increase all components of β-cell function, namely proinsulin, XBP1 mRNA, and ER chaperones. The decrease in insulin protein levels with elevated ΔAUC indicates heightened secretory function within individual cells, draining intracellular stores before they are restored by proinsulin production. Because we currently assume a constant β-cell population, compensatory insulin release depends entirely on the ability of each cell to increase its own hormone production. Larger values of ΔAUC also

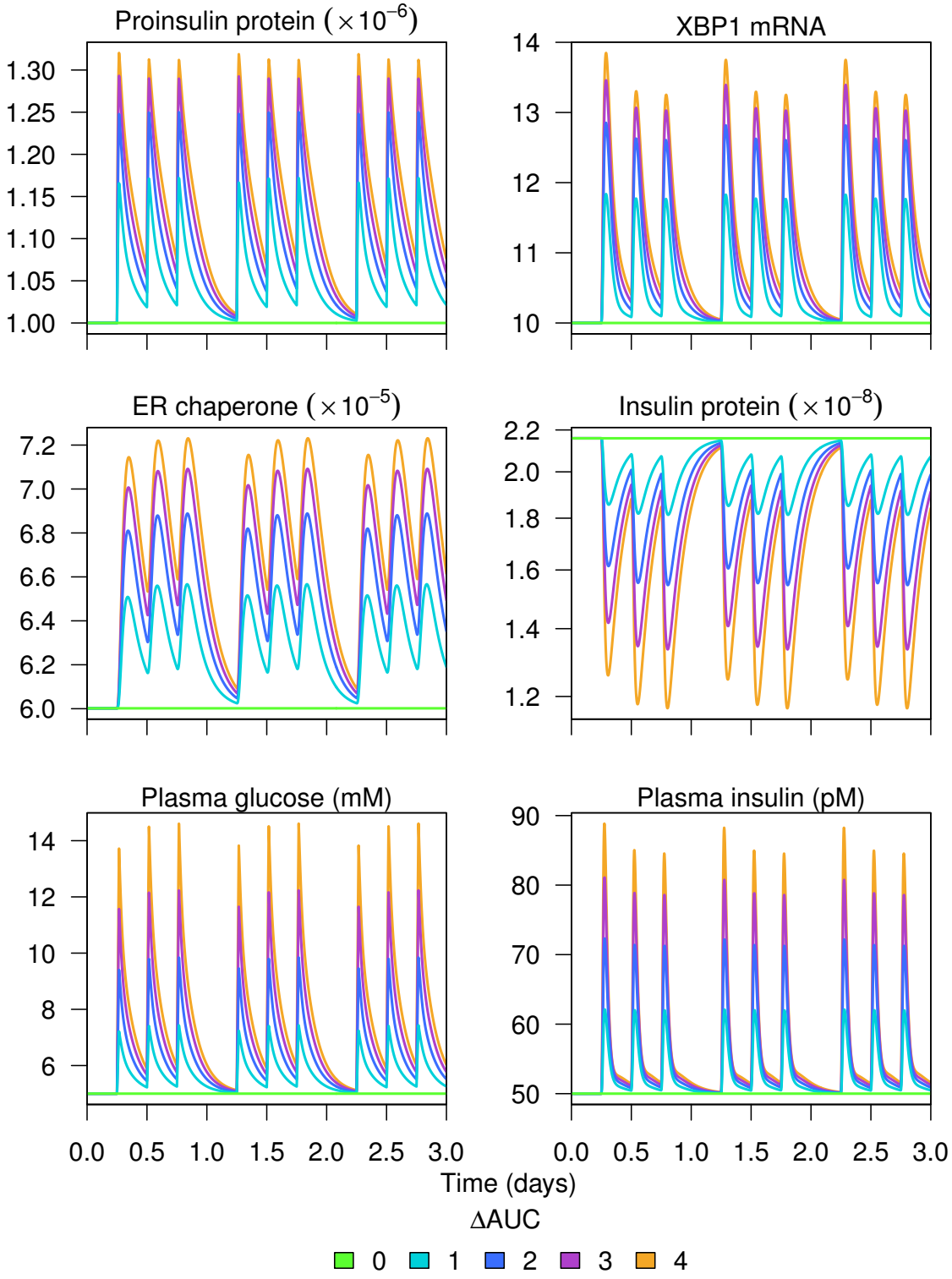

Figure 5.4. β-cell function model behavior over three days for varying levels of food intake.

lengthen the return time toward basal values. However, over the course of three days, there are no significant changes in basal levels.

Nevertheless, UPR activity is altered due to increased nutrient excess. Glucose stimulates the appearance of proinsulin in the ER, but this effect saturates for high glucose, leading to a smaller increase in the protein. In addition, ΔAUC enhances UPR activation, which has multiple effects. With 6-hour inter-meal periods, a sufficiently active UPR reduces the maximal proinsulin levels reached after the first meal of the day, leading to a similar effect on XBP1 mRNA. When $\Delta\text{AUC} \leqslant 2$, PERK inhibition due to residual chaperone elevation outweighs the effect of proinsulin-mediated activation, resulting in higher peak proinsulin with the second and third meals of each day. Similarly, limited IRE1α responses reduce maximal XBP1 mRNA induction. On the other hand, when $\Delta\text{AUC} > 2$, increased PERK activity after breakfast decreases the maximal proinsulin amounts attained with lunch and dinner. Simultaneously, increased IRE1α activity leads to more drastic decreases in XBP1 mRNA than with smaller ΔAUC.

5.1.2 Summary

Our model of β-cell function reveals the nature of insulin production from the perspective of an individual cell. Cellular function is preserved by the induction of the UPR in the presence of elevated ER protein loads. This response reduces the stress placed on the cell while enhancing its capacity to process insulin for secretion into the blood. Once the cell has adapted to the increased workload, it relaxes to a near-basal state. Glucose regulation therefore relies on the ability of β cells to maintain a balance between supply and demand. Omitted from the present framework is the consideration of β-cell mass plasticity, which can also impact the response to a heightened demand for insulin.

5.2 Model of metabolic regulation with β-cell dynamics

5.2.1 Unregulated β-cell mass

β cells adapt to changes in the metabolic environment by altering their secretory capacity, size, or number. Because the metabolic activities of these cells occur on a shorter time scale than their population dynamics, significant modifications to β-cell numbers will only appear over the long term. We introduce the differential equation

$$\frac{\mathrm{d}B}{\mathrm{d}t} = \left(h_b \frac{G^2}{G^2 + G_{hb}^2} - k_b \right) B \tag{5.2}$$

to describe the dynamics of β-cell mass, $B(t)$. We ignore hypertrophic and hypotrophic effects by assuming that all β cells have equal, constant volume, and we restrict ourselves to changes

in total cell number. Henceforth, reference to β-cell mass is equivalent to that of β-cell number. Glucose stimulates the replication of β cells according to a second-degree Hill function, which is similar to the form used in De Gaetano et al. [24]. We further assume that *de novo* production of β cells is negligible and that cellular turnover occurs at constant rate k_b.

We explore the long-term interaction of nutrient excess, oxidative stress, mitochondrial damage, and β-cell mass (Figure 5.5), by appending Equation (5.2) to a complete model composed of systems (4.15) and (5.1). We eliminate equation (5.1e), and we replace (4.15b) with (5.1f). We initialize the system under the assumption that glucose is in equilibrium according to a given σ and set $\hat{s} = (\sigma + h_g - k_g G_0)/(G_0 U_0)$ for each ΔAUC-determined σ. $G(0) = 5$ mM for all ΔAUC.

Elevated nutrient intake initially leads to sharp increases in plasma glucose and insulin. Similar behavior occurs in proinsulin and ER chaperones, accompanied by equivalent reductions in β-cell insulin protein and in the amount of GLUT4 at the membrane of skeletal muscle cells. These rapid increases near time $t = 0$ occur because the system is not yet calibrated to higher glucose loads, and they invoke an adaptive β-cell response in the form of increased mass. Large ΔAUC promotes more profound β-cell mass expansion, which consequently restores basal quantities of glucose and other glucose-responsive variables, including GLUT4, unfolded proinsulin, and folded insulin.

Excess glucose also leads to increased skeletal muscle oxidative stress-mediated IRS-1 serine phosphorylation, which approaches an equilibrium level upon total mitochondrial damage. When compared to the results of the model without β-cell dynamics, the timing of global mitochondrial dysfunction remains the same. This is because the level of total glucose uptake is identical to that of the previous model and similarly maintained at a constant rate. The effects of muscle mitochondrial dysfunction, however, are different with the inclusion of β-cell function. A jump in serine phosphorylation gives rise to an immediate decline in membrane GLUT4, which creates a sharp increase in plasma glucose. The response of glucose under these conditions influences β cells in two ways. On the one hand, intracellular proinsulin and chaperone production rise, and more insulin protein is secreted. On the other hand, β-cell mass responds to a greater demand for insulin with increased replication, leading to a higher plasma insulin concentration. The spike in plasma insulin immediately reverses the effects of dysfunctional skeletal muscle cells, as glucose, GLUT4, proinsulin, chaperones, and folded insulin all return to their basal levels.

In the absence of β-cell mass adaptation, that is, when $B'(t) = 0$, glucose dysregulation

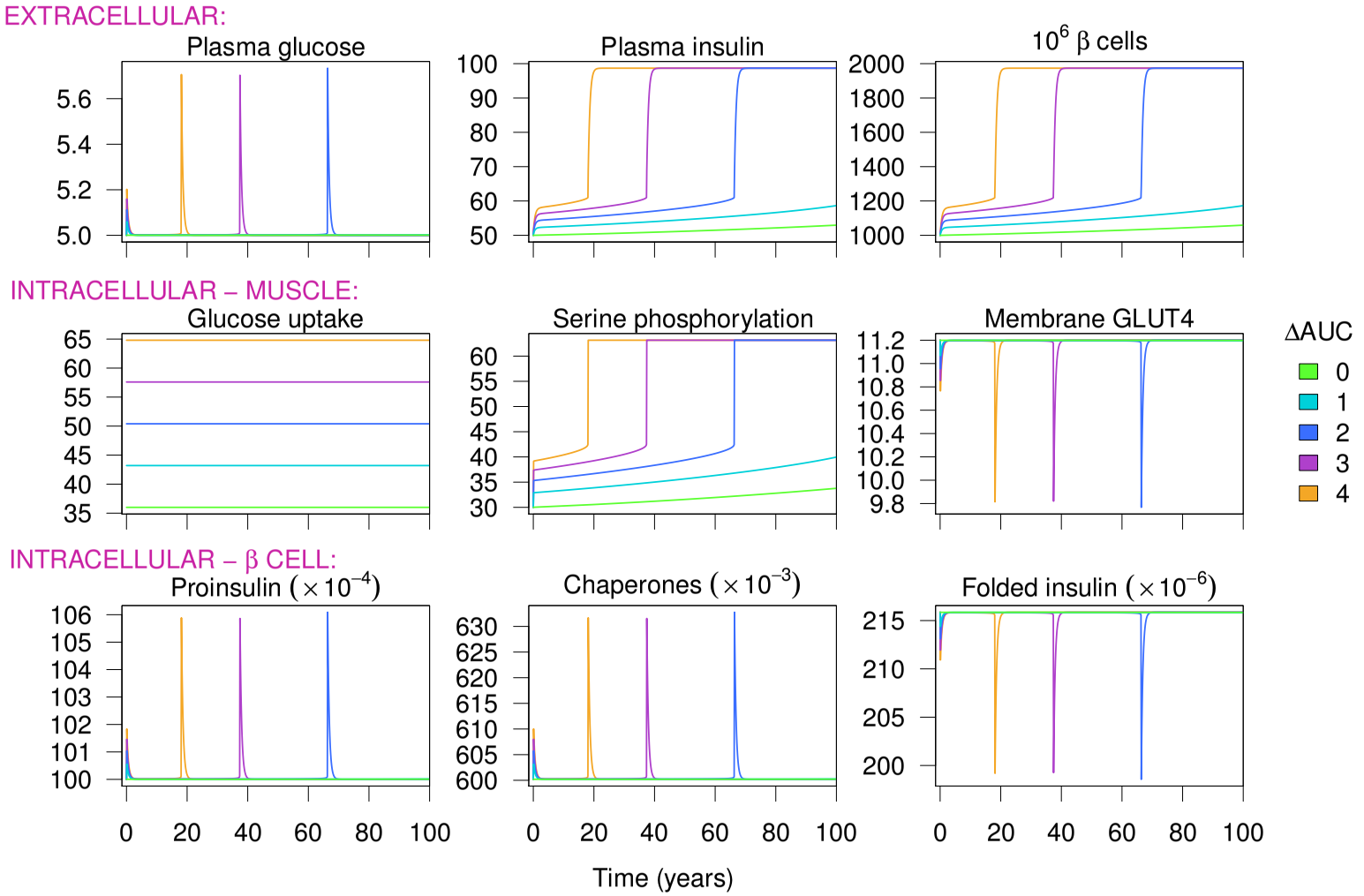

Figure 5.5. Dynamics of the full metabolic system for selected variables over a 100-year period. Units: plasma glucose, mM; plasma insulin, pM; β-cell mass, 10^6 cells; glucose uptake, mM/min; hydrogen peroxide, μM; GLUT4, percent; proinsulin/chaperones/folded insulin, molecules.

eventually occurs (Figure 5.6). Initially, the elevated glucose input leads to a jump in the plasma concentration; in contrast to the model with a dynamic β-cell population, this sharp rise is never reversed. Glucose slowly increases, as insulin resistance develops. Additionally, insulin is augmented with higher ΔAUC, but the magnitude of compensation is reduced, when compared to the dynamics illustrated in Figure 5.5. Upon total mitochondrial dysfunction in muscle, the secretory capacity of β cells is overwhelmed, and the glucose concentration reaches a steady state within the impaired range (between 5.6 and 7 mM [3]). Amplified basal insulin secretion is the result of increased glucose intake, which suggests that expansion of the β-cell population is required for normal glucose tolerance in the presence of severe insulin resistance.

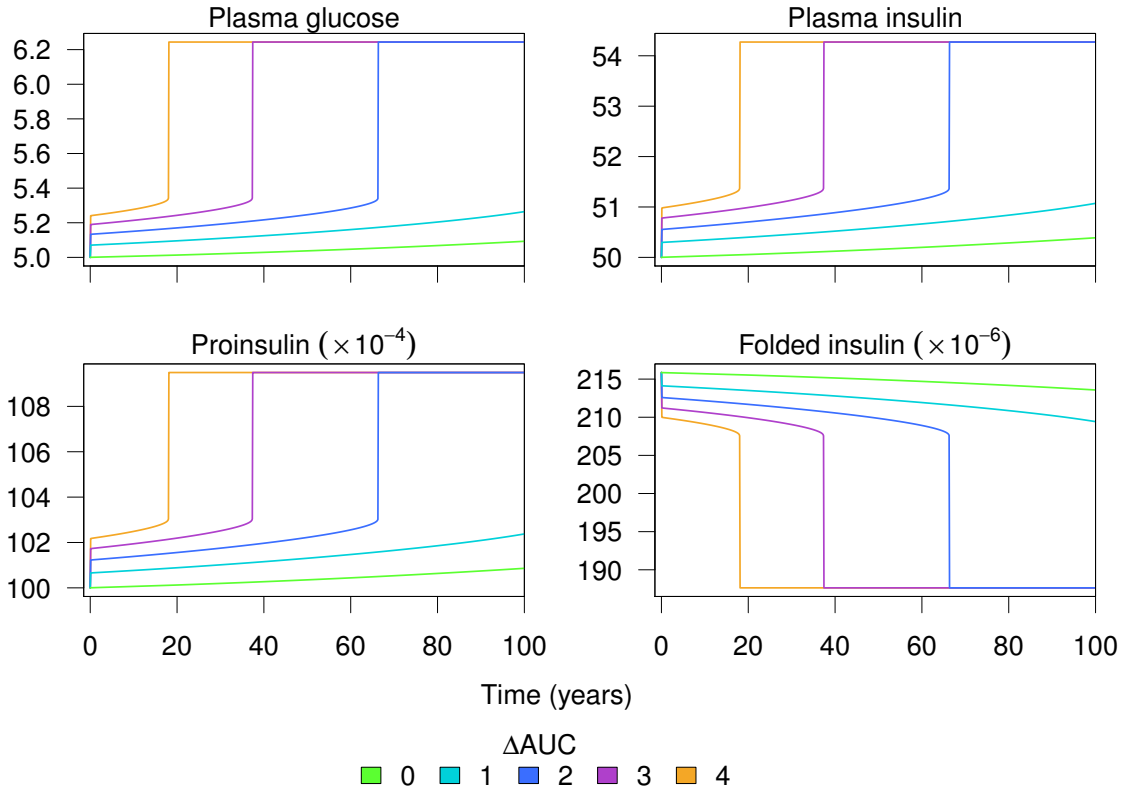

Figure 5.6. Dynamics of the full metabolic system with β-cell function and constant β-cell mass. Units: plasma glucose, mM; plasma insulin, pM; β-cell mass, cells; glucose uptake, mM/min; hydrogen peroxide, μM; GLUT4, percent; proinsulin, chaperones, and folded insulin, molecules.

5.2.1.1 Summary

The results of the full model reveal a progressively insulin-resistant state, characterized by hyperinsulinemia and increased β-cell mass, along with a normal glucose concentration. With higher ΔAUC, more insulin is required to combat the lower sensitivity of skeletal muscle cells to insulin. As a result, individual β cells produce more proinsulin and secrete more insulin into the blood. This process works for a time, but with skeletal muscle dysfunction, glucose dysregulation occurs, forcing β cells to increase their mass in order to satisfy an increased demand for insulin. This leads to a plateau of insulin at a higher level and the restoration of the basal glucose concentration. The hallmark of this model is insulin resistance that is fully compensated by β-cell secretory and replicative function.

Prior to the onset of complete mitochondrial dysfunction, UPR feedback minimally contributes to the maintenance of normal glucose concentrations in the face of worsening insulin resistance. A switch to predominately β-cell mass-mediated compensation occurs, relieving the pressure on individual β cells. At this point, β cells secrete only a basal amount of insulin, independently of ΔAUC, whereas insulin requirements are fully met with a greater number of β cells. In this light, extreme nutrient excess can only ever lead to severe insulin resistance, but not insulin deficiency, as in type 2 diabetes. These results suggest that negative feedback on β-cell population dynamics or on β-cell function is necessary in the development of type 2 diabetes, which may also highlight a larger role for β-cell loss in disease development.

5.2.2 Apoptotic regulation of β cells

Heretofore, we have neglected the effects of UPR activation on the β-cell population. Prolonged activation of the UPR can generate regulatory proapoptotic signals, which occurs when excessive ER stress impairs the cell's ability to restore homeostasis [66]. In the case of constant σ, β-cell loss can only occur within the average lifespan if glucose and insulin dynamics closely track those of UPR-activated proapoptotic signaling (not shown). This suggests the presence of more complex mechanisms driving the loss of β cells in diabetes development. We hypothesize that the pattern of ingestion, along with the total amount of nutrient intake, makes a significant difference.

The Trusina et al. UPR model demonstrates that the magnitude and duration of imposed ER stress influences the benefit of translation attenuation [97]. As discussed in Section 5.1, increased ΔAUC leads to delayed restoration of basal ER activity. It is the relatively short-term, yet constitutive, activation of the UPR that can activate proapoptotic signals, thus altering β-cell

turnover rates. Over the course of a lifetime, periodic meal pulses generate doses of ER stress that, under normal circumstances, is reconciled prior to the significant activation of death signals. With sufficiently large insulin demand, UPR activation, due to upregulated proinsulin production and processing, is sustained over longer intervals; if stress attacks increase the ER workload substantially, the protective response is further heightened, placing the cell in a more precarious state than does an isolated challenge to the system.

As "prolonged" activation requires both pulsatile input and a failure to recover the basal state, we explore the implications of periodic meals on PERK activity and β-cell dynamics. Let $Z(t)$ be the level of proapoptotic activity, governed by

$$\frac{\mathrm{d}Z}{\mathrm{d}t} = h_z K_{\mathrm{PERK}}(\hat{u}(t) - \hat{u}_0) - d_z Z. \tag{5.3}$$

Z increases according to the change in PERK from its basal level and is assumed to decay rapidly with rate d_z. The effect of proapoptotic signaling activity is to enhance β-cell turnover. We modify the rate of change of $B(t)$ to be

$$\frac{\mathrm{d}B}{\mathrm{d}t} = \left[h_b \frac{G^2}{G^2 + G_{hb}^2} - k_b(1 + \eta_z Z) \right] B, \tag{5.4}$$

where η_z is the effectiveness with which Z mediates β-cell apoptosis.

We simplify the dynamics of the full system by restricting ourselves to a truncated timeline of glucose metabolism, in which seven-day snapshots of metabolic regulation are taken for discrete levels of insulin resistance (Figure 5.7). Food intake parameter σ is again applied as a square wave for varying ΔAUC. Assuming an input of cytosolic hydrogen peroxide alters the level of insulin resistance in a skeletal muscle cell over time, we include only the insulin signaling dynamics from Chapter 4 and omit intramitochondrial activity:

$$\begin{aligned}
&\text{Phosphorylated tyrosine residues:} && \frac{\mathrm{d}P_y}{\mathrm{d}t} = \alpha_y \frac{I}{I + I_h}(1 - P_y)(1 - P_s) - \delta_y P_y \\
&\text{Phosphorylated serine residues:} && \frac{\mathrm{d}P_s}{\mathrm{d}t} = \alpha_s(1 - P_s)\frac{J_{\max} R_h}{R_h + \hat{j}} - \delta_s P_s \\
&\text{Fraction membrane GLUT4:} && \frac{\mathrm{d}U}{\mathrm{d}t} = \left(\alpha_u + \eta_p \frac{P_y}{P_y + \hat{p}} \right)(1 - U) - \delta_u U,
\end{aligned} \tag{5.5}$$

where hydrogen peroxide, R_h, is treated as a parameter to specify the level of insulin resistance.

The four panels of Figure 5.7 correspond to ΔAUC = 0.5, with R_h = 0.0100, 0.0115, 0.0130, and 0.0145, from left to right, where R_h = 0.01 is the basal hydrogen peroxide concentration used in previous chapters. We assume that larger R_h values represent age-related worsening of insulin resistance and that each phase begins with a proapoptotic signal level of zero. Black and

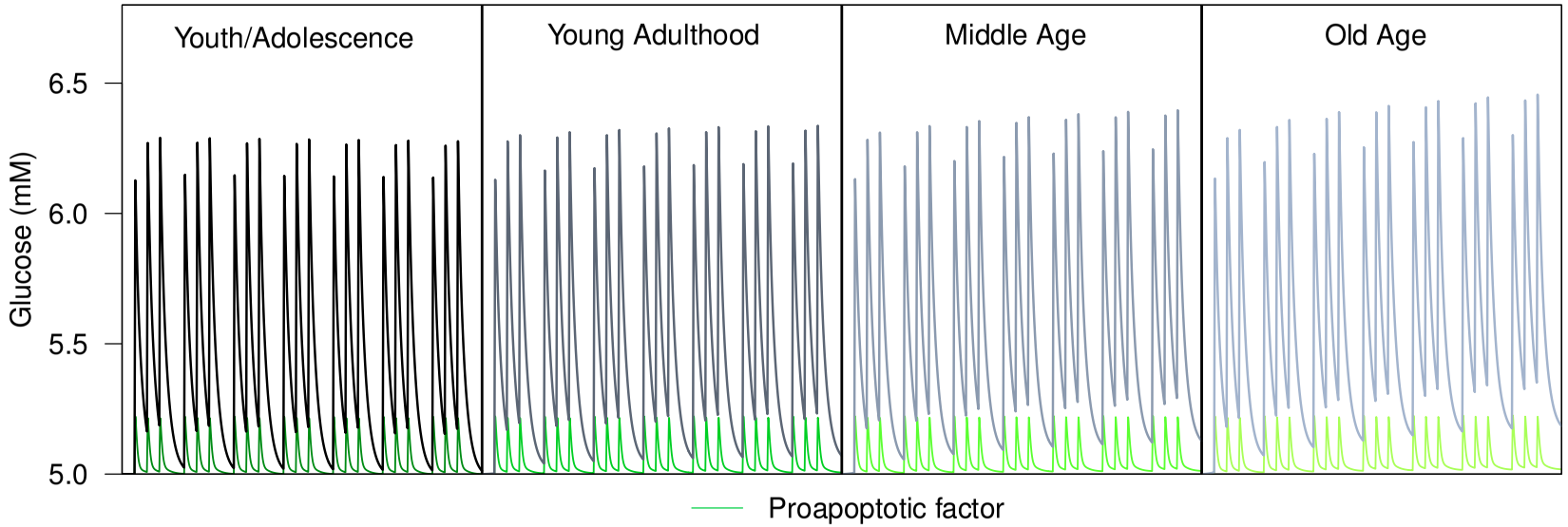

Figure 5.7. Four-stage response of pulsatile glucose input on metabolic regulation. Each stage provides a particular level of insulin resistance, as determined by the effect of varying hydrogen peroxide on skeletal muscle glucose uptake capacity.

gray lines reflect glucose dynamics within a given life stage, and green lines their corresponding proapoptotic activity. Progressive lightening of these lines indicates more advanced life stages. During the adolescent period, glucose input is tightly regulated with each stimulus, as plasma glucose returns to its basal level of 5mM. Similarly, the proapoptotic signal induced by UPR activation returns to its initial level of zero. Through young adulthood and middle age, higher levels of insulin resistance lead to increased UPR activation, β-cell apoptosis and elevated basal glucose levels. At the height of insulin resistance in old age, glucose regulation is less efficient, and β-cell compensation is restricted by apoptosis to a larger extent than in earlier stages. As a result, the effects of heightened insulin demands and β-cell decompensation are more apparent. Overnutrition is less important because basal glucose levels fall well within the normal range, that is, below 5.6 mM, even with an age-related increase in insulin resistance. Nevertheless, this example suggests that over an extended period of time, the combined effect of increased β-cell function and apoptotic feedback mechanisms, along with nutrient overload and a sufficiently high insulin demand, promotes gradual β-cell loss.

5.3 Discussion

Our model gives insight into the nature of β-cell function, from both a natural and compensatory standpoint. Adaptation of β cells to changes in insulin demand occur at both molecular and population levels. When the increase in the requisite concentration of insulin to maintain normoglycemia is small, β cells can adapt by increasing insulin secretion per cell. However, in the case of severe insulin resistance, more dramatic changes in β-cell mass are necessary to conserve individual cellular function and meet metabolic demands. This compensatory behavior protects β cells from ER stress, thereby limiting UPR induction. Our model implies that such a mechanism is enough to prevent the development of type 2 diabetes. However, with the consideration of proapoptotic consequences of constitutive UPR activation, we find that β-cell mass is more susceptible to loss with increasingly severe insulin resistance, supporting the additive effect of increased apoptosis as an additional mechanism for β-cell decompensation.

Although improperly folded proinsulin leads to its UPR-mediated degradation, an explicit description of these proteins has been omitted from our model [79]. The role of misfolded proteins in β-cell function resembles that of unfolded proteins, as they also induce UPR activity. We indirectly include abnormal proinsulin processing by assuming that some fraction of the proinsulin degraded also includes degraded misfolded proinsulin. With this in mind, consideration of these abnormal proteins in the UPR framework would not contribute signifi-

cant changes to the model. Still, as the demand for insulin increases, the likelihood that folding mistakes are made also increases, and misfolded proteins will aggregate more quickly when the ER is overworked [66]. The additional biological complexity this creates is important if the UPR is more sensitive to abnormally folded proteins than unfolded ones, in either its initiation or targeting effector responses. We hypothesize that explicitly described misfolded proteins can reduce the amount of folded insulin protein through competition, wherein more chaperone activity would be diverted from proinsulin folding to degradation of defective proteins. It remains to be determined whether such a reduction in folded protein would significantly impact the plasma insulin concentration.

Notably, the snapshots presented in Figure 5.7 are not illustrative of the typical trajectory for glucose metabolism during the course of a lifetime. Instead, they represent isolated responses to a particular level of insulin resistance. This is important because we assume identical initial conditions for each 7-day period, ignoring the metabolic changes that may have occurred prior to the beginning of each phase. Were this model solved for thrice-daily meals over several decades, we hypothesize that the glucose excursions seen in the “old age” phase would deviate farther from the basal level, as the cumulative metabolic history would determine the initial state of this life stage.

In this chapter, we have completed a model of glucose metabolism and mechanisms of dysfunction. It is evident that a multitude of causative factors are responsible for the progression of type 2 diabetes, and we have highlighted oxidative stress, mitochondrial dysfunction, and the unfolded protein response as sources of metabolic dysregulation in disease development.

CHAPTER 6

CONCLUSION

This work has focused on the coordinated function and dysfunction of skeletal muscle and β cells in glucose metabolism. We have provided a mathematical model of the mechanisms underlying age- and glucose-mediated skeletal muscle insulin resistance, and we have detailed its impact on the dynamics of the glucose-insulin regulatory system, with particular attention to mitochondrial abnormalities and oxidative stress. We have also presented a model of β-cell function, with feedback provided by the unfolded protein response, to outline mechanisms of β-cell decompensation. Combining these models, we have developed a long-term mathematical model of mechanisms underlying the progression of type 2 diabetes.

Skeletal muscle is the major tissue addressed in our discussion of insulin resistance. However, other insulin-responsive tissues do acquire insulin resistance, particularly in obesity. In this chapter, we discuss mechanisms of obesity-related dysfunction in type 2 diabetes pathogenesis for consideration in future work.

Obesity is highly correlated with type 2 diabetes, yet less than half of obese individuals actually develop the disease. This fact may be explained by a propensity toward β-cell dysfunction in this subset [28], but less straightforward is the reason for inter-individual variability in the molecular presentation of obesity-related insulin resistance, which can also impact the likelihood of disease manifestation. As such, we look to mechanisms of adipose tissue insulin resistance and its systemic effects for answers.

Conditions of overnutrition often result in the expansion of white adipose tissue, which comprises subcutaneous and visceral subtypes, SAT and VAT, respectively. SAT and VAT are the major sites for fat storage, and because they are functionally distinct, fat partitioning may play a role in the development of obesity-related diabetes [69]. Predominant fat storage in SAT may systemically provide protection from fat-mediated defects, whereas VAT storage of fuel excess leads to progressive tissue dysfunction and insulin resistance [69, 89]. This generates questions regarding the specification of adipocyte phenotypes and the switch underlying preferential expansion in an over-fueled environment.

Associated with increased adiposity is inflammation, which is one source of systemic insulin resistance. Recruitment and infiltration of macrophages in expanding adipose tissue, particularly in VAT [102], is now the widely accepted origin of the elevated TNFα expression observed in obesity [6, 82]. Interestingly, the distribution of resident adipose tissue macrophages is thought to be divided between the classically activated, Th1-mediated M1 phenotype and the alternatively activated, Th2-mediated M2 phenotype [61]. It is proposed that dynamic remodeling or switching of adipose tissue macrophage phenotypes occurs in a state of obesity, but the precise mechanism remains to be elucidated [28, 61]. Notably, dysfunctional VAT appears to produce more proinflammatory cytokines than SAT does [28, 89], and pathological function of antibody-producing B cells may contribute to such production [102]. We can address the question of phenotypic expression of macrophages either alone or in the context of distinct expanding adipose tissue environments.

Inflammation and adipose-secreted cytokines can cause insulin signaling defects through inhibitory serine phosphorylation of the IRS proteins in various tissues [2, 20]. We now discuss insulin action and insulin resistance in adipose tissue, to further dilineate the systemic effects of obesity-induced inflammation. Insulin signals triglyceride (TG) synthesis in adipocytes for storage and greatly inhibits lypolysis and the release of free fatty acids (FFAs) into plasma [105]. Insulin resistance in these tissues therefore reduces TG synthesis and increases FFAs in the blood, for which other tissues and organs can compensate by storing fat. Preferential lipid synthesis in skeletal muscle and liver, however, reduces glucose oxidation and uptake, thus desensitizing these cells to insulin [80]. Furthermore, the TG precursor, diacylglycerol (DAG), is more recently believed to directly initiate signaling events that promote serine phosphorylation of IRS proteins and insulin resistance [6]. Endocrine function is also at risk, as increased concentrations of circulating FFAs are toxic to β cells, providing an additional basis for β-cell failure in type 2 diabetes [56, 80]. We can therefore assess the role of FFAs as additional mediators of systemic insulin resistance and glucose dysregulation in late type 2 diabetes development.

Liver dysfunction in type 2 diabetes is also exacerbated by the presence of adipose tissue insulin resistance. The increased release of FFAs from these tissues can result in enhanced lipogenic activity and fat accumulation in the liver, resulting in hepatic insulin resistance [82]. Such resistance reduces insulin's ability to suppress hepatic glucose production after eating, which can to lead to fasting hyperglycemia [69, 90]. However, metabolic dysfunction of the liver seems to rely on preexisting abnormalities that carry more weight than increases in glucose production, which themselves resemble elevated dietary sugar intake [69]. Hence, we deem

adiposity as the reasonable next step on which we can expand our mechanistic treatment of type 2 diabetes progression (Figure 6.1).

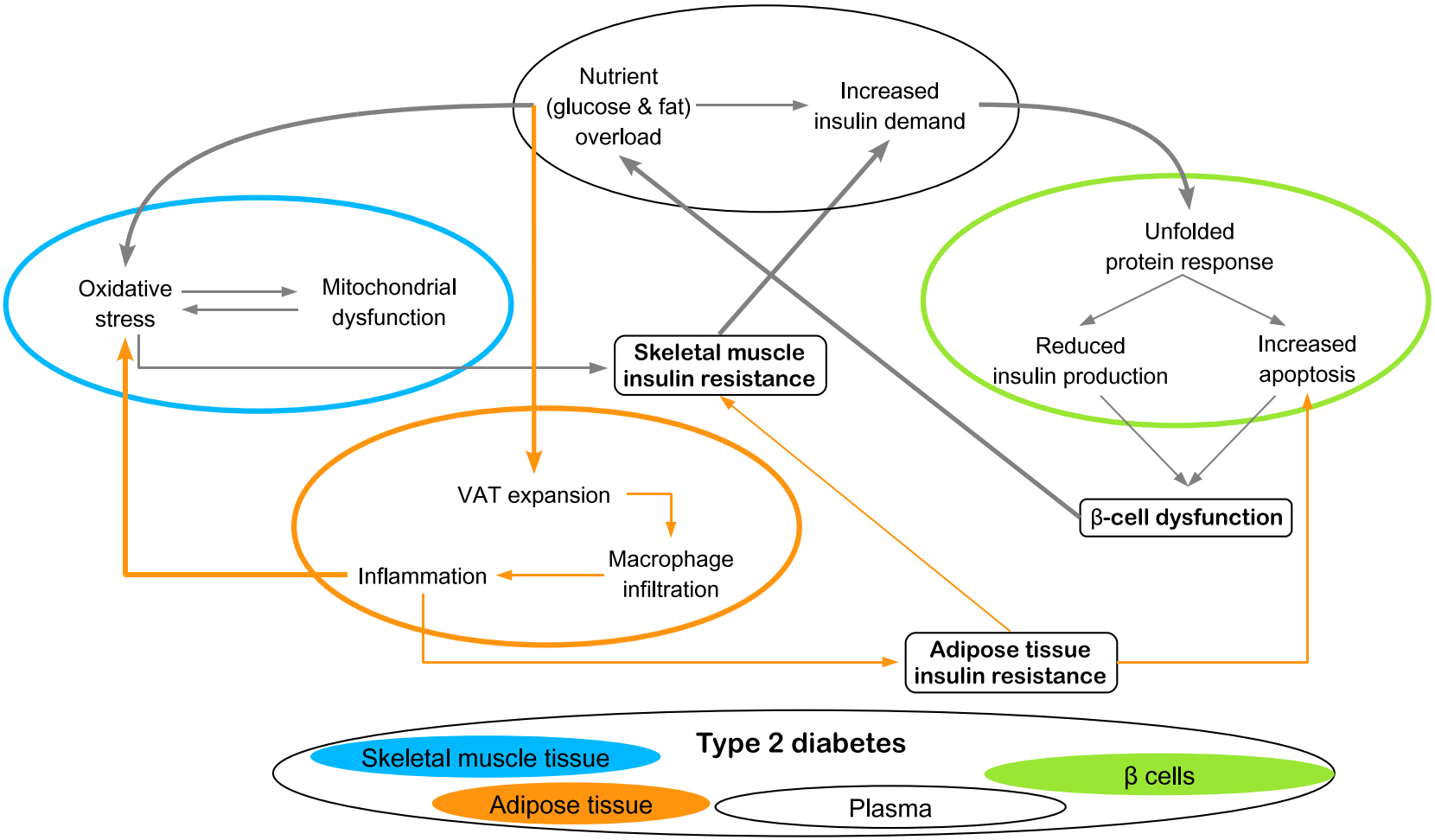

Figure 6.1. Expanded mechanisms of type 2 diabetes progression. In future work, we intend to incorporate mechanisms of dysfunction that are mediated by obesity and overnutrition, including preferential VAT expansion and the resulting signals generated by recruitment of proinflammatory macrophages into these tissues. Further, we can assess the systemic effects of adipose tissue insulin resistance, e.g., in β-cell loss and in skeletal muscle oxidative stress. VAT: visceral adipose tissue.

APPENDIX A

PARAMETER VALUES

Table A.1 is a comprehensive annotated list of all parameter values. Each value is discussed in detail in the following sections.

Table A.1. List of all parameter values used in the main text. *See text for details.

	PARAMETER	VALUE	UNITS	REFERENCE
Superoxide Production	a_a	1.04×10^{-2}	min^{-1}	*
	a_e	104.1667	min^{-1}	*
	B	1000	10^6 cells	[24]
	G_h	9.0	mM	[24]
	h_g	0.025	mM min^{-1}	derived
	h_i	2.8744×10^{-2}	$(10^6 \text{ cells})^{-1}$ min^{-1}	derived
	k_c	1200	min^{-1}	*
	k_e	7.6678×10^{-4}	min^{-1}	*
	k_g	0	min^{-1}	[24]
	k_{gi}	1.282×10^{-3}		derived
	k_i	0.05	min^{-1}	[24]
	k_{rs}	2.4×10^5	μM^{-1} min^{-1}	[35]
	N_e	20	mM^{-1}	[59]
	q_a	10^{-3}	#	*
	q_r	8×10^{-5}	#	*
	S	10^{-4}	pM^{-1} min^{-1}	[24]
	v_1	1/19.5	#	*
	v_2	15600	#	*
	ξ	8×10^{-6}	d^{-1}	*
Mitochondrial Selection	b_0	0.07	d^{-1}	*
	b_1	0.0644	d^{-1}	derived
	c	0.2	#	*
	d_0	0.07	d^{-1}	[30]
	d_1	0.056	d^{-1}	derived
	K	500	mitochondria	*
	μ	10^{-6}	#	*
	s	0.08	#	[60]

Continued on next page

Table A.1. Continued

	PARAMETER	VALUE	UNITS	REFERENCE
Insulin Signaling	A_h	3.0	μM	[83]
	α_s	0.4286	min^{-1}	derived
	α_u	0.00696	min^{-1}	[85]
	α_y	4.16	min^{-1}	[85]
	δ_{rh}	3000.0	μM^{-1} min^{-1}	[83]
	δ_s	0.0001	min^{-1}	*
	δ_u	0.167	min^{-1}	[85]
	δ_y	0.33557	min^{-1}	[85]
	η_p	0.104375	min^{-1}	[85]
	I_h	1.2×10^3	pM	*
	$\hat{j}$	200.0	μM	[104]
	J_{max}	2.0	#	*
	$\hat{p}$	1.64909	#	*
	q_h	0.015	#	derived
β-Cell Function	d_{uc}	1/120	min^{-1}	[97]
	d_{uu}	4.0362	min^{-1}	derived
	d_{ux}	1/30	min^{-1}	[97]
	d_z	2.0	min^{-1}	*
	η_z	0.5	#	*
	G_{hb}	5	mM	[24]
	h_b	0.0334	d^{-1}	derived
	$\hat{h}_i$	1.158×10^{-9}	pM molecule^{-1} $(10^6 \text{ cells})^{-1}$	derived
	h_{uc}	500	molecules (mRNA level)$^{-1}$ min^{-1}	[97]
	h_{uu}	2.5×10^7	molecules min^{-1}	[84]
	h_{ux}	6.2239	mRNA level min^{-1}	derived
	h_z	1/120	min^{-1}	*
	k_b	1/60	d^{-1}	[78]
	K_{PERK}	100	#	[97]
	k_{uf}	0.002	mM^{-1} min^{-1}	[15, 16]
	K_{uu}	10^4	molecules	[97]
	K_1	10^6	molecules	[97]
	K_2	6000	molecules	[97]
	K_3	2×10^5	molecules	[97]
	q_{uf}	0.9	mM^{-1} min^{-1}	*
	σ_{uc}	1.5	molecules min^{-1}	[97]

A.1 Superoxide Production

A.1.1 Glucose-insulin subsystem

- *Initial conditions.* We make the assumption that $F_1'(0) = 0$ for all variables $F_1(t)$ in subsystem (2.1). As in [24], we assume that plasma glucose and insulin take on their basal values initially: $G_0 = 5$ mM and $I_0 = 50$ pM, respectively. Because intracellular glucose concentrations are difficult to determine [106], we arbitrarily set $G_{i0} = 1$ mM.

- *β-cell mass, B.* β-cell mass is estimated to be on the order of 10^9 cells in [24]. In millions of cells, we therefore use $B = 1000$.

- *Half-maximal glucose stimulation, G_h.* As in [24], we use a value of 9.

- *Hepatic glucose production, h_g.* With the assumption that $G'(0) = 0$ without additional glucose input due to diet, we derive h_g to be $k_g G_0 + S G_0 I_0 = 0.025$.

- *Insulin production, h_i.* With $I'(0) = 0$, h_i is derived to be $k_i I_0 (G_0^4 + 9^4)/(B G_0^4) = 0.028744$.

- *Insulin-independent glucose uptake, k_g.* This version of the glucose subsystem is adapted from a previous model by [24]. The value used is therefore $k_g = 0$.

- *Glycolytic rate, k_{gi}.* From $G'(0) = 0$, this value is derived to be

$$k_{gi} = \upsilon_1 S G_0 I_0 / G_{i0} = 0.001282.$$

- *Insulin clearance, k_i.* First-order clearance of insulin is assumed to occur at a normal rate of 5% per minute, as in [24].

- *Insulin sensitivity, S.* In the case of constant insulin sensitivity, we use a value of 0.0001, as in [24].

- *Food intake parameters, σ and* ΔAUC. We obtain the physiological range of $\Delta\text{AUC} \in [0,4]$ from continuous glucose monitoring studies [17]. The derivation of σ is described in Chapter 2. The average glucose input rate is $\sigma = h_g \Delta\text{AUC}/G_0$ per minute. σ is thus estimated to range from 0 to 1/72000.

- *Glucose distribution, υ_1.* Skeletal muscle fiber diameters range between 10 and 100 microns, with variable diameters on the order of centimeters [58]. We first estimate the volume of a single skeletal muscle fiber by using a radius of 0.005 cm and an average height of 5 cm. Using the cylindrical volume, we estimate the cytosolic volume of a single

fiber to be 3.9×10^{-7} L. With a plasma volume of ~ 4 L [36] and an arbitrary skeletal muscle cell number of 2.0×10^{8},

$$v_1 = \frac{4}{(3.9 \times 10^{-7}) \cdot (2.0 \times 10^{8})} = \frac{1}{19.5} \tag{A.1}$$

describes the conversion factor of plasma glucose into a single cell.

A.1.2 Mitochondrial subsystem

- *Initial conditions.* We make the assumption that $F_2'(0) = 0$ for all variables $F_2(t)$ in subsystem (2.4). The steady-state superoxide concentration within the mitochondrial matrix has been estimated to exist in picomolar concentrations [67, 83]. We therefore use the estimated value of $R_{s0} = 10^{-5}$ μM. In [83], the initial MnSOD concentration is taken to be the steady-state value of $A_{s0} = 5$. All mitochondria are assumed to be perfectly efficient initially, implying $L_0 = 0$. We derive the initial reduced complex concentration to be $C_0 = \dfrac{v_2 N_e K_{gi} G_{i0} C_{tot}}{v_2 N_e K_{gi} G_{i0} + k_c}$. E_0 is derived to be $q_a k_{rs} R_{s0} A_{s0} / a_a$.

- *MnSOD production, a_a.* It is assumed that the maximal level of MnSOD production meets the steady-state antioxidant concentration after 8 hours. We therefore compute $a_a = \dfrac{A_{s0}}{60 \cdot 8} = 0.0104$ μM min^{-1}.

- *MnSOD signal activation, a_e.* The steady-state concentration of superoxide, R_{s0}, is assumed to maximally stimulate MnSOD production activity within 16 hours. The rate of signal activation then becomes $a_e = \dfrac{1}{60 \cdot R_{s0} \cdot 16} = 104.1667$.

- *Rate of cellular respiration, k_c.* k_c is derived from the initial equilibrium assumption: $\dfrac{v_2 N_e k_{gi} G_{i0} (C_{tot} - C_0)}{C_0} = 1200$.

- *MnSOD signal deactivation, k_e.* k_e is derived to be $a_e R_{s0}(1 - E_0)/E_0 = 7.6678 \times 10^{-4}$.

- *Superoxide dismutation, k_{rs}.* MnSOD is known to interact with superoxide at a rate ~ $\mathcal{O}(10^9)$ M^{-1} s^{-1} [34, 35, 83]. As in [35], we use $k_{rs} = 2.4 \times 10^5$ μM^{-1} min^{-1}.

- *Total electron contribution, N_e.* Each unit of glucose contributes 20 electrons to the electron transport chain. Thus, we assume $N_e = 20$ per mM [59].

- *MnSOD damage probability, q_a.* We assume 0.1% of all reactions between MnSOD and superoxide result in irreversible MnSOD damage.

- *Fractional superoxide production, q_r.* The fraction of oxidative phosphorylation in isolated mitochondria resulting in superoxide production has been found to lie between 0.001 and 0.04 [31, 49, 98]. It is estimated that *in vivo* this percentage is much smaller [32, 67]. We therefore choose $q_r = 8 \times 10^{-5}$.

- *ETC conversion factor, v_2.* It is estimated that up to 20% of skeletal muscle cell volume comprises mitochondria [58]. With a skeletal muscle cytosolic volume of 3.9×10^{-7} L and a mitochondrial population of 500, an individual mitochondrial matrix volume of 0.05 μm^3 or 5×10^{-11} L yields a total volume that is between 5 and 10% – once the volume of the intermembrane space is taken into account – of the cell volume. Using this information, v_2 is calculated to be $\frac{10^3 \cdot (3.9 \times 10^{-7})}{K \cdot (5 \times 10^{-11})} = 15600$.

- *Mitochondrial dysfunction, ξ.* Mutagenic lesions created by superoxide-mediated guanine oxidation of mtDNA can lead to alterations in the mitochondrial genome [30, 64], but an accumulation of deleterious mutations above a threshold is required before defective oxidative phosphorylation is manifest [21]. Furthermore, the fraction of genes implicated in cellular respiration is 35%, further reducing the overall effect on mitochondrial efficiency [99]. We therefore assume a low rate of appearance of mitochondrial inefficiency due to superoxide: $\xi = 8 \times 10^{-6}$.

A.2 Mitochondrial selection

- *Mitochondrial growth rates, b_0 and b_1.* We assume growth of the undamaged mitochondrial class balances its turnover. Hence $b_0 = 0.07$. Because damaged mitochondria experience a growth disadvantage, we use s to derive the growth rate for this subpopulation: $b_1 = (1-s)b_0 = 0.0644$.

- *Fractional scavenging resistance, c.* As in our sensitivity studies, we find that an excessive survival advantage, e.g., 0.4, for damaged mitochondria eliminates the effects of their growth disadvantage. At the same time, extremely small differences in scavenging susceptibility reverse the stability condition (3.6). In consideration of these effects, we choose to represent the damaged mitochondrial survival advantage by $c = 0.2$.

- *Mitochondrial turnover rates, d_0 and d_1.* Mitochondrial DNA is estimated to turnover approximately once every two weeks [30]. Thus, we set $d_0 = 0.07$. Taking into account the fractional resistance to mitophagy, we set $d_1 = (1-c)d_0 = 0.056$.

- *Mitochondrial population size, K.* Mammalian cells have, on average, between 10^3 and 10^4 copies of mtDNA, with each mitochondrion housing 2–10 copies [88]. Assuming a skeletal muscle cell copy number of 5000 with a per-mitochondrion number of 10 (as in [74]), we set $K = 500$.

- *Damage transition probability, μ.* The transition from healthy to damaged mitochondria is assumed to be small due to the slow accumulation of internal dysfunction that would lead to a fully oxidatively stressed mitochondrion. Thus, we use $\mu = 10^{-6}$.

- *Fractional growth deficit, s.* It is estimated that the growth difference between healthy and damaged is no more than 10% [60]. As such, we use $s = 0.08$.

A.3 Insulin signaling system

- *Initial conditions.* We make the assumption that $F_3'(0) = 0$ for all variables $F_3(t)$ in the simplified insulin signaling system (4.10). We assume that baseline serine phosphorylation has no inhibitory effects. This assumption is based on the idea that in the absence of insulin stimulation, IRS-1 is phosphorylated on 12 of 40 serine sites [20]. Assuming that basal insulin contributes no additional serine phosphorylation, we set $P_{s0} = 0.3$. We then derive the initial condition for tyrosine phosphorylation: $P_{y0} = \dfrac{I_{r0}(1-P_{s0})}{I_{r0}(1-P_{s0}+\delta_y/\alpha_y}$. In Sedaghat et al. [85], the fraction of GLUT4 at the cellular membrane, in the absence of insulin stimulation, is taken to be 0.04. Created from this model is an insulin-GLUT4 curve that yields a half-maximal stimulatory insulin concentration of roughly 200 pM. Under maximal insulin stimulation of 10^6 pM, GLUT4 expression at the cell surface is assumed to be 0.4. We therefore assume that the initial fraction of GLUT4 at the membrane is $U_0 = 0.04 + (0.4 - 0.04)\dfrac{I_0}{I_0 + 200}$. As recorded in [83], we set the initial concentration of hydrogen peroxide to $R_{h0} = 0.01$ μM.

- *Catalase concentration, A_h.* This value is assumed to be constant at the steady-state concentration, estimated to be roughly 3 [83].

- *Serine phosphorylation, α_s.* This parameter is derived to be $\alpha_s = \dfrac{\delta_s P_{s0}(\hat{j} + R_{h0})}{J_{\max} R_{s0}(1-P_{s0})}$.

- *Basal GLUT4 translocation, α_u.* This value, also taken from [85], is set to be $\alpha_u = 0.00696$.

- *Tyrosine phosphorylation, α_y.* The model of inuslin signaling by Sedaghat et al. models the general phosphorylation of IRS-1 [85]. As this activity results in downstream activa-

tion of elements in the insulin signaling cascade, we assume the rate of phosphorylation used corresponds to that of tyrosine activation on IRS-1. Hence, we set $\alpha_y = 4.16$.

- *Hydrogen peroxide removal,* δ_{rh}. As reported in [83], we take this value to be 3000.
- *Serine dephosphorylation,* δ_s. This value is arbitrarily set to 0.0001 to ensure the dynamics of serine phosphorylation occur on the same time scale as those of tyrosine phosphorylation.
- *GLUT4 internalization,* δ_u. From [85], we use $\delta_u = 0.167$.
- *Tyrosine dephosphorylation,* δ_y Taken from [85], $\delta_y = 0.33557$.
- *Half-maximal insulin activity,* I_h. Activity of the insulin receptor is assumed to be equivalent to the bound fraction of receptors. In [85], the percent of maximal activity of insulin receptors for a 50 pM (I_0) concentration of insulin is roughly 4%. Since we define total receptor activity to be $I_r = \dfrac{I}{I + I_h}$ in the present work, we require $0.04 = \dfrac{50}{50 + I_h}$. Thus, $I_h = 1200$.
- *PKB-mediated GLUT4 translocation,* η_p. As in [85], we use $\eta_p = 0.104375$.
- *Half-maximal JNK activation via hydrogen peroxide,* $\hat{j}$. Given experimental evidence of JNK activation and maximal effects, a half-maximal concentration of 200 μM hydrogen peroxide is assumed from [104].
- *Maximal JNK activity,* $J_{\max}$. It has been reported that millimolar concentrations of hydrogen peroxide may induce JNK activation more than five-fold. However, the actual activity level of the stress protein is unclear. In the work of Yoshizumi et al., JNK phosphorylation does not appear to saturate with 1 mM hydrogen peroxide. Given that steady-state hydrogen peroxide exists in nanomolar concentrations, it is assumed that maximal JNK activation *in vivo* saturates at an arbitrary level of 2.
- *Half-maximal PKB activity,* $\hat{p}$. As derived in Chapter 2, $\hat{p} = \delta_p / \alpha_p$. In [85], $\delta_p = 10 \ln 2$. We derive α_p from the initial steady-state assumption:

$$\alpha_p = \frac{\delta_p(\delta_u U_0 - \alpha_u(1 - U_0))}{P_{y0}[\eta_p(1 - U_0) - \delta_u U_0 + \alpha_u(1 - U_0)]} \approx 4.20321. \tag{A.2}$$

  Hence, we use $\hat{p} \approx 1.64909$.

- *Fractional hydrogen peroxide appearance, q_h.* With the hydrogen peroxide concentration at equilibrium initially, we derive q_h to be $\delta_{rh}A_hR_{h0}/\alpha_hR_{s0}K$. Note that $\alpha_h = 2k_{rs}A_{s0}$. As defined previously, the steady-state concentration of MnSOD (A_{s0}) is estimated to be about 5 μM [83] and the superoxide dismutation rate $2.4\cdot10^5$ [35]. We therefore use $q_h = 0.015$.

- *Rate of glucose uptake, $\hat{s}$.* This parameter is derived to be $(\sigma + h_g - k_gG_0)/G_0U_0$ and varies according to the value of σ.

A.4 β-cell function

- *Initial conditions.* We make the assumption that $F_4'(0) = 0$ for all variables $F_4(t)$ in the β-cell function system, comprising Equations (5.1), (5.3), and (5.4). As before, we use $G_0 = 5$, $I_0 = 50$, and $B_0 = B = 1000$. To reflect a substantial number of existing proinsulin molecules, we set $B_{uu0} = 10^6$, based on the magnitude assumed in [97]. We assume arbitrary units for B_{ux}, as there is no qualitative change in the subsystem containing the unfolded protein response when different magnitudes of the variable are considered. Hence, we arbitrarily set $B_{ux0} = 10$. We assume there is no apoptotic signal present initially, so that $Z_0 = 0$. Based on the equilibrium assumption, we derive $B_{uc0} = (\sigma_{uc} + h_{uc})/d_{uc}$ and $B_{uf0} = \dfrac{q_{uf}d_{uu}B_{uc0}B_{uu0}}{(B_{uu0}+K_{uu})k_{uf}G_0}$.

- *ER chaperone decay, d_{uc}.* This value is set to $1/120$ [97].

- *Proinsulin folding/degradation, d_{uu}.* This parameter is derived to be

$$d_{uu} = \frac{h_{uu}G_0^2(B_{uu}+K_{uu})}{(G_0^2+G_{hu}^2)(1+K_{\text{PERK}}\hat{u}_0)B_{uc}B_{uu}} \approx 4.0362,$$

where $\hat{u}_0 = \dfrac{B_{uu0}}{K_1}\left[1+\dfrac{B_{uu0}}{K_1}+\dfrac{B_{uc0}}{K_2(1+B_{uu0}/K_3)}\right]^{-1}$.

- *XBP1 mRNA decay, d_{ux}.* This value is set to $1/30$ [97].

- *Proapoptotic signal decay, d_z.* Under the assumption that proapoptotic signal decay is much faster than activation, we set $d_z = 2.0$.

- *Apoptotic effectiveness, η_z.* We assume β-cell decay is doubled when $Z = 2$, and thus set $\eta_z = 0.5$.

- *Half-maximal glucose stimulation of β-cell replication, G_{hb}.* As in [24], this value is set to the steady-state glucose concentration of 5.0.

- *β-cell replication, h_b.* This parameter is derived to be $k_b(G_0^2 + G_{hb}^2)/G_0^2 = 0.0334$.

- *Plasma insulin conversion factor, $\hat{h}_i$.* This parameter is derived to be $\hat{h}_i = \dfrac{k_i I_0}{k_{uf} B_{uf0} G_0 B_0} \approx 1.158 \times 10^{-9}$.

- *XBP1-dependent chaperone production, h_{uc}.* This value is set to $h_{uc} = 500$ [97].

- *Proinsulin production, h_{uu}.* Glucose stimulates proinsulin production in a sigmoidal manner. Maximal stimulation by glucose can lead to a 25-fold increase in proinsulin synthesis, compared to a minimally stimulated rate of 10^6 [84]. Thus, we set $h_{uu} = 25 \times 10^6$.

- *IRE1α-induced XBP1 mRNA activation, h_{ux}.* This parameter is derived to be

$$h_{ux} = \frac{d_{ux} B_{ux0}}{\hat{u}_0} \approx 6.2239.$$

- *Proapoptotic signal activation, h_z.* We assume that PERK activation above the initial steady-state level initiates a full apoptotic signal every two hours. Thus, we set $h_z = 1/120$.

- *β-cell turnover, k_b.* Adult β cells have a lifespan of about 60 days [78]. We therefore set $k_b = 1/60$.

- *Maximal PERK activity, K_{PERK}.* This value is set to 100 [97].

- *Insulin protein secretion, k_{uf}.* Maximal insulin release upon glucose stimulation occurs at a rate of roughly one granule every three seconds [15]. With each β-cell containing $\sim 10^4$ secretory granules [16], we derive a secretion rate of 0.2% min^{-1} per mM glucose. Thus, we set $k_{uf} = 0.002$.

- *Proinsulin-chaperone Michaelis-Menten constant (folding/degradation), K_{uu}.* This value is set to 10^4 [97].

- *PERK/IRE1α-proinsulin dissociation constant, K_1.* This value is set to 10^6 [97].

- *PERK/IRE1α-chaperone dissociation constant, K_2.* This value is set to 6000 [97].

- *Proinsulin-chaperone dissociation constant (chaperone sequestration), K_3.* This value is set to 2×10^5 [97].

- *Proinsulin folding fraction,* q_{uf}. We assume that 10% of all proinsulin removal results in direct degradation of proinsulin or indirect degradation via misfolded proinsulin. The remainder is assumed to be properly folded. Thus, we set $q_{uf} = 0.9$.

- *Basal chaperone production,* σ_{uc}. This value is set to 1.5 [97].

APPENDIX B

MODIFIED GILLESPIE ALGORITHM

The Gillespie algorithm, also known as the Stochastic Simulation Algorithm [37], gives a statistically exact realization of the chemical master equation, which describes the time-evolution of the probability density function of multiple states in a system. The stochastic mitochondrial selection model is a two-state system of damaged and undamaged mitochondria. To reduce the computational time used in the simulation of this system, we implement a modified version of the Gillespie algorithm, which accounts for the tendency of the system to return to 500 from 499 healthy mitochondria.

The transition matrix for this model is

$$\mathbf{A} = \begin{bmatrix} \Delta M_0 \\ \Delta M_1 \end{bmatrix} = \begin{bmatrix} \mathbf{a}_1 & \mathbf{a}_2 & \mathbf{a}_3 \end{bmatrix} = \begin{bmatrix} +1 & -1 & 0 \\ -1 & +1 & 0 \end{bmatrix}.$$

Algorithm

Step 0. Calculate the analytical expected extinction times from $M_0 = i$ mitochondria, denoted T_i. Set $\bar{\lambda} = 1/(T_K - T_{K-1})$. This is the average time it takes for one undamaged mitochondrion to be lost from an entirely healthy population.

Step 1. Initialize the system: $j = 0,\ t_0 = 0,\ M_0^0 = K,\ M_1^0 = 0$.

Step 2. Calculate the transition probability rates $v_i,\ i = 1,2,3$, where

$$\begin{aligned} v_1 &= d_0 M_0 \frac{\mu b_0 M_0 + b_1 M_1}{b_0 M_0 + b_1 M_1} \\ v_2 &= d_1 M_1 \frac{(1-\mu) b_0 M_0}{b_0 M_0 + b_1 M_1} \\ v_3 &= \frac{d_0 M_0 (1-\mu) b_0 M_0 + d_1 M_1 (\mu b_0 M_0 + b_1 M_1)}{b_0 M_0 + b_1 M_1}, \end{aligned}$$

and set $v_0 = \sum_{n=1}^{3} v_n$.

Step 3. Choose τ from an exponential distribution with rate $\lambda = v_0$, and u from a discrete uniform distribution with $n = 3$. τ determines the time at which the next event occurs, and u determines the event $\mathbf{a}_u$ to occur.

Step 4. Update t: $t_{j+1} = t_j + \tau$. Update M_0 and M_1:

$$\begin{bmatrix} M_0^{j+1} \\ M_1^{j+1} \end{bmatrix} = \begin{bmatrix} M_0^{j} \\ M_1^{j} \end{bmatrix} + \mathbf{a}_u$$

(a) If $M_0^{j+1} \neq 500$, update $j = j + 1$.

(b) If $M_0^{j+1} = 500$, choose $\bar{\tau} \sim \exp(\bar{\lambda})$. Reset $M_0^{j+1} = 499$, $M_1^{j+1} = 1$, and $t_{j+1} = t_{j+1} + \bar{\tau}$. Update $j = j + 1$.

Return to Step 1.

APPENDIX C

SOLUTION TO THE MODIFIED GAMBLER'S RUIN PROBLEM

We derive the solution to the modified Gambler's Ruin problem formulated in Chapter 3. The transition matrix

$$\begin{bmatrix}\Delta M_0\\ \Delta M_1\end{bmatrix} = \begin{bmatrix}\mathbf{a}_1 & \mathbf{a}_2 & \mathbf{a}_3\end{bmatrix} = \begin{bmatrix}+1 & -1 & 0\\ -1 & +1 & 0\end{bmatrix}$$

describes the three possible outcomes of an event in the stochastic model. Let $p_i = \Pr(\mathbf{a}_1|M_0 = i)$ and $q_i = \Pr(\mathbf{a}_2|M_0 = i)$. Then $1 - p_i - q_i = \Pr(\mathbf{a}_3|M_0 = i)$. Let b_i and d_i be the birth and death rates of mitochondrial subpopulation i, $i = 0,1$. Let μ be the probability that an undamaged mitochondrion transitions to a damaged one. $M_0 + M_1 = K$ implies that $M_1 = K - M_0$. Then

$$p_i = \underbrace{\frac{d_1(K-i)}{d_0 i + d_1(K-i)}}_{\text{death from } \mathscr{C}_1} \cdot \underbrace{\frac{(1-\mu)b_0 i}{b_0 i + b_1(K-i)}}_{\text{birth to } \mathscr{C}_0} \qquad \text{and}$$

$$q_i = \underbrace{\frac{d_0 i}{d_0 i + d_1(K-i)}}_{\text{death from } \mathscr{C}_0} \cdot \underbrace{\frac{\mu b_0 i + b_1(K-i)}{b_0 i + b_1(K-i)}}_{\text{transition/birth to } \mathscr{C}_1}, \qquad \text{so that}$$

$$1 - p_i - q_i = \underbrace{\frac{d_1(K-i)}{d_0 i + d_1(K-i)}}_{\text{death from } \mathscr{C}_1} \cdot \underbrace{\frac{\mu b_0 i + b_1(K-i)}{b_0 i + b_1(K-i)}}_{\text{transition/birth to } \mathscr{C}_1} + \underbrace{\frac{d_0 i}{d_0 i + d_1(K-i)}}_{\text{death from } \mathscr{C}_0} \cdot \underbrace{\frac{(1-\mu)b_0 i}{b_0 i + b_1(K-i)}}_{\text{birth to } \mathscr{C}_0}.$$

Let W_i be the probability that M_0 will equal K before it reaches zero, having begun with $M_0 = i$. In general,

$$W_i = p_i W_{i+1} + q_i W_{i-1},$$

and $W_K = \mu W_{K-1}$. Now, let L_i be the probability that $M_0 = 0$ will occur before $M_0 = K$ from i mitochondria. Then

$$(1 - L_i) = p_i(1 - L_{i+1}) + q_i(1 - Li - 1)$$

$$\Rightarrow \quad L_i = (1 - p_i - q_i) + p_i L_{i+1} + q_i L_{i-1}.$$

Let T_i be the expected time until $M_0 = 0$ from $M_0 = i$, and let E_i be the average duration of time between events. Then

$$\begin{aligned} & T_i = (1-p_i-q_i)(T_i+E_i) + p_i(T_{i+1}+E_i) + q_i(T_{i-1}+E_i) \\ \Rightarrow \quad & q_i T_{i-1} - (p_i+q_i)T_i + p_i T_{i+1} = -E_i, \end{aligned}$$

with boundary condition $T_0 = 0$. Let $\Delta_i = T_{i+1} - T_i$. Then

$$\begin{aligned} & p_i(T_{i+1}-T_i) - q_i(T_i - T_{i-1}) = -E_i \\ \Leftrightarrow \quad & p_i\Delta_i - q_i\Delta_{i-1} = -E_i \\ \Leftrightarrow \quad & \Delta_{i-1} = \frac{E_i}{q_i} + \frac{p_i}{q_i}\Delta_i, \end{aligned}$$

and letting $\rho_i = \dfrac{p_i}{q_i}$ and $\eta_i = \dfrac{E_i}{q_i}$ gives $\Delta_{i-1} = \rho_i\Delta_i + \eta_i$. We proceed by solving this equation recursively. With $\Delta K = 0$,

$$\begin{aligned} & \Delta_{K-1} = \eta_K + \rho_K\Delta_K \\ & \Delta_{K-2} = \eta_{K-1} + \rho_{K-1}\eta_K \\ & \Delta_{K-3} = \eta_{K-2} + \rho_{K-2}\rho_{K-1}\eta_K + \rho_{K-2}\eta_{K-1} \\ & \qquad \vdots \\ \Rightarrow \quad & \Delta_{K-i} = \eta_{K-i+1} + \sum_{m=0}^{i-2}\left[\eta_{K-m}\prod_{n=m+1}^{i-1}\rho_{K-n}\right] \\ \Leftrightarrow \quad & \Delta_i = \eta_{i+1} + \sum_{m=0}^{K-i-2}\left[\eta_{K-m}\prod_{n=m+1}^{K-i-1}\rho_{K-n}\right]. \end{aligned}$$

It follows that

$$T_{i+1} = T_i + \eta_{i+1} + \sum_{m=0}^{K-i-2}\prod_{n=m+1}^{K-i-1}\eta_{K-m}\rho_{K-n},$$

subject to $T_K = \eta_K + T_{K-1}$ and $T_0 = 0$. Further,

$$\begin{aligned} T_1 &= T_0 + \eta_1 + \sum_{m=0}^{K-2}\prod_{n=m+1}^{K-1}\eta_{K-m}\rho_{K-n} \\ T_2 &= T_1 + \eta_2 + \sum_{m=0}^{K-3}\prod_{n=m+1}^{K-2}\eta_{K-m}\rho_{K-n} \\ &= T_0 + \left[\eta_1 + \sum_{m=0}^{K-2}\prod_{n=m+1}^{K-1}\eta_{K-m}\rho_{K-n}\right] + \left[\eta_2 + \sum_{m=0}^{K-3}\prod_{n=m+1}^{K-2}\eta_{K-m}\rho_{K-n}\right] \\ &\vdots \\ \Rightarrow & \begin{cases} T_i = T_0 + \displaystyle\sum_{j=0}^{i-1}\left[\eta_{j+1} + \sum_{m=0}^{K-j-2}\prod_{n=m+1}^{K-j-1}\eta_{K-m}\rho_{K-n}\right], & i = 1,\ldots,K-1, \\ T_K = \eta_K + T_{K-1}. \end{cases} \end{aligned}$$

REFERENCES

[1] M. A. ABDUL-GHANI AND R. A. DEFRONZO, *Pathogenesis of insulin resistance in skeletal muscle*, J. Biomed. Biotechnol., 2010 (2010), pp. 1–19.

[2] V. AGUIRRE, T. UCHIDA, L. YENUSH, R. DAVIS, AND M. F. WHITE, *The c-Jun N-terminal kinase promotes insulin resistance during association with insulin receptor substrate-1 and phosphorylation of Ser*^{307}, J. Biol. Chem., 275 (2000), pp. 9047–9054.

[3] AMERICAN DIABETES ASSOCIATION, *Diagnosis and classification of diabetes mellitus*, Diabetes Care, 33 (2010), pp. S62–S69.

[4] B. N. AMES, M. K. SHIGENAGA, AND T. M. HAGEN, *Mitochondrial decay in aging*, Biochim. Biophys. Acta, 1271 (1995), pp. 165–170.

[5] T. ANELLI AND R. SITIA, *Protein quality control in the early secretory pathway*, EMBO J., 27 (2008), pp. 315–327.

[6] A. D. ATTIE AND P. E. SCHERER, *Adipocyte metabolism and obesity*, J. Lipid Res., 50 (2009), pp. S395–S399.

[7] S. H. BACK AND R. J. KAUFMAN, *Endoplasmic reticulum stress and type 2 diabetes*, Ann. Rev. Biochem., 81 (2012), pp. 16.1–16.27.

[8] N. BASHAN, J. KOVSAN, I. KACHKO, H. OVADIA, AND A. RUDICH, *Positive and negative regulation of insulin signaling by reactive oxygen and nitrogen species*, Physiol. Rev., 89 (2009), pp. 27–71.

[9] K. BECKMAN AND B. N. AMES, *Endogenous oxidative damage of mtDNA*, Mutat. Res., 424 (1999), pp. 51–58.

[10] A. BERDICHEVSKY, L. GUARENTE, AND A. BOSE, *Acute oxidative stress can reverse insulin resistance by inactivation of cytoplasmic JNK*, J. Biol. Chem., 285 (2010), pp. 21581–21589.

[11] R. BERGMAN, Y. Z. IDER, C. R. BOWDEN, AND C. COBELLI, *Quantitative estimation of insulin sensitivity*, Am. J. Physiol., 236 (1979), pp. E667–E677.

[12] R. N. BERGMAN, *Minimal model: Perspective from 2005*, Horm. Res., 64 (2005), pp. 8–15.

[13] C. BONNARD, A. DURAND, S. PEYROL, E. CHANSEAUME, M. CHAUVIN, B. MORIO, H. VIDAL, AND J. RIEUSSET, *Mitochondrial dysfunction results from oxidative stress in the skeletal muscle of diet-induced insulin-resistant mice*, J. Clin. Invest., 118 (2008), pp. 789–800.

[14] M. D. BRAND, *Uncoupling to survive? The role of mitochondrial inefficiency in ageing*, Exp. Gerontol., 35 (2000), pp. 811–820.

[15] T. K. BRATANOVA-TOCHKOVA, H. CHENG, S. DANIEL, S. GUNAWARDANA, Y. LIU, J. MULVANEY-MUSA, T. SCHERMERHORN, S. G. STRAUB, H. YAJIMA, AND G. W. G. SHARP, *Triggering and augmentation mechanisms, granule pools, and biphasic insulin secretion*, Diabetes, 51 (2002), pp. S83–S90.

[16] Y. BRUNNER, Y. COUTÉ, M. IEZZI, M. FOTI, M. FUKUDA, D. F. HOCHSTRASSER, C. B. WOLLHEIM, AND J. SANCHEZ, *Proteomics analysis of insulin secretory granules*, Molec. Cell. Proteomics, 6 (2007), pp. 1007–1017.

[17] A. E. BRYNES, J. ADAMSON, A. DORNHORST, AND G. S. FROST, *The beneficial effect of a diet with low glycaemic index on 24h glucose profiles in healthy young people as assessed by continuous glucose monitoring*, Brit. J. Nutr., 93 (2005), pp. 179–182.

[18] A. E. BUTLER, J. JANSON, S. BONNER-WEIR, R. RITZEL, R. A. RIZZA, AND P. C. BUTLER, *β-cell deficit and increased β-cell apoptosis in humans with type 2 diabetes*, Diabetes, 52 (2003), pp. 102–110.

[19] CENTERS FOR DISEASE CONTROL AND PREVENTION, *National diabetes fact sheet: national estimates and general information on diabetes and prediabetes in the United States, 2011*, U.S. Department of Health and Human Services, Centers for Disease Control and Prevention, 2011.

[20] B. CHEATHAM AND C. R. KAHN, *Insulin action and the insulin signaling network*, Endocr. Rev., 16 (1995), pp. 117–142.

[21] H. CHEN, M. VERMULST, Y. E. WANG, A. CHOMYN, T. A. PROLLA, J. M. MCCAFFERY, AND D. C. CHAN, *Mitochondrial fusion is required for mtDNA stability in skeletal muscle and tolerance of mtDNA mutations*, Cell, 141 (2010), pp. 280–289.

[22] A. CLARK, L. C. JONES, E. DE KONING, B. C. HANSEN, AND D. R. MATTHEWS, *Decreased insulin secretion in type 2 diabetes: a problem of cellular mass or function?*, Diabetes, 50 (2001), pp. S169–S171.

[23] C. DALLA MAN, R. A. RIZZA, AND C. COBELLI, *Meal simulation model of the glucose-insulin system*, IEEE Trans. Biomed. Eng., 54 (2007), pp. 1740–1749.

[24] A. DE GAETANO, T. HARDY, B. BECK, E. ABU-RADDAD, P. PALUMBO, J. BUE-VALLESKEY, AND N. PØRKSEN, *Mathematical models of diabetes progression*, Am. J. Physiol. Endocrinol. Metab., 295 (2008), pp. E1462–E1479.

[25] R. A. DEFRONZO, *Pathogenesis of type 2 diabetes mellitus*, Med. Clin. N. Am., 88 (2004), pp. 787–835.

[26] S. DEL PRATO, W. J. WISHNER, J. GROMADA, AND B. SCHLUCHTER, *β-Cell mass plasticity in type 2 diabetes*, Diab. Obes. Metab., 6 (2004), pp. 319–331.

[27] S. A. DETMER AND D. C. CHAN, *Functions and dysfunctions of mitochondrial dynamics*, Nat. Rev. Mol. Cell Biol., 8 (2007), pp. 870–879.

[28] M. Y. DONATH AND S. E. SHOELSON, *Type 2 diabetes as an inflammatory disease*, Nat. Rev. Immunol., 11 (2011), pp. 98–107.

[29] W. DRÖGE, *Free radicals in the physiological control of cell function*, Physiol. Rev., 82 (2002), pp. 47–95.

[30] N. M. DRUZHYNA, G. L. WILSON, AND S. P. LEDOUX, *Plant Mitochondria*, Springer Science + Business Media, 2011, ch. Human mitochondrial mutations and repair.

[31] J. L. EVANS, I. D. GOLDFINE, B. A. MADDUX, AND G. M. GRODSKY, *Oxidative stress and stress-activated signaling pathways: a unifying hypothesis of type 2 diabetes*, Endocr. Rev., 23 (2002), pp. 599–622.

[32] T. FINKEL, *Signal transduction by reactive oxygen species*, J. Cell Biol., 194 (2011), pp. 7–15.

[33] S. G. FONSECA, J. GROMADA, AND F. URANO, *Endoplasmic reticulum stress and pancreatic β-cell death*, Trends Endocrin. Met., 22 (2011), pp. 266–274.

[34] I. FRIDOVICH, *Superoxide dismutases*, Annu. Rev. Biochem., 44 (1975), pp. 147–159.

[35] ——, *Superoxide radical and superoxide dismutases*, Annu. Rev. Biochem., 64 (1995), pp. 97–112.

[36] W. F. GANONG, *Review of medical physiology*, Appleton & Lange, fourteenth ed., 1989.

[37] D. T. GILLESPIE, *Exact stochastic simulation of coupled chemical reactions*, J. Phys. Chem., 81 (1977), pp. 2340–2361.

[38] M. A. GUNEY AND M. GANNON, *Pancreas cell fate*, Birth Defects Res., Part C, 87 (2009), pp. 232–248.

[39] D. HANAHAN, H. O. MCDEVITT, AND G. F. CAHILL, JR., eds., *Perspectives on the molecular biology and immunology of the pancreatic β cell*, Cold Spring Harbor Laboratory, 1989.

[40] S. C. HANLEY, E. AUSTIN, B. AUSSOULINE-THOMAS, J. KAPELUTO, J. BLAICHMAN, M. MOOSAVI, M. PETROPAVLOVSKAIA, AND L. ROSENBERG, *β-cell mass dynamics and islet plasticity in human type 2 diabetes*, Endocrinology, 151 (2010), pp. 1462–1472.

[41] C. HETZ, *The unfolded protein response: controlling cell fate decisions under ER stress and beyond*, Nat. Rev. Mol. Cell Biol., 36 (2012), pp. 329–337.

[42] K. HIRATANI, T. HARUTA, A. TANI, J. KAWAHARA, I. USIO, AND M. KOBAYASHI, *Roles of mTOR and JNK in serine phosphorylation, translocation, and degradation of IRS-1*, Biochem. Biophys. Res. Commun., 335 (2005), pp. 836–842.

[43] K. L. HOEHN, A. B. SALMON, C. HOHNEN-BEHRENS, N. TURNER, A. J. HOY, G. J. MAGHZAL, R. STOCKER, H. VAN REMMEN, E. W. KRAEGEN, G. J. COONEY, A. R. RICHARDSON, AND D. E. JAMES, *Insulin resistance is a cellular antioxidant defense mechanism*, Proc. Natl. Acad. Sci., 106 (2009), pp. 17787–17792.

[44] A. K. HOLLEY, V. BAKTHAVATCHALU, J. M. VELEZ-ROMAN, AND D. K. ST. CLAIR, *Manganese superoxide dismutase: guardian of the powerhouse*, Int. J. Mol. Sci., 12 (2011), pp. 7114–7162.

[45] G. S. HOTAMISLIGIL AND E. ERBAY, *Nutrient sensing and inflammation in metabolic diseases*, Nat. Rev. Immunol., 8 (2008), pp. 923–934.

[46] S. JITRAPAKDEE, A. WUTTHISATHAPORNCHAI, J. C. WALLACE, AND M. J. MACDONALD, *Regulation of insulin secretion: role of mitochondrial signalling*, Diabetologia, 53 (2010), pp. 1019–1032.

[47] T. KADOWAKI, *Insights into insulin resistance and type 2 diabetes from knockout mouse models*, J. Clin. Invest., 106 (2000), pp. 459–465.

[48] C. R. KAHN, G. L. KING, A. C. MOSES, G. C. WEIR, A. M. JACOBSON, AND R. J. SMITH, eds., *Joslin's diabetes mellitus*, Lippincott Williams & Wilkins, fourteenth ed., 2005.

[49] J. KIM, Y. WEI, AND J. R. SOWERS, *Role of mitochondrial dysfunction in insulin resistance*, Circ. Res., 102 (2008), pp. 401–414.

[50] A. KOWALD AND T. B. L. KIRKWOOD, *A network theory of ageing: the interactions of defective mitochondria, aberrant proteins, free radicals and scavengers in the ageing process*, Mutat. Res., 316 (1996), pp. 209–236.

[51] ——, *Accumulation of defective mitochondria through delayed degradation of damaged organelles and its possible role in the ageing of post-mitotic and dividing cells*, J. Theor. Biol., 202 (2000), pp. 145–160.

[52] A. J. KOWALTOWSKI AND A. E. VERCESI, *Mitochondrial damage induced by conditions of oxidative stress*, Free Radic. Biol. Med., 26 (1999), pp. 463–471.

[53] J. L. LEAHY, *Pathogenesis of type 2 diabetes mellitus*, Arch. Med. Res., 36 (2005), pp. 197–209.

[54] A. LEE, K. HEIDTMAN, G. S. HOTAMISLIGIL, AND L. H. GLIMCHER, *Dual and opposing roles of the unfolded protein response regulated by IRE1α and XBP1 in proinsulin processing and insulin secretion*, Proc. Natl. Acad. Sci., 108 (2011), pp. 8885–8890.

[55] Y. H. LEE AND M. F. WHITE, *Insulin receptor substrate proteins and diabetes*, Arch. Pharm. Res., 27 (2004), pp. 361–370.

[56] G. LEIBOWITZ, E. BACHAR, M. SHAKED, A. SINAI, M. KETZINEL-GILAD, E. CERASI, AND N. KAISER, *Glucose regulation of β-cell stress in type 2 diabetes*, Diab. Obes. Metab., 12 (2010), pp. 66–75.

[57] D. LEROITH, S. I. TAYLOR, AND J. M. OLEFSKY, eds., *Diabetes mellitus: A fundamental and clinical text*, Lippincott Williams & Wilkins, third ed., 2004.

[58] R. L. LIEBER, *Skeletal muscle structure, function, and plasticity: the physiological basis of rehabilitation*, Lippincott Williams & Wilkins, third ed., 2010.

[59] H. LODISH, A. BERK, P. MATSUDAIRA, C. A. KAISER, M. KRIEGER, M. P. SCOTT, S. L. ZIPURSKY, AND J. DARNELL, *Molecular Cell Biology*, W.H. Freeman and Company, 2004.

[60] L. LOEWE, *Quantifying the genomic decay paradox due to Muller's ratchet in human mitochondrial DNA*, Genet. Res., Camb., 87 (2006), pp. 133–159.

[61] C. N. LUMENG, J. B. DELPROPOSTO, D. J. WESTCOTT, AND A. R. SALTIEL, *Phenotypic switching of adipose tissue macrophages with obesity is generated by spatiotemporal differences in macrophage subtypes*, Diabetes, 57 (2008), pp. 3239–3246.

[62] P. MÄÄTTÄNEN, K. GEHRING, J. J. M. BERGERON, AND D. Y. THOMAS, *Protein quality control in the ER: the recognition of misfolded proteins*, Semin. Cell Dev. Biol., 21 (2010), pp. 500–511.

[63] P. MARCHETTI, F. DOTTA, D. LAURO, AND F. PURELLO, *An overview of pancreatic beta-cell defects in human type 2 diabetes: implications for treatment*, Regul. Peptides, 146 (2006), pp. 4–11.

[64] S. MARCHI, C. GIORGI, J. M. SUSKI, C. AGNOLETTO, A. BONONI, M. BONORA, E. DE MARCHI, S. MISSIROLI, S. PATERGNANI, F. POLETTI, A. RIMESSI, J. DUSZYNSKI, M. R. WIECKOWSKI, AND P. PINTON, *Mitochondria-Ros crosstalk in the control of cell death and aging*, J. Sig. Transduc., 2012 (2012), pp. 1–17.

[65] L. MIAO AND D. K. S. CLAIR, *Regulation of superoxide dismutase genes: implications in disease*, Free Radic. Biol. Med., 47 (2009), pp. 344–356.

[66] D. M. MUOIO AND C. B. NEWGARD, *Molecular and metabolic mechanisms of insulin resistance and β-cell failure in type 2 diabetes*, Nat. Rev. Mol. Cell Biol., 9 (2008), pp. 193–205.

[67] M. P. MURPHY, *How mitochondria produce reactive oxygen species*, Biochem. J., 417 (2009), pp. 1–13.

[68] L. C. MURTAUGH, *Pancreas and beta-cell development: from the actual to the possible*, Development, 134 (2007), pp. 427–438.

[69] C. J. NOLAN, P. DAMM, AND M. PRENTKI, *Type 2 diabetes across generations: from pathophysiology to prevention and management*, Lancet, 378 (2011), pp. 169–181.

[70] C. J. NOLAN AND M. PRENTKI, *The islet β-cell: fuel responsive and vulnerable*, Trends Endocrin. Met., 19 (2008), pp. 285–291.

[71] E. NYMAN, C. BRÄNNMARK, R. PALMÉR, J. BRUGÅRD, F. H. NYSTRÖM, P. STRÅLFORS, AND G. CEDERSUND, *A hierarchical whole-body modeling approach elucidates the link between* in vitro *insulin signaling and* in vivo *glucose homeostasis*, J. Biol. Chem., 286 (2011), pp. 26028–26041.

[72] M. PAL, *Recent advances in glucokinase activators for the treatment of type 2 diabetes*, Drug Discov. Today, 14 (2009), pp. 784–792.

[73] G. PANI, O. R. KOCH, AND T. GALEOTTI, *The p53-p66shc-Manganese superoxide dismutase (MnSOD) network: A mitochondrial intrigue to generate reactive oxygen species*, Int. J. Biochem. Cell Biol., 41 (2009), pp. 1002–1005.

[74] S. K. POOVATHINGAL, J. GRUBER, B. HALLIWELL, AND R. GUNAWAN, *Stochastic drift in mitochondrial DNA point mutations: a novel perspective* ex silico, PLoS Comp. Bio., 5 (2009), p. e10000572.

[75] S. P. PORTERFIELD, *Endocrine Physiology*, Mosby, Inc., second ed., 2001.

[76] G. PRATVIEL AND B. MEUNIER, *Guanine oxidation: one- and two-electron reactions*, Chem. Eur. J., 12 (2006), pp. 6018–6030.

[77] J. RAHIER, Y. GUIOT, R. M. GOEBBELS, C. SEMPOUX, AND J. C. HENQUIN, *Pancreatic β-cell mass in European subjects with type 2 diabetes*, Diab. Obes. Metab., 10 (2008), pp. 32–42.

[78] C. J. RHODES, *Type 2 diabetes—a matter of β-cell life and death?*, Science, 307 (2005), pp. 380–384.

[79] D. RON AND P. WALTER, *Signal integration in the endoplasmic reticulum unfolded protein response*, Nat. Rev. Mol. Cell Biol., 8 (2007), pp. 519–529.

[80] H. RUAN AND H. F. LODISH, *Insulin resistance in adipose tissue: direct and indirect effects of tumor necrosis factor-α*, Cytokine Growth F. R., 14 (2003), pp. 447–455.

[81] M. M. SACHDEVA AND D. A. STOFFERS, *Meeting the demand for insulin: molecular mechanisms of adaptive postnatal β-cell mass expansion*, Mol. Endocrinol., 23 (2009), pp. 747–758.

[82] V. T. SAMUEL AND G. I. SHULMAN, *Mechanisms for insulin resistance: common threads and missing links*, Cell, 148 (2012), pp. 852–871.

[83] J. G. SCANDALIOS, *Oxidative stress and the molecular biology of antioxidant defenses*, Cold Spring Harbor Laboratory, 1997.

[84] F. C. SCHUIT, P. A. IN'T VELD, AND D. G. PIPELEERS, *Glucose stimulates proinsulin biosynthesis by a dose-dependent recruitment of pancreatic beta cells*, Proc. Natl. Acad. Sci, 85 (1988), pp. 3865–3869.

[85] A. R. SEDAGHAT, A. SHERMAN, AND M. J. QUON, *A mathematical model of metabolic insulin signaling pathways*, Am. J. Physiol. Endocrinol. Metab., 283 (2002), pp. E1084–E1101.

[86] S. SEINO AND G. I. BELL, eds., *Pancreatic beta cell in health and disease*, Springer, 2008.

[87] G. SESTI, *Pathophysiology of insulin resistance*, Best Pract. Res. Clin. Endocrinol. Metab., 20 (2006), pp. 665–679.

[88] J. A. M. SMEITINK, R. C. A. SENGERS, AND J. M. F. TRIJBELS, eds., *Oxidative phosphorylation in health and disease*, Landes Bioscience/Eureka.com; Kluwer Academic/Plenum Publishers, 2004.

[89] J. D. SMITH, A. BOREL, J. NAZARE, S. M. HAFFNER, B. BALKAU, R. ROSS, C. MASSIEN, N. ALMÉRAS, AND J. DESPRÉS, *Visceral adipose tissue indicates the severity of cardiometabolic risk in patients with and without type 2 diabetes: results from the INSPIRE ME IAA study*, J. Clin. Endocrinol. Metab., 97 (2012), pp. 1517–1525.

[90] A. G. TABÁK, M. JOKELA, T. N. AKBARALY, E. J. BRUNNER, M. KIVIMÄKI, AND D. R. WITTE, *Trajectories of glycaemia, insulin sensitivity, and insulin secretion before diagnosis of type 2 diabetes: an analysis from the Whitehall II study*, Lancet, 373 (2009), pp. 2215–2221.

[91] C. M. TANIGUCHI, B. MANUELLI, AND C. R. KAHN, *Critical nodes in signalling pathways: insights into insulin action*, Nat. Rev. Mol. Cell Biol., 7 (2006), pp. 85–96.

[92] R. W. TAYLOR AND D. M. TURNBULL, *Mitochondrial DNA mutations in human disease*, Nat. Rev. Genet., 6 (2005), pp. 389–402.

[93] A. TERMAN AND U. T. BRUNK, *Myocyte aging and mitochondrial turnover*, Exp. Gerontol., 39 (2004), pp. 701–705.

[94] T. TIGANIS, *Reactive oxygen species and insulin resistance: the good, the bad and the ugly*, Trends Pharmacol. Sci., 32 (2011), pp. 82–89.

[95] T. A. TIRONE AND F. C. BRUNICARDI, *Overview of glucose regulation*, World J. Surg., 25 (2001), pp. 461–467.

[96] B. TOPP, K. PROMISLOW, G. DEVRIES, R. M. MIURA, AND D. T. FINEGOOD, *A model of β-cell mass, insulin, and glucose kinetics: pathways to diabetes*, J. Theor. Biol., 206 (2000), pp. 605–619.

[97] A. TRUSINA, F. R. PAPA, AND C. TANG, *Rationalizing translation attenuation in the network architecture of the unfolded protein response*, Proc. Natl. Acad. Sci., 105 (2008), pp. 20280–20285.

[98] M. VALKO, D. LEIBFRITZ, J. MONCOL, M. T. D. CRONIN, M. MAZUR, AND J. TELSER, *Free radicals and antioxidants in normal physiological functions and human disease*, Int. J. Biochem. Cell. Biol., 39 (2007), pp. 44–84.

[99] D. C. WALLACE, *A mitochondrial paradigm of metabolic degenerative diseases, aging, and cancer: a dawn for evolutionary medicine*, Annu. Rev. Genet., 39 (2005), pp. 359–407.

[100] G. C. WEIR AND S. BONNER-WEIR, *Five stages of evolving β-cell dysfunction during progression to diabetes*, Diabetes, 53 (2004), pp. S16–S21.

[101] G. WILCOX, *Insulin and insulin resistance*, Clin. Biochem. Rev., 26 (2005), pp. 19–39.

[102] D. A. WINER, S. WINER, L. SHEN, P. P. WADIA, J. YANTHA, G. PALTSER, H. TSUI, P. WU, M. G. DAVIDSON, M. N. ALONSO, H. X. LEONG, A. GLASSFORD, M. CAIMOL, J. A. KENKEL, T. F. TEDDER, T. MCLAUGHLIN, D. B. MIKLOS, H. DOSCH, AND E. G. ENGELMAN, *B cells promote insulin resistance through modulation of T cells and production of pathogenic IgG antibodies*, Nat. Med., 17 (2011), pp. 610–617.

[103] C. YIN LIU AND R. J. KAUFMAN, *The unfolded protein response*, J. Cell Sci., 116 (2003), pp. 1861–1862.

[104] M. YOSHIZUMI, J. ABE, J. HAENDELER, Q. HUANG, AND B. C. BERK, *Src and Cas mediate JNK activation but not ERK1/2 and p38 kinases by reactive oxygen species*, J. Biol. Chem., 275 (2000), pp. 11706–11712.

[105] R. ZECHNER, R. ZIMMERMANN, T. O. EICHMANN, S. D. KOHLWEIN, G. HAEMMERLE, A. LASS, AND F. MADEO, *Fat signals – lipases and lipolysis in lipid metabolism and signaling*, Cell Metab., 15 (2012), pp. 279–291.

[106] K. ZIERLER, *Whole body glucose metabolism*, Am. J. Phys. Endocrinol. Metab., 276 (1999), pp. E409–E426.

[107] M. ZORATTI AND I. SZABÓ, *The mitochondrial permeability transition*, Biochim. Biophys. Acta, 1241 (1995), pp. 139–176.